FACULDADE DE ENGENHARIA DA UNIVERSIDADE DO PORTO

# Machinability studies of conventional and additively manufactured 316L stainless steel

**Ana Chantal Leites Amaral**

INTEGRATED MASTERS IN MECHANICAL ENGINEERING FACULTY OF ENGINEERING OF THE UNIVERSITY OF PORTO

Master's Dissertation

Supervisor: Prof. Dr. Abílio Manuel Pinho de Jesus

Co-supervisor: Eng. Tiago Emanuel Fraga da Silva

Co-supervisor: Prof. Manuel Fernando Gonçalves Vieira

July 24, 2019

# Machinability studies of conventional and additively manufactured 316L stainless steel

**Ana Chantal Leites Amaral**

Master's Dissertation

July 24, 2019

# Resumo

O fabrico aditivo metálico é um método emergente para o fabrico de componentes metálicos com formas complexas e um elevado grau de personalização. No entanto, um dos principais desafios deste método de fabrico é a qualidade superficial resultante, o que leva à necessidade de operações de pós-processamento. A presente dissertação consiste no estudo da maquinabilidade do aço inoxidável 316L produzido por *selective laser melting* (SLM).

Numa primeira fase deste estudo procedeu-se à caracterização do material, no estado *as-built*, em termos de microestrutura, rugosidade superficial e propriedades mecânicas. Seguindo-se a realização de um total de 144 operações de torneamento longitudinal, a seco, com diferentes parâmetros de corte e ferramentas, com o intuito de estudar a diferença entre o material convencional e o de fabrico aditico, em termos das forças de corte, potências, pressões específicas de corte, formas das aparas geradas e rugosidades superficiais. Além disso, realizou-se uma simulação numérica 2D para complementar os estudos de maquinabilidade sob condições de corte ortogonais, tendo em vista o planeamento futuro de ensaios de corte ortogonal.

Os ensaios de torneamento permitiram verificar que o material de fabrico aditivo tem um comportamento semelhante ao convencional, em termos das forças de corte e formas das aparas geradas, sendo que a maior diferença encontrada entre resultados destes ensaios advém da utilização de ferramentas de corte distintas e não dos materiais. No que diz repeito à qualidade superficial, o material de fabrico aditivo apresentou globalmente uma menor rugosidade superficial quando comparado ao material convencional, demonstrando uma melhoria significativa, quando comparado ao estado *as-built*, com um decréscimo de rugosidade média superficial de 11.06$\mu$m para 0.38$\mu$m, depois da operação de acabamento. As simulações numéricas de corte ortogonal revelaram forças de corte inferiores para o material convencional quando comparado ao de fabrico aditivo, que por sua vez está relacionado com a lei constitutiva utilizada para caracterizar o material de fabrico aditivo.

# Abstract

Metal additive manufacturing is a novel method for fabricating metallic components with intricate shapes at a high degree of customization. However, the resulting surface quality is one of the main challenges of this method, hence the necessity for post-processing operations. This dissertation presents a machinability study of stainless steel 316L fabricated by selective laser melting (SLM).

This study initiates with the SLM 316L material characterization, in the as-built state, in terms of microstructure, surface roughness and mechanical properties. Then a total of 144 instrumented dry turning experiments with different cutting conditions and tools were performed, to infer on the differences between the conventional and SLM 316L in terms of cutting forces, cutting power, specific cutting pressure, chip formation and surface roughness. In addition, 2D metal cutting simulations were conducted for further machinability studies under orthogonal cutting conditions.

This study demonstrates that turning wrought or SLM 316L is similar in what concerns cutting forces and chip formation, the major differences found in these outputs were not among materials, but rather between cutting tools tested. Concerning surface quality, the selective laser melted 316L presented an overall lower average roughness in comparison to the wrought material and demonstrated a significant improvement from the as-built state; the average surface roughness was decreased from 11.06$\mu$m to 0.38$\mu$m after fine-finishing. Despite requiring further experimental validation of the considered strain-rate influence on the identified quasi-static flow stress of the SLM 316L, the numerical simulations of orthogonal cutting revealed lower cutting forces for the wrought 316L.

# Acknowledgements

The completion of this dissertation would not have been possible without the input and assistance of many individuals, however, there are some people that I want to thank in particular.

Foremost, I would like to thank Prof. Abílio Jesus for the opportunity to develop the current thesis, for his wise inputs, guidance, patience and for his help in overcoming the difficulties that arose throughout the project.

I also thank Tiago Silva for his permanent availability and constant willingness to help. For giving me the freedom to make my own decisions, but at the same time steering me in the right direction.

Additionally, I thank Domingos Carvalho, responsible for the mechanical workshops at FEUP, for his availability and assistance throughout the project.

I extend my appreciation to INEGI for all the work conditions and technical support. A special thank to Armanda Marques, responsible for the metallurgical laboratory, for her enthusiasm and relentless efforts in the material characterization stage.

I would also like to acknowledge CETRIB, in particular Prof. Carlos Fernandes for his help and expertise in the material analysis stage. Eng. Miguel Figueiredo and Rui Silva, from the LET laboratory, are also acknowledged for their availability and help in the mechanical tests preformed throughout this dissertation.

I would also like to express my acknowledgements to Palbit S.A., for providing the tools essential for the experimental part of this dissertation.

The projet "MAMTool - Machinability of Additive Manufactured Parts for Tooling Industry" funded by the Programa Operacional Competitividade e Internacionalização, and Programa Operacional Regional de Lisboa funded by FEDER and National Funds (FCT) is acknowledged (Reference PTDC/EME-EME/31895/2017).

I would also like to thank my colleague and friend André Couto for his continuous support and positive thinking even in the most stressful situations.

Finally, I would like to express my sincere gratitude to my family for giving me continuous encouragement and unconditional support throughout my studies. I would not be where I am without them.

Ana Chantal Leites Amaral
Porto, June 2019

# Contents


**1 Introduction** **1**
- 1.1 Project's framework and motivation . . . 1
- 1.2 Project's objectives . . . 1
- 1.3 Structure of this dissertation . . . 2

**2 Additive manufacturing review** **5**
- 2.1 Introduction and process categories . . . 5
- 2.2 Metal additive manufacturing . . . 7
  - 2.2.1 Selective laser melting . . . 8
  - 2.2.2 Materials . . . 9
- 2.3 Metallic powders . . . 11
  - 2.3.1 Powder production . . . 11
- 2.4 Processing issues and defects . . . 12
  - 2.4.1 Loss of alloying elements . . . 12
  - 2.4.2 Porosity and lack of fusion . . . 13
  - 2.4.3 Surface roughness . . . 15
  - 2.4.4 Cracking and delamination . . . 16
- 2.5 Post-processing . . . 17

**3 Metal cutting review** **19**
- 3.1 Introduction . . . 19
- 3.2 Orthogonal metal cutting . . . 19
  - 3.2.1 Mechanics of orthogonal cutting . . . 20
  - 3.2.2 Forces in orthogonal cutting . . . 22
- 3.3 Chip formation . . . 24
  - 3.3.1 Types of chip formation . . . 24
  - 3.3.2 Chip form classification . . . 26
- 3.4 Cutting tools . . . 27
  - 3.4.1 Tool materials . . . 28
  - 3.4.2 Tool geometry . . . 30
- 3.5 Cutting conditions . . . 31
- 3.6 Machining forces and power . . . 32
  - 3.6.1 Machining power . . . 33
  - 3.6.2 Specific cutting pressure . . . 33
- 3.7 Surface finish . . . 33

**4 Simulation of metal cutting** **35**
4.1 Introduction . . . 35
4.2 Model formulation . . . 35
4.3 Material laws . . . 36
4.4 Software solutions . . . 37

**5 Austenitic stainless steels** **39**
5.1 Characterization of AISI 316L stainless steel . . . 39
5.1.1 Properties . . . 39
5.1.2 Machinability . . . 40

**6 Experimental procedure** **43**
6.1 General considerations . . . 43
6.2 Preparation of samples and material characterization . . . 44
6.2.1 SLM parameters . . . 44
6.2.2 Division of the build plate and separation of the samples from the substrate 44
6.2.3 Chemical composition . . . 45
6.2.4 Microstructures and defects . . . 46
6.2.5 Roughness measurements . . . 51
6.2.6 Compression tests . . . 53
6.3 Machining . . . 55
6.3.1 Pre-machining of the samples . . . 55
6.3.2 Cutting tools . . . 55
6.3.3 Experimental apparatus . . . 58
6.3.4 Turning parameters . . . 60
6.3.5 Surface analysis . . . 62

**7 Experimental results and discussion** **63**
7.1 Machining power and cutting forces . . . 63
7.1.1 Evolution of the feed and penetration forces . . . 64
7.1.2 Evolution of the main cutting force . . . 65
7.1.3 Cutting power . . . 68
7.1.4 Specific cutting pressure . . . 69
7.2 Chip analysis . . . 71
7.3 Surface analysis . . . 76
7.3.1 Cutting tools surface analysis . . . 76
7.3.2 Workpiece surface analysis . . . 77

**8 Orthogonal metal cutting preliminary studies** **81**
8.1 Introduction . . . 81
8.2 Quick-return mechanism . . . 81
8.2.1 Kinematic analysis of a quick-return mechanism . . . 81
8.2.2 Shaping machine type L2-03.6 . . . 84
8.3 Deform$^{TM}$2D . . . 85
8.3.1 Material characterization . . . 86
8.3.2 Process parameters . . . 89
8.4 Results . . . 89
8.4.1 Load results . . . 89
8.4.2 Chip formation . . . 91

**9 Conclusions and future work** **93**
9.1 Conclusions . . . 93
9.1.1 Material characterization . . . 93
9.1.2 Machining power and cutting forces . . . 93
9.1.3 Chip forms . . . 94
9.1.4 Surface finish . . . 94
9.1.5 FEM simulation . . . 94
9.2 Future works . . . 95

**References** **97**

**A Methods for powder production** **105**

**B Codes for the turning experiments** **107**

**C Average load values of the turning experiments** **109**

**D Energy-dispersive X-ray spectroscopy** **111**

**E Technical drawings of a gripping system for mounting the dynamometer on the shaping machine** **113**

# List of Figures


2.1 General additive manufacturing process. . . . . 5
2.2 AM trend analysis. . . . . 6
2.3 SLM process schematics. . . . . 8
2.4 Controlling parameters in SLM process. . . . . 9
2.5 Process window for EBM of Ti-6Al-4V for achieving optimal deposition quality. 10
2.6 Comparison of inconel 718 powder quality from different production techniques. 12
2.7 Comparison of process induced, lack of fusion porosity, to powder induced, entraped gas porosity transferred from the feedstock. . . . . 13
2.8 SEM images of microstructural defect. . . . . 14
2.9 (a) Stair step effect; (b) SEM image of un-melted powder particles on build surface; (c) balling effect; (d) effect of heat input on surface roughness . . . . . 16

3.1 Classification of material removal processes. . . . . 20
3.2 (a) Orthogonal cutting; (b) Oblique cutting. . . . . 20
3.3 (a) Variables in orthogonal cutting; (b)Orthogonal cutting schematics. . . . . 21
3.4 Forces in metal cutting. . . . . 22
3.5 Schematics of chip formation with deformation zones. . . . . 24
3.6 Continuous chip formation. . . . . 25
3.7 Serrated chip formation. . . . . 26
3.8 Discontinuous chip formation. . . . . 26
3.9 Chip form classification in accordance with ISO 3685 standard. . . . . 27
3.10 Chip classification. . . . . 27
3.11 Cutting tool materials and their wear resistance and toughness. . . . . 29
3.12 Alternative ways for holding and presenting the cutting edge of a single-point tool. 30
3.13 Geometric elements of a single-point cutting tool insert. . . . . 30
3.14 Approximation of turning (a) by the orthogonal cutting model (b). . . . . 31
3.15 Force components in turning. . . . . 32
3.16 Influence of geometric factors on the theoretical finish of the work surface. . . . . 34

4.1 Classification of the material models for high plastic deformation. . . . . 37

5.1 Post-processing operations of SLM AISI 316L. . . . . 42

6.1 SLM built specimens attached to the substrate. . . . . 44
6.2 Schematics of the build plate division. . . . . 45
6.3 Build plate prepared for 3D scanning after mechanical cutting. . . . . 45
6.4 Schematics of the division of the cylindrical specimen. . . . . 46
6.5 Example of the image analysis process of S1.1 surface (polished surface): (a) optical microscopy image of the polished surface and (b) image after processing. 47

6.6 Optical micrographs showing pores in different regions of a section parallel to the building direction (XZ or YZ) (a) and (c), and on a section transverse to the building direction (XY) (b) and (d). . . . 47
6.7 Optical microscopy images of the microstructure revealed by chemical etching of the samples. . . . 49
6.8 Optical microscopy images after electrolytic etching, showing microstructural defects. . . . 50
6.9 Backscattered SEM images of the microstructure on a section longitudinal to the building direction. . . . 50
6.10 Optical microscopy images of the microstructures revealed by electrolytic etching. 51
6.11 (a) HommelWorke rugosimeter. Directions for the roughness measurements and specimens analyzed: (b) turning specimen and (c) orthogonal cutting specimen. . 52
6.12 Roughness profiles of the as-built state. . . . 52
6.13 SEM image of the as-built surface on a section longitudinal to the building direction. 53
6.14 Compression test specimen drawing. . . . 53
6.15 (a) Compression test specimen mounted on the compression system; (b) Test specimen before compression; (c) Test specimen after test. . . . 54
6.16 Stress-strain curves for the vertical (V) and horizontal (H) AM specimens and for the conventional (C) specimens. . . . 54
6.17 Turning test specimen drawing. . . . 55
6.18 Geometric parameters of the inserts. . . . 56
6.19 Toolholder geometrical features. . . . 56
6.20 Palbit inserts: (a)DCMW 11T304, (b) DCGT 11T304-FS. . . . 57
6.21 Schematics of the experimental setup. . . . 58
6.22 EFI DU20 conventional lathe. . . . 59
6.23 Assembly of the piezoeletric dynamometer in the conventional lathe. . . . 59
6.24 Charge amplifiera and data aquisition system used for the turning experiments . . 60
6.25 Schematics of the specimen sections for the turning experiments. . . . 60
6.26 Detail of the workpiece assembly on the conventional lathe. . . . 61
6.27 Schematics of the sections machined with different feeds for roughness measurements. . . . 62

7.1 Load spectrum of the AM 316L turning operation. . . . 63
7.2 Evolution of the feed force as a function of feed rate for the AM and conventional specimens. . . . 64
7.3 Evolution of the penetration force as a function of depth of cut for the AM and conventional specimens. . . . 65
7.4 Evolution of the cutting force as a function of cutting speed, for the AM and conventional specimens, and for the different cutting conditions. . . . 67
7.5 Cutting force spectrum of the AM and conventional 316L. . . . 68
7.6 Cutting power as a function of feed rate for the AM and conventional specimens. 69
7.7 Cutting power as a function of depth of cut for the AM and conventional specimens. 69
7.8 Cutting pressure as a function of the area of the chip section, for the conventional and AM 316L. . . . 70
7.9 Cutting pressure as a function of the area of the chip section, for the conventional and AM 316L. . . . 71
7.10 Chip geometry of the conventional material. . . . 73
7.11 Chip geometry of the AM material. . . . 74

7.12 SEM images of the chips obtained from machining with cutting tool T1, for the conventional and AM 316L. . . . 75
7.13 SEM images of the chips obtained from machining with cutting tool T2, for the conventional and AM 316L. . . . 75
7.14 SEM images showing some particularities of the AM 316L chips. . . . 76
7.15 SEM images of the cutting tools' surface. . . . 77
7.16 Surface roughness of the AM and conventional AISI 316L, after machining, as a function of the feed rate. . . . 78
7.17 Surface roughness measurements by optical profilometer of the AM specimen machined with cutting tool T1. . . . 79
7.18 SEM images of the AM specimen's surface machined with the cutting tool T2. . . . 80

8.1 Shaping machine type L2-03.6 (DEMec). . . . 82
8.2 Kinematic scheme of a planar quick-return mechanism. . . . 83
8.3 Ram velocity graphics. . . . 85
8.4 Finite element model of Deform2D. . . . 86
8.5 Flow stress curves of conventional AISI 316L for different stain rates and a temperature of 20°C. . . . 86
8.6 Flow stress curves of conventional AISI 316L for different temperatures and a strain rate of 1. . . . 87
8.7 Flow stress curves of AM AISI 316L for different stain rates and a temperature of 20°C. . . . 88
8.8 Flow stress curves of conventional AISI 316L for different temperatures and a strain rate of 1. . . . 88
8.9 Load as a function of time for both AM and conventional 316L. . . . 90
8.10 Evolution of the average load as a function of feed rate, for both AM and conventional 316L. . . . 90
8.11 Chip geometry of the conventional 316L, with the effective stress distribution. . . . 91
8.12 Chip geometry of the AM 316L, with the effective stress distribution. . . . 92

D.1 EDS analysis of cutting tool T2. . . . 112

E.1 Technical drawing of the lower plate to assemble the dynamometer on the shaping machine type L2-03.6. . . . 114
E.2 Technical drawing of the upper plate to assemble the dynamometer on the shaping machine type L2-03.6. . . . 115

# List of Tables


2.1 Experimentally determined printability of different alloys and process combinations. 11

3.1 Properties of cutting tool materials. . . . . 29
3.2 Relationship between turning operation and orthogonal cutting. . . . . 32

5.1 Chemical composition (wt%) of stainless steel 316L according to F3184-16. . . . 40
5.2 Mechanical properties of 316L austenitic stainless steel fabricated by SLM and traditionally processed. . . . . 40

6.1 Chemical composition (wt%) of 316L stainless steel. . . . . 46
6.2 Porosity results with respect to the surfaces considered. . . . . 47
6.3 Average roughness values in $\mu$m for the as-built state. . . . . 52
6.4 Inserts designation and dimensions in accordance with Palbit® turning catalogue. 56
6.5 Toolholder designation and dimensions in accordance with Palbit® turning catalogue. . . . . 56
6.6 Inserts' material grades in accordance with Palbit® turning catalogue. . . . . 57
6.7 Cutting conditions for the experiments conducted in the conventional lathe. . . . 61
6.8 Cutting conditions for surface analysis. . . . . 62

7.1 Cutting pressure of the AM and conventional 316L. . . . . 70
7.2 Chip classification in accordance with ISO 3685 standard. . . . . 72
7.3 Ideal cutting parameters for favourable chip formation for each cutting tool. . . . 72
7.4 Surface roughness after machining. . . . . 77

8.1 Shaping machine type L2-03.6 parameters. . . . . 84
8.2 Orthogonal cutting simulation parameters. . . . . 89

A.1 Methods for metal powder production. . . . . 106

B.1 Code names adopted for the turning experiments. . . . . 108

C.1 Average load values of the turning experiments. . . . . 110

# Symbols and Abbreviations

| | |
|---|---|
| $A_s$ | Shear plane area |
| $a_p$ | Depth of cut |
| ALE | Arbitary Lagrangian Eulerian |
| AM | Additive Manufacturing |
| ASB | Adiabatic shear band |
| ASBS | Adiabatic shear band spacing |
| ASTM | American Society for Testing and Materials |
| BN | Boron nitride |
| BUE | Build-up edge |
| CAD | Computer-Aided Design |
| CBN | Cubic polycristalline boron nitride |
| DED | Direct Energy Deposition |
| EBM | Electron Beam Melting |
| EDM | Electrical discharge machining |
| EIGA | Electrode induction gas atomization |
| DMLS | Direct Metal Laser Sintering |
| $f$ | Feed rate |
| $F$ | Friction force |
| $F_c$ | Cutting force |
| $F_t$ | Thrust force |
| $F_s$ | Shear force |
| $F_n$ | Normal to shear force |
| $F_f$ | Feed force |
| $F_p$ | Penetration force |
| fcc | Face centered cubic |
| FEM | Finite element method |
| HIP | Hot Isostatic Pressing |
| HSS | High Speed Steels |
| ISO | International Organization for Standardization |
| $K_c$ | Specific cutting pressure |
| LBM | Laser Beam Melting |

| | |
|---|---|
| LOM | Light optical microscope |
| MAM | Metal Additive Manufacturing |
| $N$ | Normal to friction force |
| $P$ | Cutting power |
| $P_u$ | Unit power |
| PBF | Powder Bed Fusion |
| PCD | Polycrystalline diamond |
| PCB | Polycrystalline boron nitride |
| SLM | Selective Laser Melting |
| $Q$ | Material removal rate |
| $r$ | Chip thickness ratio |
| $r_\varepsilon$ | Tool nose radius |
| $S$ | Area of the chip section |
| SEM | Scanning electron microscope |
| SS | Stainless steel |
| w | Width of cut |
| $t_0$ | Uncut chip thickness |
| $t_c$ | Chip thickness after cut |
| T | Temperature |
| $T_{room}$ | Room temperature |
| $U$ | Specific energy |
| $v_c$ | Cutting speed |
| WC | Tungsten carbide |

## Greek Symbols

| | |
|---|---|
| $\alpha$ | Rake angle |
| $\beta$ | Friction angle |
| $\gamma_w$ | Wedge angle |
| $\varepsilon$ | Plastic strain |
| $\dot{\varepsilon}$ | Plastic strain rate |
| $\dot{\varepsilon}_0$ | Reference plastic strain rate |
| $\theta_c$ | Clearance angle |
| $\mu$ | Friction coefficient |
| $\tau$ | Shear stress |
| $\phi$ | Shear angle |

# Chapter 1

# Introduction

## 1.1 Project's framework and motivation

A growing interest has been dedicated to metal additive manufacturing techniques, for the ability to produce near net shape components with high design freedom. However, these components require post-processing to achieve better surface finishes and dimensional tolerances, either by conventional or non-conventional machining. This dissertation focuses on conventional machining of additively manufactured 316L stainless steel, with the objective of unveiling the influence of the process parameters on the resulting surface integrity, cutting loads and chip control, which are determinant for the process productivity, including energetic efficiency and tool life preservation. Although there is a strong field of research on metallic powder-based additive manufactured components, when it comes to post-processing, it has yet to be properly addressed, which is part of the motivation for this project. This dissertation is part of the MAMtool research project, which aims at developing constitutive models for AM materials and predictive numerical tools for metal cutting, based upon the experimental machinability studies of these materials. This project envisages the general metalwork industry and the tooling industry, for potentiating energy efficient moulding solutions for plastic parts injection.

One of the main advantages that comes with using additive manufacturing processes for the production of mold inserts is the ability of creating conformal cooling channels within the inserts. This allows for a more efficient and fast removal of heat from the mold or die, when compared to drilled straight-line channels. With this solution the molding cycle times are reduced and the tool life prolonged, which can also contribut to improved part quality.

## 1.2 Project's objectives

The objective of this dissertation is to study the machinability of both additively and conventionally manufactured stainless steel AISI 316L, the latter serving as a basis of comparison for the AM results. There were many intermediate steps involved in achieving the final objective of the present work, that can be described as follows:

- Literature review on the topics of additive manufacturing, particularly selective laser melting, metal cutting and finite element model simulation with a special focus to those regarding AISI 316L;
- AM material characterization: metallographic studies through optical and electronic microscopy; flow stress determination through quasi-static compression tests;
- Instrumented turning experiments; study of the influence of different cutting conditions in the resulting cutting forces, chip formation and surface integrity;
- Development of a material constitutive law, from the quasi-static compression tests, for the additively manufactured AISI 316L;
- Two dimensional numerical simulations, using Deform$^{TM}$, for future studies on the machinability of AISI 316L under orthogonal cutting conditions.

## 1.3 Structure of this dissertation

Throughout this dissertation different topics are addressed, being divided into nine chapters, as follows:

- **"Introduction"**: a brief description of the project's framework and motivation, and the main goals of this dissertation;
- **"Additive manufacturing review"**: literature review on additive manufacturing, focusing on selective laser melting of metallic powders and the main material defects that could arise from this technology;
- **"Metal cutting review"**: the main aspects of metal cutting are addressed; namely the process mechanics, chip formation, cutting tools, cutting conditions, cutting forces and power and finally surface integrity;
- **"Simulation of metal cutting"**: basic principles of finite element modelling simulations;
- **"Austenitic stainless steels"**: brief description of austenitic stainless steels, with focus on AISI316L properties and machinability;
- **"Experimental procedure"**: material characterization and description of the preparatory stages for the experimental tests, including test specimens drawings, equipment used and conditions tested;
- **"Experimental results and discussion"**: analysis of the results from the turning experiments, particularly cutting forces, cutting power and specific cutting pressure, in addition to chip classification and surface integrity analysis;

- **"Orthogonal metal cutting preliminary studies"**: kinematic analysis of a quick-return mechanism, which is the basis for the 2D numerical simulation parameters; AM 316L material constitutive law identification; analysis of results from the 2D orthogonal cutting simulations, including cutting forces and chip formation;
- **"Conclusions and future work"**: summary of the main conclusions of the work and listing of possible future works.

# Chapter 2

# Additive manufacturing review

## 2.1 Introduction and process categories

Additive manufacturing (AM) is the official term, according to the ASTM and ISO standard organizations, given to processes in which material is added orderly in layers to make parts from 3D model data, in contrast to conventional subtractive manufacturing methods. This method of manufacturing appeared from the necessity of developing prototypes without the need of moulds and machining operations, thus it was firstly introduced under the name of rapid prototyping. Nevertheless, AM technologies have undergone significant developments through recent years enabling the use of these methods to manufacture functional models.

The general procedure to obtain an AM part is common to all technologies that will be explored ahead, and it begins with the three-dimensional modelling of the desired part, resorting to CAD (Computer-aided design) software. Following this, the CAD model is converted into a standard format, compatible with AM processing, such as .STL, .AMF and .3MF [1]. The processing software will then slice the model into various 2D layers, and having the file ready for the machine to read, proceeds the printing stage. After this phase, the parts undergo heat treatments and other post-processing, to remove the substrate and support structures and to give them the desired finish and mechanical properties.

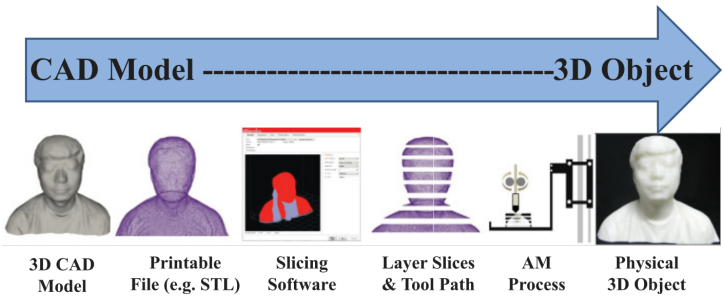


Figure 2.1: General additive manufacturing process [2].

Although AM technology was firstly developed around polymeric materials, waxes and paper

laminates, continuing developments have broadened this range, introducing composites, metals and ceramics as printable materials [3]. Moreover, in order to achieve better output results, in addition to the progress in technologies, the materials were also specifically developed to suit the different processes in AM, resulting in parts with greater accuracy, strength and durability [3]. The feedstock options for AM processes are filaments, pastes, liquids, powders, pellets and sheets.

The main sectors benefiting from AM technologies development, mainly in the metal and composite categories, are transportation, aerospace, medical and industrial [1]. Figure 2.2 represents the main industrial sectors utilizing AM technologies in the year 2018 and the range of its applications. From the chart in Figure 2.2(b) it is noticeable that AM still plays a significant role in concept modelling and prototyping being only surpassed by the fabrication of functional parts.

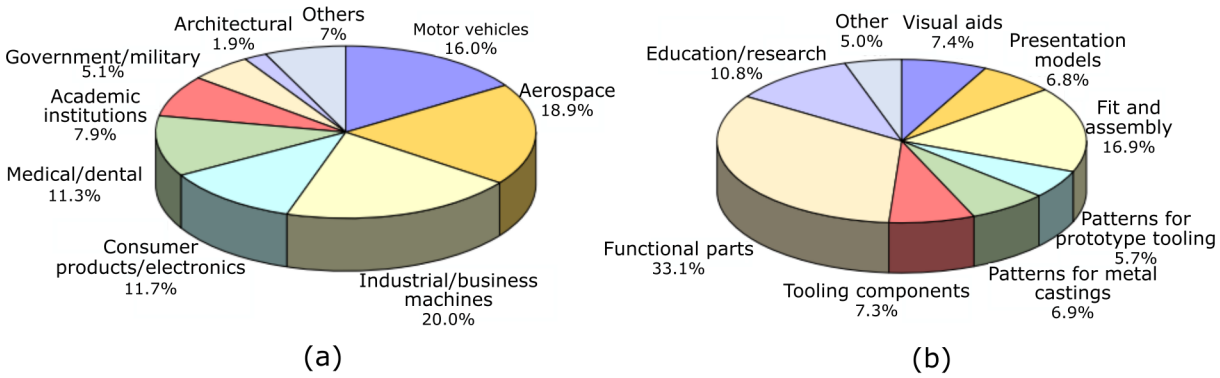


Figure 2.2: (a) Main industrial sectors that utilize AM; (b) Range of applications for AM [4].

AM is a serious contender to conventional manufacturing processes, since it enables manufacturers significant improvements in cost effectiveness and product value for unique parts or small series production. Probably the most attractive advantage to AM is the ability to produce complex geometries with a high degree of customization without the use of tools and moulds, translating into a decline in costs and lead times. Another asset is the possibility to achieve significant part weight reduction through topological optimization, which is especially attractive for the transportation sector.

The main challenges in implementing AM come from the high running costs resulting from the initial machine investment, the cost of the build material and the overall equipment maintenance, such as sieving and gas filtering systems. Moreover, the lack of knowledge about processing parameters and the difficulty in replicating the processes make manufacturers reluctant in adopting this technology. Although progress is being made in this area, there is still a deficiency in standards relating to AM parts, including materials' specifications and testing. In addition, the need of post-processing to give parts the geometrical tolerances, dimensional accuracy and surface finish, that are not otherwise found in the as-built state, is also a significant drawback of the technology.

Additive manufacturing processes are categorized into seven distinct technologies, as described by the ISO/ASTM 52900 standard [5]. The approved terminology for process categories and definitions is depicted as follows:

- **Material extrusion**: process in which material is selectively dispensed through a nozzle or orifice;
- **Material jetting**: process in which droplets of build material are selectively deposited;
- **Binder jetting**: process in which a liquid bonding agent is selectively deposited to join powder materials;
- **Sheet lamination**: process in which sheets of material are bonded to form a part;
- **Vat photopolymerization**: process in which liquid photopolymer in a vat is selectively cured by light-activated polymerization;
- **Powder bed fusion**: process in which thermal energy selectively fuses regions of a powder bed;
- **Directed energy deposition**: process in which focused thermal energy is used to fuse materials by melting as they are being deposited.

## 2.2 Metal additive manufacturing

The interest of this dissertation lies in metal additive manufacturing (MAM). This type of fabrication stands out due to its capability to process metals and metallic super-alloys practically without design constraints, a high degree of customization and more efficient usage of raw material, otherwise difficult or impossible by conventional means [6], for low-volume aerospace, medical, industrial and transportation applications [1].

Only four technologies out of the ones presented in Section 2.1 are currently utilized for metals production, namely: binder jetting, sheet lamination, powder bed fusion (PBF) and directed energy deposition (DED). The processes referred to by these categories can be divided and classified by the energy source, deposition nature and aggregate state of the feedstock, the binding mechanism between layers [7] as well as by the production times, maximum fabricated component size, ability to produce complex geometries and product quality [6]. This dissertation will focus on the most widely used technology for metals [1]: powder bed fusion.

The processes relying on PBF technologies use powder as feedstock, as the name indicates, and these powders are selectively melted by the energy input of a laser or electron beam [7]. In the case where the energy source comes from an electron beam, the process is called electron beam melting (EBM), otherwise the process utilizes a laser, thus having the name laser beam melting (LBM); also known as selective laser melting (SLM) [8] or direct metal laser sintering (DMLS) [9]. For the remaining of this dissertation SLM will be the designation adopted to refer to this process. These powder based processes are the ones that achieve better surface finish and have the ability to produce complex features, due to small-size powder particles [6].

### 2.2.1 Selective laser melting

SLM is a powder-bed based process in which a thin layer of metal powder is selectively melted by a laser beam in order to turn it into a solid slice with the desired shape of the final component [9]. Figure 2.3 represents the process chain for SLM and a set-up schematics.

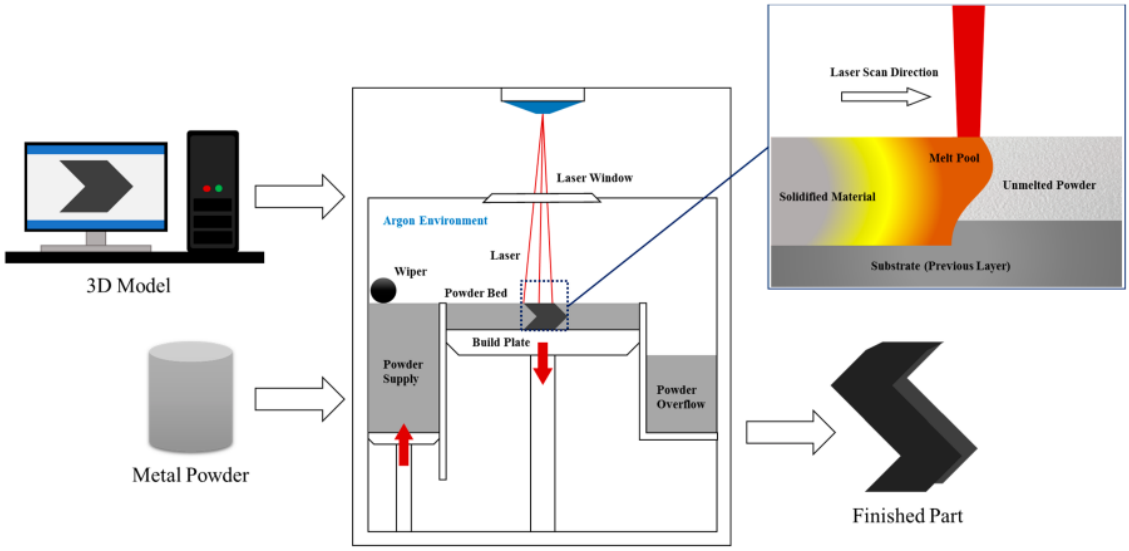


Figure 2.3: SLM process schematics [9].

In this process the metal powders are fed into the system by a hopper or a feeding system, and their uniform distribution over the build plate is ensured by a wiper or a dispersing piston and roller.

These PBF systems require a build substrate to give mechanical and thermal support to the build material, ensuring that the existing layers of material do not move when a new layer of powder is distributed [8]. SLM typically comprehends a system of lenses and a scanning mirror or galvanometer, responsible for directing the laser beam, with power between 20W and 1kW [7], across the deposited powder layer. The laser beam energy must be sufficient to ensure that the layer of powder is fully molten throughout its thickness. Furthermore, the laser path at each run follows a pattern, called the scan strategy, guaranteeing that each run overlaps the preceding one fusing the already solidified layer with the new layer, resulting in a homogeneous solid [9]. After a run is complete, the build platform is lowered by a distance of one layer thickness (20-100 $\mu$m [9]) and a new layer of powder is deposited. This process is repeated until the part is completed and at each complete turn, the unmelted powders can be sieved and re-utilized. These operations are performed in a closed chamber with a protective gas environment, either nitrogen or argon [7], to prevent unwanted reactions and oxidation.

#### 2.2.1.1 Process parameters

SLM process parameters can be grouped into four categories: (1) laser-related, (2) scan related, (3) powder-related and (4) temperature-related, as shown by the schematics of Figure 2.4.

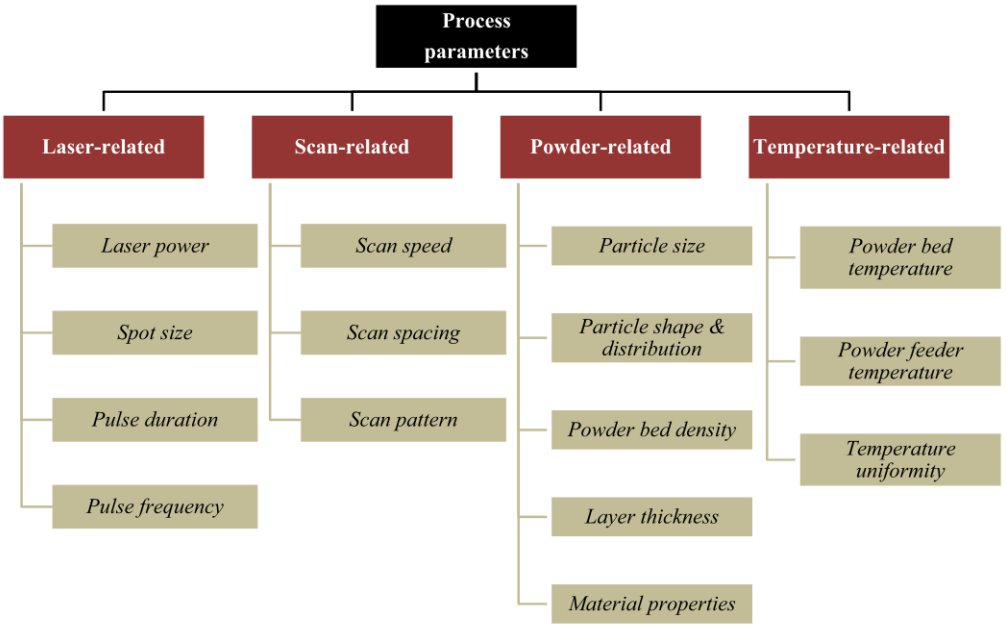


Figure 2.4: Controlling parameters in SLM process [10].

### 2.2.2 Materials

The range of metallic materials capable of being processed by AM is growing every year [4] with the development of feedstock and processing parameters. Interest is increasing in processing high performance metals through AM, which offers significant economic advantages by producing intricate components at lower costs and less waste. The following is a list of commonly processed high performance metallic materials, from the most studied groups of metals optimized for AM:

- **Titanium alloys**: commercially pure Ti, Ti-6Al-4V, Ti-6Al-4V ELI [11], Ti-24Nb-4Zr-8Sn, Ti-6Al-7Nb [7];
- **Nickel base alloys**: Inconel 625, Inconel 718, Waspalloy, Rene 41 [12], Invar 36, Haynes 230 [6], Hastelloy X, MAR-M 247, IN738LC [13];
- **Steels**: stainless steels (AISI316L, 304L, 304, 316 [6]); maraging steel (AISI 18Ni-300 [14]); precipitation hardenable steels (17-4PH, 15-5PH [7]); tool steels(H11, H13 [15], H20 [13]); high speed steel (M2 [12]).

Significant research efforts have been concentrated on Ti, Ni and Fe based alloys for various AM technologies, culminating in some well established combinations of material and processes for practical applications.

Furthermore, other metals and alloys have been studied for implementation in AM, although with fewer publications, namely: cobalt-chrome alloys for biomedical applications [16], magnesium [17], refractory alloys such as Ta based [18] and precious metals such as Au [19] in SLM in addition to magnetic alloys (e.g. Ni-Fe-V/Mo [20]) and metallic glasses (amorphous alloys) [21].

#### 2.2.2.1 Printability of metal alloys

Metallic components fabricated by AM are susceptible to defects such as residual stresses and distortion, lack of fusion and composition changes, as will be further discussed in Section 2.4, that arise depending on the material and process.

The term *printability*, in the context of MAM processing, is introduced as the ability of a feedstock material to be successfully deposited as bulk material, avoiding the above mentioned defects and thereby meeting the mechanical, metallurgical and functional performance requirements for a designated application.

Therefore, the printability of alloys can be evaluated through experimental data, by exploring one parameter at a time and finding a region within the scale of that parameter which results in a successfully deposited material [6]. An example of a printability diagram is shown in Figure 2.5, where the effects of laser power and scanning speed, on the quality of Ti-6Al-4V deposited by EBM are represented. Using a different approach, printability can be evaluated through process simulation using phenomenological models of AM validated and calibrated through experimental data.

Table 2.1 shows the printability of commonly AM processed alloys deposited by different processes, based on experimental outcomes.

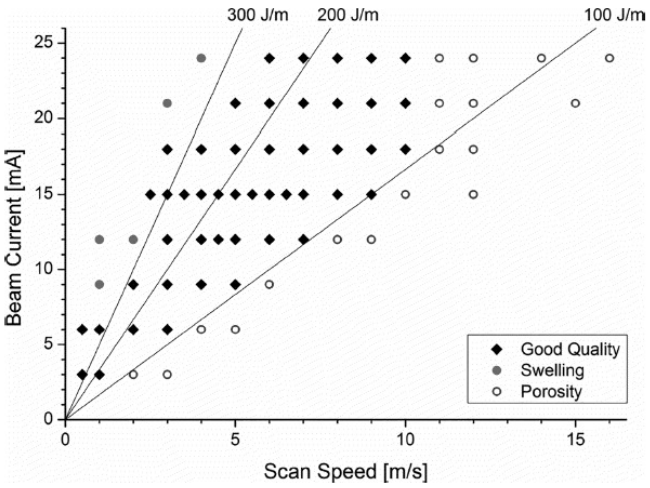


Figure 2.5: Process window for EBM of Ti-6Al-4V for achieving optimal deposition quality [22].

Table 2.1: Experimentally determined printability of different alloys and process combinations [6].

| Alloy Type | PBF-L | PBF-EB | DED-L | DED-EB | DED-PA |
|---|---|---|---|---|---|
| Aluminum | – | – | A | 2319, 4043 | A |
| AlSi10Mg | A | – | – | – | – |
| Copper-base alloys | – | – | A | Cu70-Ni30<br>Ni30-Cu70 | C |
| Magnesium | – | – | – | – | B, A |
| Nickel-base alloys | – | – | A | – | A |
| IN625 | A | – | – | 625 | |
| IN718 | A | A | – | 718 | – |
| HX | A | – | – | – | – |
| Cobalt-Chrome alloys | A | A | A | – | – |
| Precious metals | A | – | | – | – |
| Steels | – | – | A | 4043 | – |
| Maraging Steel | A | – | – | – | – |
| Stainless Steel | – | – | A | 300 Series | – |
| 316L | A | – | – | – | – |
| 17-4 PH | A | – | – | – | – |
| PH-1 (EOS) | A | – | – | – | – |
| GP1 (EOS) | A | – | – | – | – |
| CX (EOS) | A | – | – | – | – |
| Titanium | – | – | A | Ti alloys | A |
| Ti-6–4 | A | A | – | – | – |
| Ti-6–4 ELI | A | A | – | – | – |
| Grade 2 | A | A | – | – | – |
| Refractory Metals | – | – | – | Ta, W, Nb, Zr | – |
| Intermetallic alloys | B=TiAl | – | – | | – |

*A* - easily printed, quality deposit, *B* - acceptable print quality at specified parameters, *C* - restricted or poor quality, limited parameter space and *D* - not printable.

## 2.3 Metallic powders

The quality of the feedstock utilized in AM has great influence over the quality of the final component. Powder parameters such as dimension, geometry, surface morphology, internal porosity and composition determine its quality and are inherently related with physical properties, such as flowability and apparent density [23]. For AM processes a good powder flow and packing is required to ensure a homogeneous spreading and to achieve high relative density in fabricated parts.

### 2.3.1 Powder production

There are several techniques that can be implemented for the production of powders, each having its corresponding powder characteristics. Widely established techniques for metals and alloys comprise mechanical methods such as water, gas or plasma atomization; chemical and electrolytic methods and physical-chemical methods. Further information about the methods for powder production, with respect to materials and resulting powder particles characteristics can be found in Appendix A.

For the production of ferrous powders, the simplest and cheaper atomization process adopted is water atomization, in which liquid metal is atomized by water jets when flowing down the atomization chamber [7]. However, due to high process cooling rates the powder particles produced have an irregular shape, with sizes that range from 1 $\mu$m to a few millimeters [24].

In order to overcome this limitation, gas atomization can be adopted, with the added advantage of being able to produce powders of reactive metals when utilizing an inert gas (e.g. argon

or nitrogen). The heat conduction between the metal and the surrounding inert atmosphere allows the formation of spherical powder particles (Fig. 2.6, (a)) [7], with sizes between 10-500 $\mu$m [24], although exhibiting a large amount of satellites and internal porosity (Fig. 2.6, (c)), due to entrapped inert gas [23]. A variation of the gas atomization process utilized for the production of powders from highly reactive metals and alloys [25], e.g. titanium, uses electrode induction melting combined with inert gas atomization, EIGA, for the production of spherical particles.

Plasma atomization, also known as rotating eletrode atomization [25], appears as a relatively new process for the production of high purity powders from reactive metals in the form of a wire. In this process, the metal wire is atomized by plasma torches that disperse it into droplets following the solidification in powder form. This process allows the fabrication of highly spherical particles (Fig. 2.6,(a)(b)) with a low oxygen content and with a fine particle size distribution from 0-200 $\mu$m (Fig. 2.6,(c)) [25].

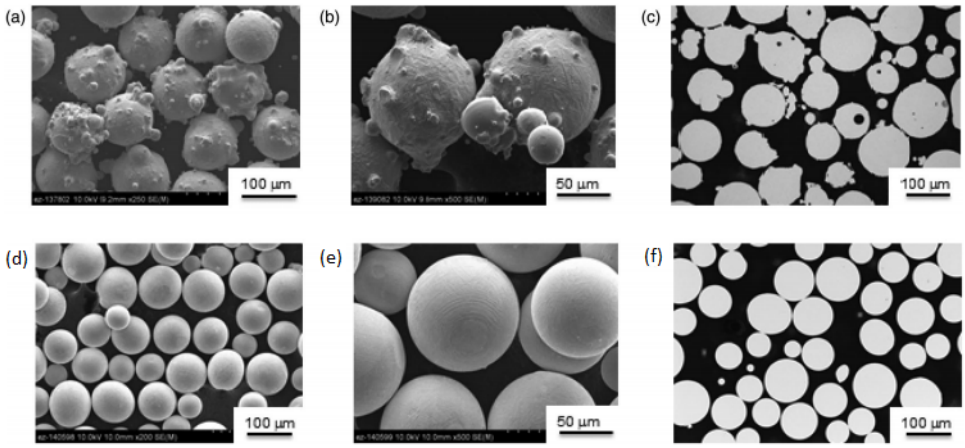


Figure 2.6: Comparison of inconel 718 powder quality produced by gas atomization (a)SEM 250x, (b)SEM 500x, (c) LOM; and plasma atomization (d)SEM 250x, (e)SEM 500x, (f)LOM. [26]

Note that spherical particles with a smooth surface, without satellites or other defects, increase powder flowability. A higher particle size distribution contributes to an increased apparent density given that finer particles fill the interstitial space between larger ones, although flowability may be affected negatively in this case [23]. The size selection for powders for AM has to be a compromise between cost and surface finish, being that the smaller the particles the better the surface finish obtained, which usually comes with a higher feedstock cost.

## 2.4 Processing issues and defects

### 2.4.1 Loss of alloying elements

In additive manufacturing processes the high molten pool temperatures have a tendency to cause selective vaporization of the more volatile elements, changing the overall composition of the

alloy. In turn, these changes in composition can affect the quality of the components by modifying the solidification microstructure, corrosion resistance and mechanical properties [6].

In laser processing, the vaporization of alloying elements occurs from the surface of the molten pool, although they are depleted from the entire volume. Therefore, in order to understand the changes in composition, an estimation of the temperature field and the molten pool geometry is required.

### 2.4.2 Porosity and lack of fusion

Porosity is a common defect in AM components that can have a negative effect on mechanical properties and can arise from solidification related phenomena or can be powder or process induced (see Fig. 2.7). The porosity that results from the solidification process is termed shrinkage porosity and appears as a consequence of incomplete flow of metal into the desired melt region [23]. Figure 2.8(d) shows a void with a layered inner morphology related to the melt pool boundaries, resulting from high residual stresses induced by rapid cooling.

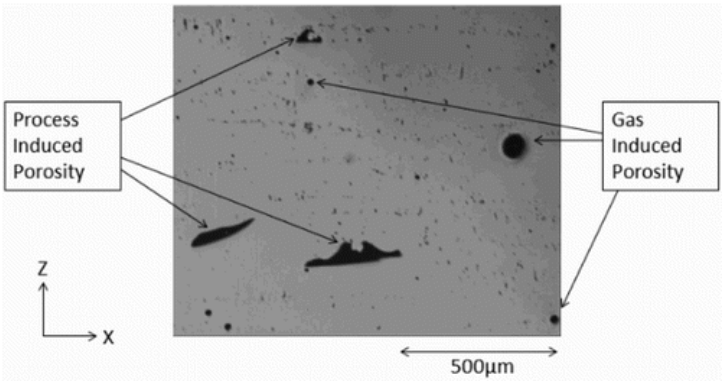


Figure 2.7: Comparison of process induced, lack of fusion porosity, to powder induced, entrapped gas porosity transferred from the feedstock [23].

Powder induced porosity is related to gases entrapped inside the powder particles resulting from the production process, as stated in section 2.3.1, that may translate directly to the deposited parts as microscopic spherical gas pores. In addition gas pores can also be process induced resulting from entrapped shielding gas or alloy vapor in the melting pool.

Moreover, most of the porosity observed in AM parts is process induced, and requires tight parameter control in order to be minimized or eliminated. When processes are operated with a low heat input, lack of fusion can occur as a consequence of inadequate penetration of the molten pool of a depositing layer into the previously deposited layers. Therefore, as the ratio of laser power to scanning speed increases, the lack of fusion porosity is minimized by increasing the pool depth (Fig. 2.8(f) and (g)), which translates into an increase in penetration depth [6].

When a very high scan speed is implemented the resultant laser path might show discontinuities related to the balling phenomenon (Fig. 2.8(c)). This effect appears as a consequence of an unstable melt pool, since high scan speeds apply more shear stress to the liquid phase leading

to higher surface tension inside the melt pool [27]. A high hatching space also results in lack of fusion voids due to insufficient overlap between laser scan tracks leading to incomplete consolidation [28].

Lack-of-fusion pores are characterized by an irregular shape and appear in a variety of sizes, from micro to macroscopic. They can be distinguished from the other types of pores for being elongated with sharp edges, acting as stress concentrators under applied loads, and by the existence of un-melted powder particles visible near the pore (Fig. 2.8(a) and (b)) [29].

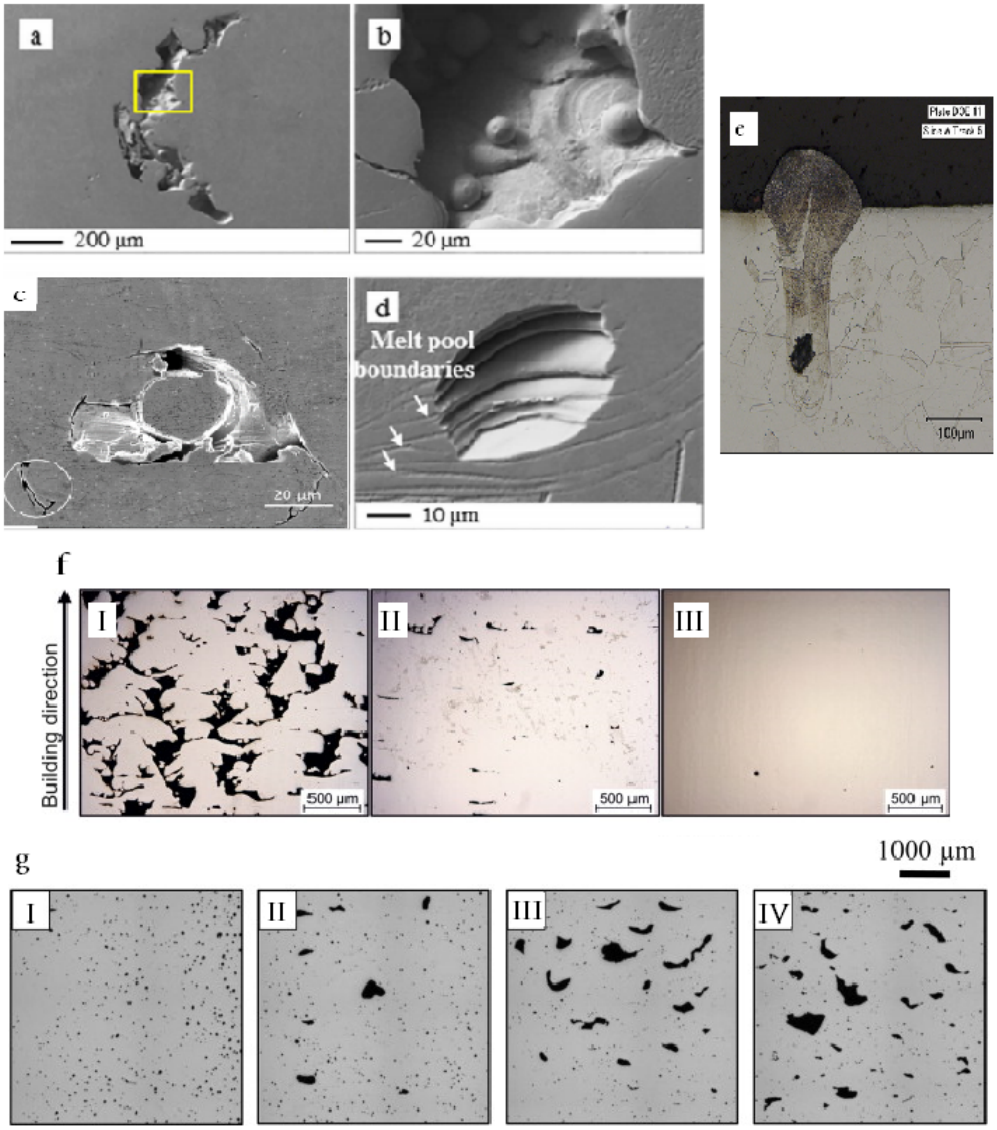


Figure 2.8: SEM images of microstructural defect:(a) low and (b) high magnification of a binding defect with unmelted 316L particles [29]; (c) balling phenomenon [27]; (d) cavity associated with residual stresses. (e) keyhole porosity [30]; (f) effect of laser power on porosity (I)90 (II)120 and (III)180W [31]; (g) effect of scanning speed on porosity (I)250 (II)500 (III)750 and (IV)1000 mm/s [10]

On the other hand, when processes are operated at very high energy density, spatter ejection

may occur and the depth of the melt pool changes from being controlled by thermal conduction to so-called keyhole mode melting [30]. In this case, the power density is sufficient to cause evaporation of the metal and form plasma which leads to the development of vapor cavities. If the keyhole mode melting is not carefully controlled, it can result in repeated formation of unstable cavities which in turn collapse and give place to a trail of voids inside the part with entrapped vapor (Fig. 2.8(e)).

### 2.4.3 Surface roughness

High surface roughness is inherent to AM, being affected not only by the process parameters but also by the feedstock, part design and post-processing resulting in either partially fused particles, improper melting or lack of fusion of layers or striations. Studies [6, 23] identify two main causes for surface roughness.

The first is related to the approximation of curved features by stepped layers, termed "stair step effect" (Fig. 2.9(a)). This effect can be diminished by decreasing the feature sizes and layer thickness which in counterpart results in a decrease in deposition rate. On the other hand AM components typically undergo post-fabrication machining to achieve the desired surface quality and dimensional requirements. Process parameters that result in an acceptable surface quality are generally time consuming which may not be adequate to ensure certain dimensional accuracies. In order to avoid counterproductive processes, a compromise of time over surface quality, followed by the component's post-processing (machining) can be an appropriate alternative.

The second cause for surface roughness can be attributed to improper melting of powder particles and the balling effect (Fig. 2.9(b) and (c)). Similar to what was stated in section 2.4.2, when the process utilizes a low heat input there is not enough energy to fully melt the particles, which in turn stick to the surfaces of the part, resulting in a surface roughness of the same magnitude as the powder particle diameter. The balling effect introduces roughness by the migration of small spherical particles, created by the breaking of the elongated molten pool, to the outer edges of the molten pool due to the flow inside being driven by the surface tension gradients. A higher heat input can be utilized to minimize these effects (Fig. 2.9(d)), keeping in mind not to reach values where the surface finish is at stake due to high thermal stresses and non-uniform solidification rates [6].

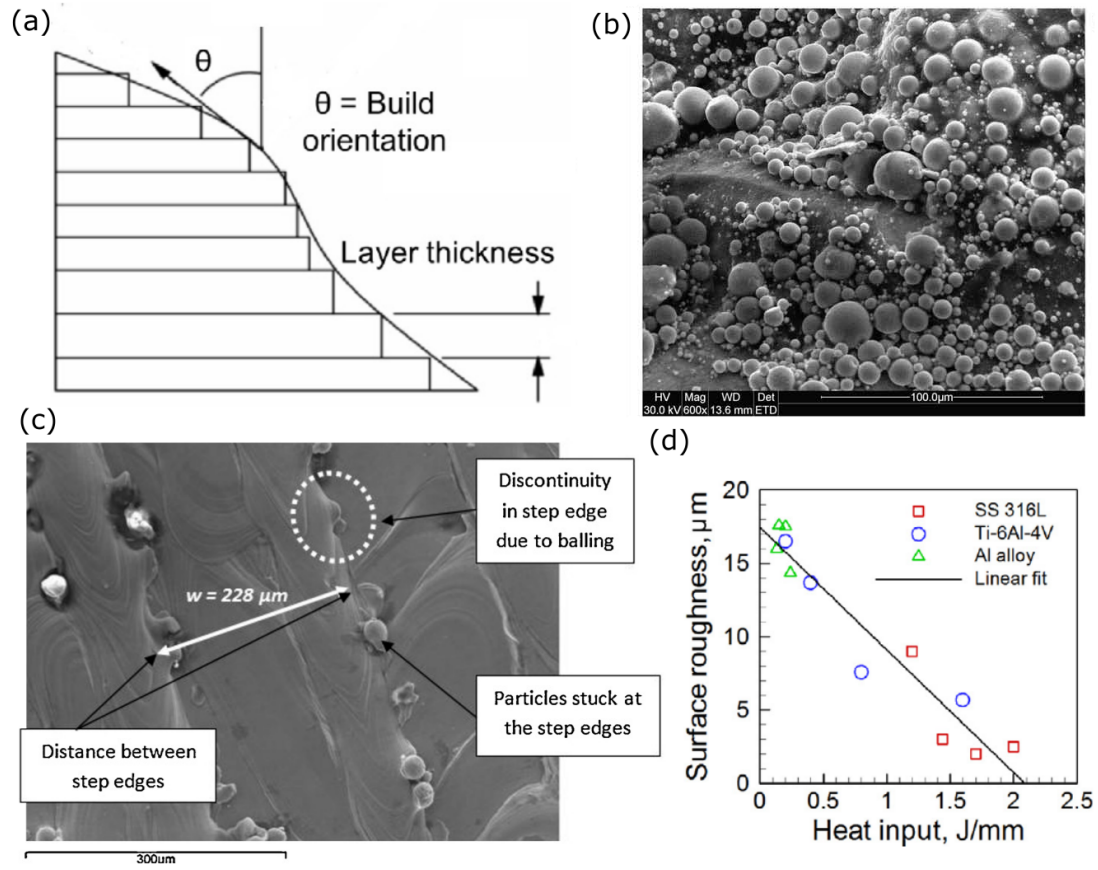


Figure 2.9: (a) Stair step effect [6]; (b) SEM image of un-melted powder particles on build surface [32]; (c) balling effect [33]; (d) effect of heat input on surface roughness [6]

### 2.4.4 Cracking and delamination

Materials in AM experience varying degrees of thermal fluctuation leading to residual stresses in the build that can translate in crack formation and delamination. Cracking of the microstructure is material dependent and may develop during solidification or subsequent heating. Regarding macroscopic cracks, these occur due to other defects such as is porosity.

There are two main types of cracking observed in AM components, namely *solidification cracking* and *grain boundary cracking* [23]. The first arises from the stresses that develop between the solidified metal in the melt pool and the metal that has yet to solidify, which can be attributed to too much energy being applied leading to large thermal stresses. The cracks develop as a result of insufficient flow of liquid due to scarce supply or obstruction by the solidified grains, and are related to the solidification nature of the material [34].

The second, *grain boundary cracking* occurs along grain boundaries of the material and depends on the precipitate phases of the metal and its grain boundary morphology [23]. It arises from rapidly heating the built material below its liquid temperature, therefore melting certain grain-boundary precipitate phases such as low melting-point carbides. These liquid films, under large residual stresses, can potentially act as crack initiation points culminating in grain-boundary

cracks in the components [34].

Delamination is the separation of two consecutive layers or a layer and the substrate, due to the residual stresses installed at the layer interfaces exceeding the yield strength of the material.

In conclusion, issues such as residual stresses and crack formation in AM can be attenuated by a combination of pre-heating, adopting the appropriate scanning strategy and parameters and post-heat treatments [13].

## 2.5 Post-processing

MAM parts must be post-processed to enhance their mechanical and geometrical properties, addressing problems such as residual stresses, undesirable microstructures and internal porosity. Post-processing can be divided into three groups: mechanical, thermal and chemical/electrochemical processes.

SLM parts should undergo a heat treatment at low temperature to relieve residual stresses, commonly prior to removal from the substrate plate [23, 35]. This treatment is normally conducted at a high enough temperature to allow atomic mobility, and rapid cooling to prevent grain recrystallization and growth. For SLM SS316L fabricated components this treatment is performed at $650^{o}$ for 2h [36].

The removal of the components from the substrate can be done by saw cutting or wire EDM, while the removal of the remaining supporting structures must be done by machining or other methods [23].

Other thermal processes such as hot isostatic pressing (HIP) can be done prior to machining. The high temperatures and pressures of the process reduce the yield strength and induce diffusivities in the material resulting in plastic deformation and recrystallization. The relative density of the as-built part is increased due to vacuum cracks and pores being closed. The denser the as-built parts are, the less the relative density increase is [37], making this process somewhat unnecessary when the SLM fabricated parts have already high density. Following this process, for SLM SS316L, a solution annealing should take place to eliminate any possible carbide formed in the slow cooling phase of HIP [36].

Other thermal processes which rely on laser surface modification technology, such as laser hardening, can be utilized to reduce surface roughness and increase surface hardness and wear resistance, leaving all other properties of the material unchanged [38].

Chemical post-processing can also be performed to achieve the desired surface finish and parameters. Through electrochemical or chemical polishing, unmelted powder particles are removed resulting in a polished surface [39].

Although these post-processing techniques contribute to an improvement of the surface quality of AM components, them alone can not achieve the high surface quality required for functional components, and for this reason, machining is still necessary in AM as a post-processing operation. In literature, there are reports of work focusing on post AM machining of metal alloys to improve

surface integrity. For example, processes such as milling [40, 41] and turning [42–44] have proved to enhance surface characteristics, such as roughness and microhardness.

In the next chapter a detailed review of the underlying aspects of machining are explored, with focus to the operations of interest to the experimental part of this thesis.

# Chapter 3

# Metal cutting review

## 3.1 Introduction

Machining is a manufacturing process in which material is removed/cut from the workpiece with a sharp cutting tool resulting in the desired shape. This dissertation will focus on the group of conventional machining (refer to Fig. 3.1), more specifically in turning operations, considering that this will be a part of the experimental procedure in this work.

Despite being a (near) net shape manufacturing process, post-processing is generally conducted after the SLM process to provide the final geometry, dimensions and finish required, not otherwise feasible by the process alone, as stated in the preceding sections.

Metal cutting processes essentially comprehend three elements; the machine tool, the cutting tool and the workpiece. A vast range of work materials is submitted to this manufacturing process, hence the need to introduce the term *machinability*, similar to the concept of *printability* presented in section 2.2.2.1. It refers to the ease with which a material can be machined using appropriate tooling and cutting conditions.

Machinability is difficult to predict because of the great amount of variables involved in the process, from the material properties of the workpiece to the inherent process characteristics, such as high temperatures, strains and stresses as well as complex friction conditions. It can be quantified as a function of (1) tool life, (2) tool forces and power consumption, (3) surface finish and (4) ease of chip disposal [45].

In this chapter the principles and underlying parameters of the machining process will be discussed, allowing for further understanding of the quantification of machinability.

## 3.2 Orthogonal metal cutting

Researchers in the metal cutting field continuously attempt to develop an analysis of the cutting process to enable the understanding of the mechanisms involved. But, to date, none of the available models can be stated to be the correct solution due to the inherent complexities of the process.

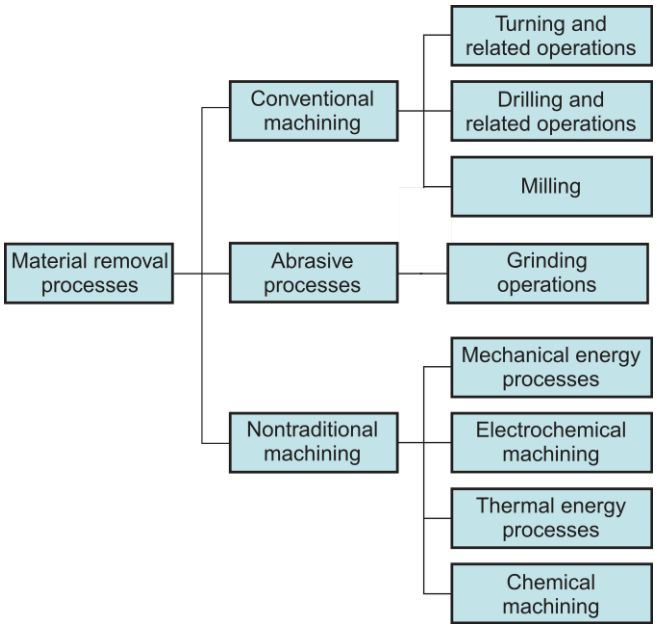


Figure 3.1: Classification of material removal processes. Adapted from [46].

Metal cutting processes, such as milling or turning, are three dimensional and are termed as oblique cutting. This designation comes from the angle between the cutting speed and the cutting edge of the tool (Figure 3.2(b)), that translates into an additional force component. Although this model depicts most processes in a more realistic way, for analysis purposes it introduces complexity when compared to the orthogonal cutting model (Figure 3.2(a)), favoured by most researchers when analyzing the chip removal fundamentals [47].

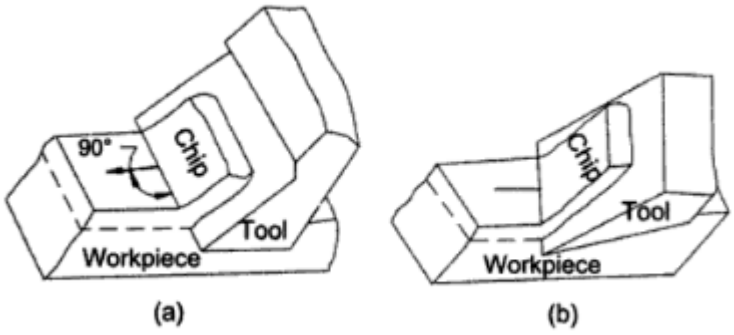


Figure 3.2: (a) Orthogonal cutting; (b) Oblique cutting [47].

### 3.2.1 Mechanics of orthogonal cutting

Orthogonal cutting can be adopted as a simplified model of material removing processes, as mentioned above, overcoming the complexities of the process and at the same time describing it in

a reasonable way. In this model only two dimensions play an active role in the analysis, although the majority of the machining processes are three dimensional.

In orthogonal cutting the effective cutting direction and consequently the effective cutting velocity, is perpendicular to the cutting edge of the tool as shown in Figure 3.3 (b).

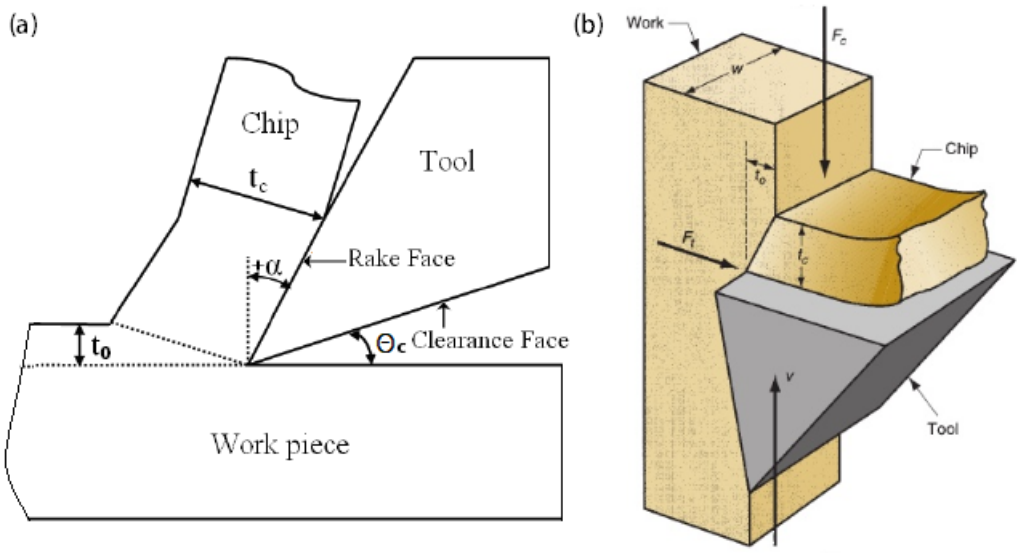


Figure 3.3: (a) Variables in orthogonal cutting [48]; (b) orthogonal cutting schematics. [46]

The chip of metal with a width (w) and an uncut chip thickness ($t_0$) is sheared from the workpiece through the action of the cutting tool. This model assumes the material removal process to be uniform along the cutting edge, therefore it is a two dimensional plane strain problem in which the action of the tool translates into a resultant force applied at its edge. This force is composed by the cutting force ($F_c$) and thrust force ($F_t$), in the direction of the velocity and the uncut chip thickness, respectively.

The relevant angles for orthogonal cutting are the rake face angle ($\alpha$), clearance angle ($\theta_c$) and the wedge angle ($\gamma_w$), angle between the rake and clearance faces (Figure 3.3(a)). The rake angle influences the direction of the chip flow and can be positive or negative, depending on the inclination of the rake face relative to the vertical dashed plane (positive angle in Figure 3.3(a)). Positive rake angles generally mean lower cutting forces, but at the same time increases the possibility of tool breakage. The clearance angle allows for friction reduction between the tool flank and the newly generated surface, thus preventing deterioration of the surface.

It is possible to geometrically define the shear angle ($\phi$) as a function of the rake angle and the chip thickness ratio ($r$) (Equation 3.2 [46]), that in turn is the ratio of the uncut chip thickness and the chip thickness after being cut ($t_c$) (Equation 3.1 [46]).

$$r = \frac{t_0}{t_c} \tag{3.1}$$

$$tan\phi = \frac{rcos\alpha}{1 - rsin\alpha} \tag{3.2}$$

### 3.2.2 Forces in orthogonal cutting

Resorting to the orthogonal cutting model, several forces can be defined (see Figure 3.4), and based on these forces, shear stress, friction coefficient and other relationships can be established.

The relationship between the various forces, based on Merchant's thin shear plane model, follows the assumptions that [47, 49]:

- The work material is ideally plastic, homogeneous and isotropic; has negligible strain hardening;
- Plastic deformation occurs exclusively in the shear plane, where the stresses are uniformly distributed;
- A continuous chip is produced with no build-up edges;
- Plane strain conditions are applicable; the width of the chip remains equal to that of the workpiece.

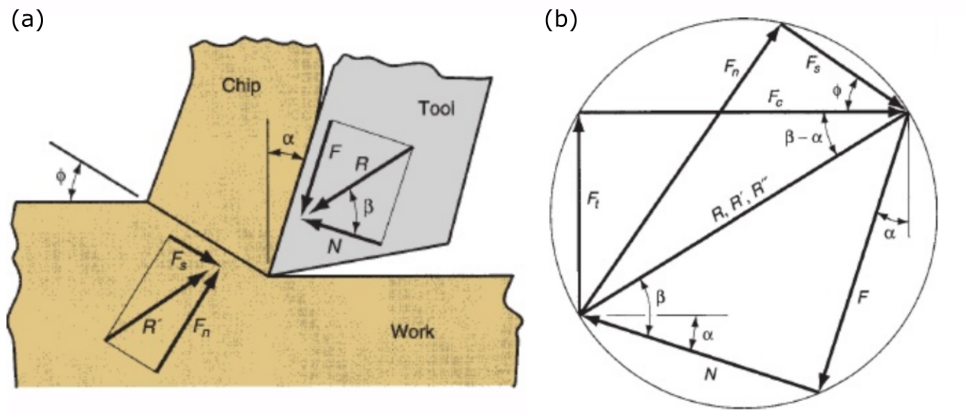


Figure 3.4: Forces in metal cutting: (a) forces acting on the chip in orthogonal cutting; (b) force diagram showing geometric relationships between forces acting on the chip and on the tool [46].

According to the simplifications assumed by this model, toghether with Merchant's forces circle diagram shown in Figure 3.4(b), relationships between three pairs of forces, the ones acting on the chip (Figure 3.4(a)) and the other acting on the tool, can be derived.

The forces applied against the chip by the tool can be separated into two mutually perpendicular components; the friction force ($\vec{F}$), that represents the resistance experienced by the chip when sliding along the rake face of the tool, and its normal ($\vec{N}$). The ratio of these two forces is known as the friction coefficient ($\mu$) between the tool and the chip.

In addition to these forces, there are two more force components acting on the chip, in this instance applied by the workpiece, namely the shear force ($\vec{F_s}$), that represents the necessary force to shear the material on the shear plane, and its normal ($\vec{F_n}$).

From Figure 3.4(b) equations can be derived to relate the four force components that cannot be measured to the two forces that can be measured; the forces acting on the tool, thrust ($\vec{F_t}$) and cutting ($\vec{F_c}$) forces [46, 47, 49]:

On the shear plane, shear force and its normal can be indicated as:

$$F_s = F_c \cos\phi - F_t \sin\phi \tag{3.3}$$

$$F_n = F_c \sin\phi + F_t \cos\phi \tag{3.4}$$

Whereas the friction force and its normal can be decomposed as:

$$F = F_c \sin\alpha + F_t \cos\alpha \tag{3.5}$$

$$N = F_c \cos\alpha - F_t \sin\alpha \tag{3.6}$$

The determination of feed and cutting forces, by means of experimental cutting tests allows for calculating these four forces (Eq. 3.3 to 3.6), and based on these estimates, shear stress and friction coefficient can be determined.

Friction coefficient and friction angle ($\beta$) are given as:

$$\mu = \frac{F}{N} = \frac{F_t + F_c \tan\alpha}{F_c - F_t \tan\alpha} \tag{3.7}$$

$$\beta = \tan^{-1}\mu \tag{3.8}$$

While the shear stress ($\tau$) that acts along the shear plane between the chip and the workpiece is defined as:

$$\tau = \frac{F_s}{A_s} \tag{3.9}$$

where $A_s$ is the area of the shear plane, calculated as:

$$A_s = \frac{t_0\, w}{\sin\phi} \tag{3.10}$$

By combining Eqs. 3.3, 3.9 and 3.10, shear stress can be expressed as:

$$\tau = \frac{F_c \cos\phi - F_t \sin\phi}{t_0 w \,/\, \sin\phi} \tag{3.11}$$

The shear angle ($\phi$), represents the direction at which the shear stress is equal to the shear strength of the material, thus shear deformation occurs at this angle. For that, the work material will choose a shear angle that minimizes energy. This gives way to the Merchant's relationship, obtained by deriving the shear stress in Eq. 3.11 with respect to $\phi$ and setting it to zero:

$$\phi = \frac{\pi}{4} - \frac{1}{2}(\beta - \alpha) \tag{3.12}$$

## 3.3 Chip formation

The conclusions drawn in Section 3.2 were based on Ernst and Merchant's theory which presents some limitations when portraying the metal cutting operation. More recent models tried to improve cutting representation by considering a deformation region, identified as primary shear zone, instead of a single plane [46, 47]. Figure 3.5 illustrates this more realistic deformation mechanism in machining.

The predominant cutting operation in machining implies shear deformation of the work material, resulting from the penetration of the cutting edge of the tool into the workpiece, which in turn shears material over the primary shear zone to form a chip.

In addition to shear deformation occurring in the primary shear zone, the chip is subjected to an additional shearing action resulting from friction between the chip and the tool (in the secondary shear zone) as the chip slides along the rake face [46].

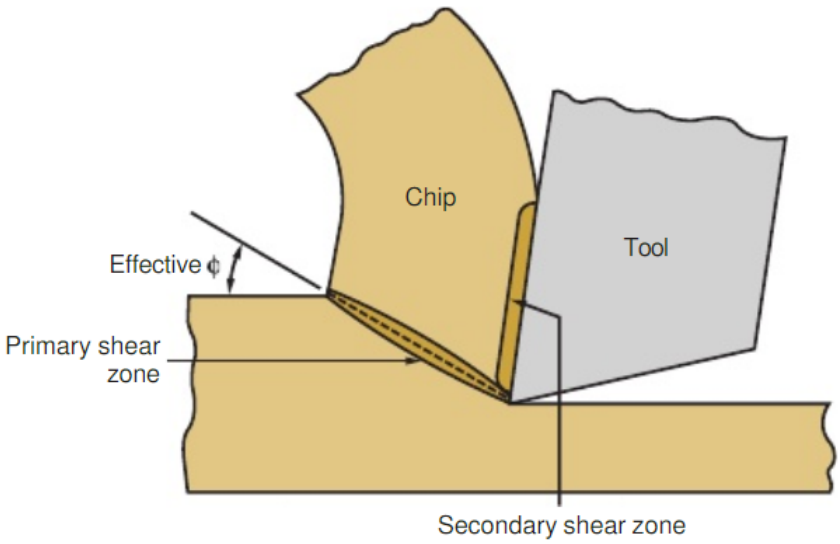


Figure 3.5: Schematics of chip formation with deformation zones [46].

### 3.3.1 Types of chip formation

It is possible to obtain a variety of chip shapes and sizes from the machining processes, depending on tool geometry, cutting conditions and work material. The chip formation in metal

cutting can be generally categorized into three types: (1) continuous chip, (2) serrated chip and (3) discontinuous chip.

#### 3.3.1.1 Continuous chip

This type of chip is characteristic when cutting ductile materials (e.g. low carbon steel, copper, brass and aluminum [50]) at high cutting speeds with low friction between the tool and chip. Some conditions that promote continuous chip formation (Fig. 3.6(a)) are sharp cutting edges, low feed rates and large positive rake angles [47].

When the friction between tool and chip is high, some particles of chip may adhere to the tool rake face near the tool tip, forming what is called build up edges (BUE). The occurrence of BUE is encouraged by high temperature and pressure conditions that culminate in its growth and subsequent breakage. Some of the broken portions of BUE get embedded into the machined surface leading to poor surface finishes (Fig. 3.6(b)).

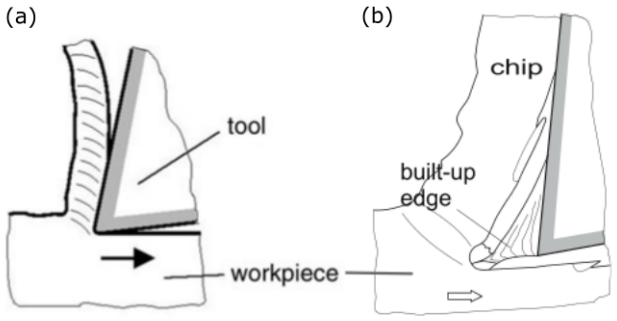


Figure 3.6: (a) Continuous chip formation [49], (b) with build up edge [51].

This type of chip poses a problem with chip disposal. As a solution, various forms of chip breakers exist in the market in the form of a step or groove in the tool rake face. These chip breakers promote the rupture of the chip into smaller pieces that can be easily disposed of.

#### 3.3.1.2 Serrated chip

This type of chip, also referred to as *shear-localized* [46], is considered semi-continuous, characterized by a saw-tooth appearance (Figure 3.7). It results from a cyclical chip formation, alternating between high and low shear strain. It is common for certain difficult-to-machine metals (e.g. titanium alloys, nickel-base superalloys and austenitic stainless steels) when machined at high cutting speeds.

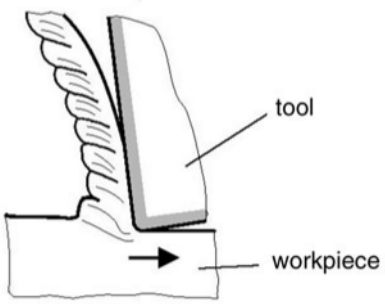


Figure 3.7: Serrated chip formation [49].

#### 3.3.1.3 Discontinuous chip

This type of chip is characteristic for brittle materials (e.g. cast irons) when machined at low cutting speeds. The shearing chip formation (Fig. 3.8(a)) is distinguished for developing into separate segments and is promoted by negative rake angles, large depths of cut and materials with limited ductility. The tearing type (Fig. 3.8(b)) corresponds to the rupture of the chip when the ductility of the material is exceeded. These types of chip formation result in an irregular texture on the machined surface.

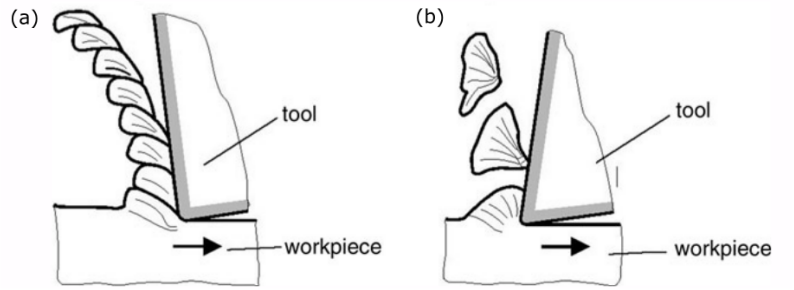


Figure 3.8: Discontinuous chip formation [49]: (a) shearing; (b) tearing type [49].

### 3.3.2 Chip form classification

The most commonly obtained chips in machining are shown in Figure 3.9, and they can be classified into eight groups in terms of size and shape. Long chips in the form of ribbon chips, snarled chips and flat helical chips are considered disadvantageous to the process since they pose hazards to the operator, tools, workpieces and the machine tool, whereas spiral chips and helical chip segments are the most favourable (Figure 3.10).

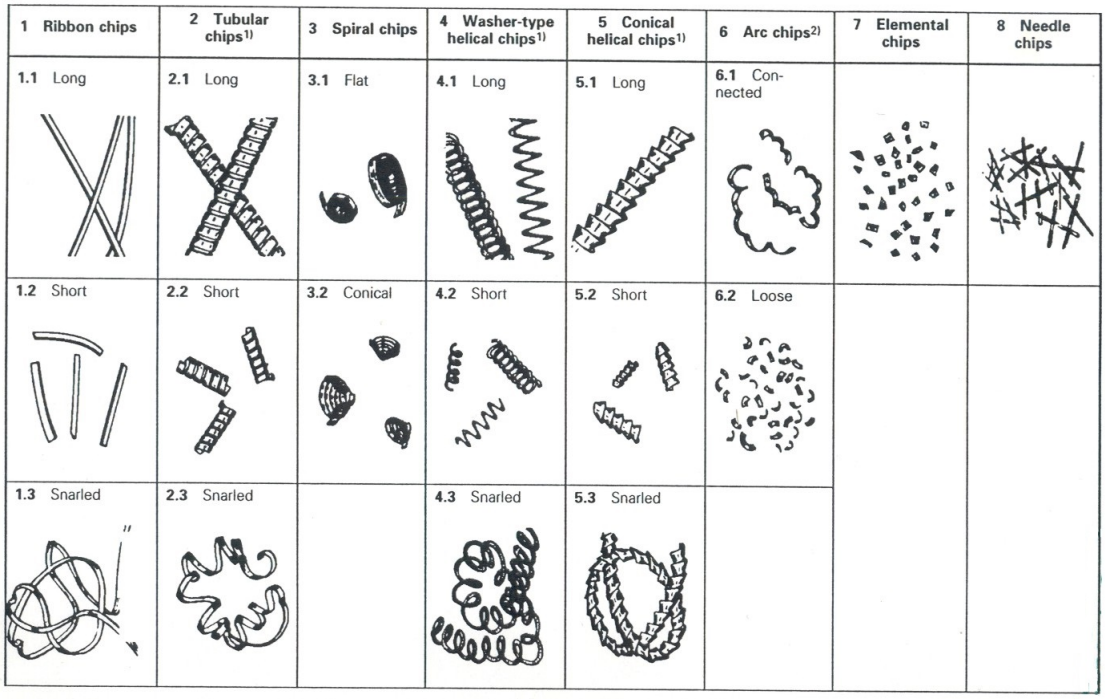


Figure 3.9: Chip form classification in accordance with ISO 3685 standard.

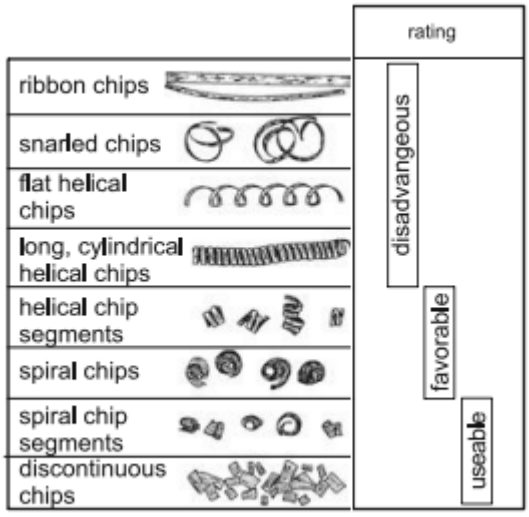


Figure 3.10: Chip classification [52].

## 3.4 Cutting tools

The cutting tools used for metal cutting must withstand the high cutting forces and temperatures inherent to the processes. When cutting forces are too high it results in the fracture of the tool, while high temperatures lead to softening of the tool and subsequent failure. Besides these causes, the tool can also fail due to continual wear of the cutting edge.

In the following sections, the main aspects of the cutting tools will be addressed, first its material, giving emphasis to that indicated for machining of austenitic stainless steels, and then its geometry.

Concerning the material, it must ensure the tool resistance to the forces, temperatures and wearing of the processes. As for the geometry of the tool, it must be developed in accordance with the work material and the machining process in question.

### 3.4.1 Tool materials

Tool materials have to meet certain requirements to guarantee a long tool life and a good process accuracy. Hardness at high and low temperatures, toughness, chemical stability and wear resistance are among those desired requisites [53]. However it is not possible to fulfill all requirements at the same time, since an increased material hardness implies a lower toughness and vice versa. Figure 3.11 shows the relationship between various tool materials in relation to wear resistance (hardness) and toughness. The tool materials can be categorized in five different groups [46, 53]:

(1) High speed steels (HSS): high alloyed steels (alloy content up to 35%);

(2) Cemented carbides (also called *sintered carbides*): class of hard tool material fabricated from tungsten carbide (WC) by powder metallurgy techniques with cobalt (Co) as a binder. Can also have TiC, TaC and/or NbC in addition to WC;

(3) Cermets, defined as composites of ceramic and metallic materials, containing TiC , TiN and other ceramics, except for tungsten carbide WC;

(4) Ceramics, manufactured by sintering metal oxides, nitrides and carbides. Normaly composed of fine-grained aluminum oxide ($Al_2O_3$) and silicon nitride ($Si_3N_4$)

(5) Ultra-hard materials, such as mono-crystalline diamond, polycrystalline diamond (PCD) and cubic crystalline boron nitride (CBN).

Commercially, cemented carbides and cermets dominate the market since they present the best balance between toughness and hardness (Table 3.1) [46, 55].

In accordance with the ISO 513 standard, the work materials are divided into groups depending on their characteristics, and for each group the insert manufacturers assign the tool materials that produce better results. For austenitic stainless steels (group M) the recommended cutting material by the insert manufacturer catalogs are cemented carbides and cermets, both coated and uncoated [55].

A thin layer (or layers) of a wear resistant material is applied to a cemented carbide insert, resulting in what is called *coated carbide*. The coating materials; commonly titanium carbonnitride (TiCN), titanium carbide (TiC), titanium nitride (TiN) and/or aluminum oxide ($Al_2O_3$), are applied to the substrate by chemical vapor deposition (CVD) or physical vapor deposition (PVD), with a thickness range of 2.5 to 13 $\mu$m, since thicker coatings tend to be more brittle [46].

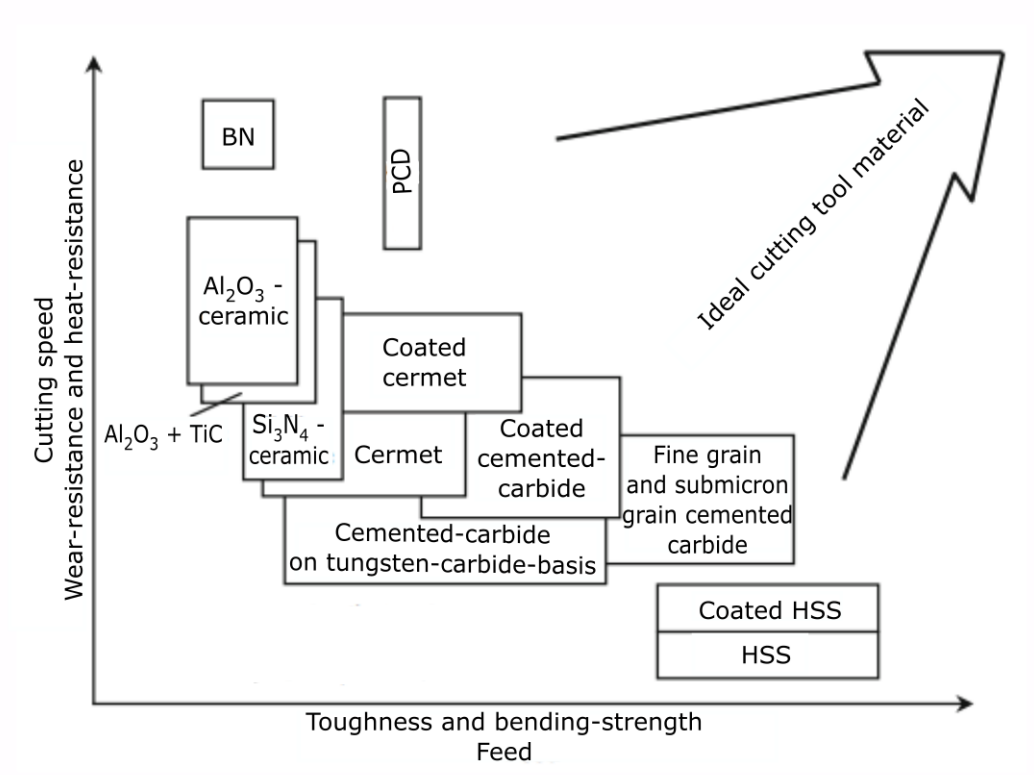


Figure 3.11: Cutting tool materials and their wear resistance and toughness. Adapted from [54].

Table 3.1: Properties of cutting tool materials [53].

| | HSS | Carbide | Ceramic | PCB | PCD |
|---|---|---|---|---|---|
| Density [g/cm$^3$] | 8.0-8.8 | 6.0-15.0 | 3.8-7.0 | 3.4 | 3.5 |
| Hardness HV 30 | 750-1000 | 1300-1700 | 1400-2400 | 4500 | 7000 |
| Young modulus [GPa] | 260-300 | 430-630 | 300-400 | 680 | 890 |
| Melting point [°C] | 1300-1400 | 1300 | 1700-2050 | 2700 | 3700 |
| Temp. stability [°C] | 600-800 | 800-1200 | 1300-1800 | 1500 | 600 |
| Temp. expansion coeff. @room temp. [$10^{-6}$] | 9-12 | 5-7.5 | 7.4-9 | 3.6 | 0.8 |
| Compression strength [GPa] | 2.5-3.5 | 4.0-5.9 | 2.5-4.5 | 4.0 | 3.0 |
| Bending strength [MPa] | 2000-3800 | 800-2200 | 300-700 | 600 | 300 |

Physical vapor deposition is a process in which a material is converted into its vapor phase in a vacuum chamber and then condensed onto a substrate surface. Chemical vapor deposition results from the interaction between a heated substrate material and a mixture of gases, leading to chemical decomposition of some of the gas constituents and the establishment of a solid film on the substrate surface [46].

### 3.4.2 Tool geometry

The cutting tool geometry varies according to the machining process. Cutting tools can be divided into single point tools and multiple-cutting-edge tools. For turning operations the first type is used.

Figure 3.12 shows the alternative ways for holding the cutting edge of a single-point tool in position: (1) solid tool, usually for HSS; (2) brazed insert, used for cemented carbide; (3) mechanically clamped insert, typical for cemented carbides, ceramics and other hard materials. Cutting tool inserts are the most common choice for machining for being economical and versatile.

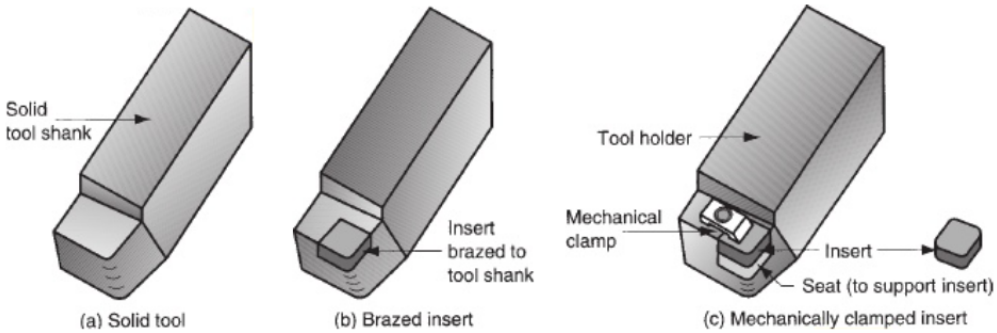


Figure 3.12: Alternative ways for holding and presenting the cutting edge of a single-point tool: (a) solid tool; (b) brazed insert;(c) mechanically clamped insert [46].

Concerning the insert's geometry, Figure 3.13 shows seven geometric elements that can be distinguished, namely: true rake angle, side flank angle, cutting edge inclination, back relief angle, side cutting edge angle, end cutting edge angle and corner radius ($r_\varepsilon$).

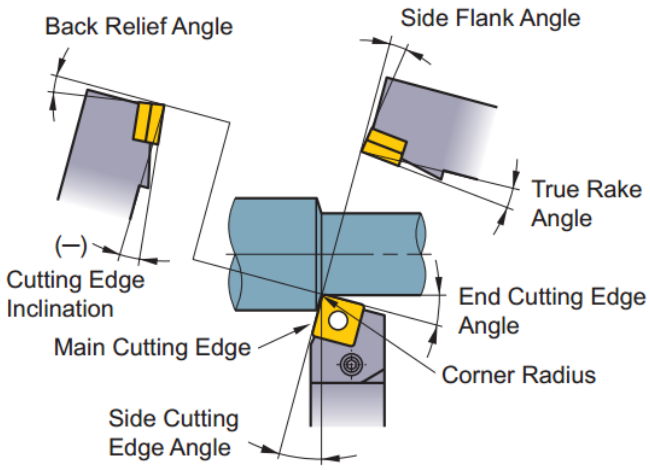


Figure 3.13: Geometric elements of a single-point cutting tool insert [55].

The rake angle has large effects on cutting resistance and temperature, chip disposal and tool life. Negative rake angles are used for hard work materials, while positive ones are chosen for easy-to-machine soft materials, and when the workpiece or machine have poor rigidity. Flank

angle provides a clearance between the tool and workpiece, preventing friction between the two, thus resulting in a smooth feed. When cutting edge strength is required, this angle should be decreased, whereas for machining work hardening materials the opposite should happen. The side cutting edge angle reduces impact load by increasing the chip contact length, thus dispersing the cutting forces on a longer cutting edge, resulting in increased tool life. This angle should be decreased when machining thin, long workpieces to prevent them from bending. The end cutting edge angle provides a clearance between the tool (end cutting edge) and the machined surface, thus preventing deterioration by rubbing and friction. The cutting edge inclination also has an important influence on the cutting process: negative angles increase the cutting edge strength and result in the disposal of the chip in the direction of the workpiece, whereas for positive ones the opposite is observed. The corner radius influences the cutting edge strength and the surface finish, as will be discussed in Section 3.7. A larger radius improves the cutting edge strength and decreases wear on the rake and flank faces.

Certain types of chips (analyzed in Section 3.3.2) pose a hazard to the machine operator and the surface quality, hence the necessity for their disposal. To this end, chip breakers are frequently used to force the chips to curl tightly and consequently cause them to fracture [46].

## 3.5 Cutting conditions

In the preceding sections the orthogonal cutting model was adopted as a means of explaining the material removal processes, but at this stage it is relevant to show the approximation of turning operations to this model. In order to understand the conversion of the cutting conditions from one model to the other refer to Figure 3.14 and Table 3.2.

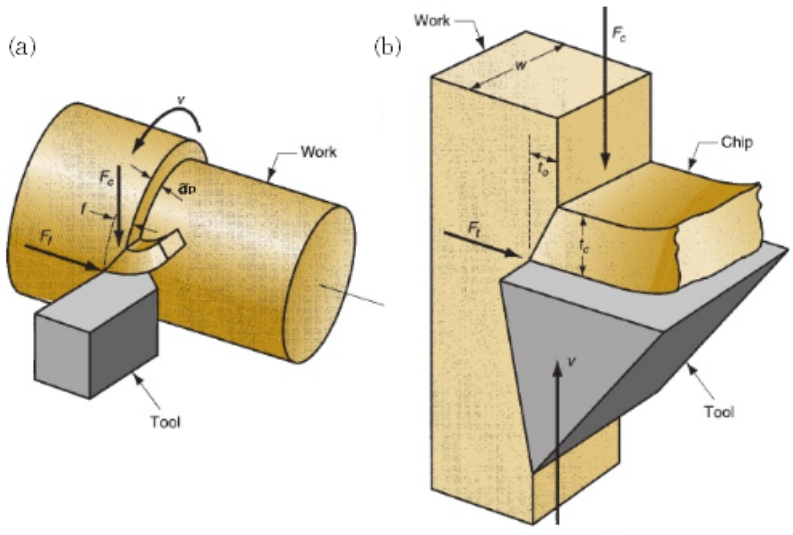


Figure 3.14: Approximation of turning (a) by the orthogonal cutting model (b) [46].

The cutting conditions, namely cutting speed $v_c$ [m/min], feed $f$ [mm/rev] and depth of cut $a_p$ [mm], are chosen in conformity with the machining operation to be performed, the cutting tool

Table 3.2: Relationship between turning operation and orthogonal cutting. Adapted from [46].

| **Turning** | | **Orthogonal cutting** |
|---|---|---|
| Feed rate, $f$ | = | Uncut chip thickness, $t_0$ |
| Depth of cut, $a_p$ | = | Width of cut, $w$ |
| Cutting speed, $v_c$ | = | Cutting speed, $v_c$ |
| Feed force, $F_f$ | = | Thrust force, $F_t$ |

and the work material properties, with the goal of achieving the best relation between productivity and surface finish. Generally, for finishing operations, a higher cutting speed is utilized with lower values for feed and depth of cut, so that the desired surface finish is achieved. Whereas for rough turning operations the opposite is confirmed, with the intent of increasing the volume of material removed per unity of time, also known as *Material Removal Rate, Q*:

$$Q = v_c \times a_p \times f \tag{3.13}$$

## 3.6 Machining forces and power

As verified in the previous section, it is possible to link turning with orthogonal cutting supported by the fact that the side cutting edge accounts for the majority of material removal, meaning that the influence of the tool nose radius and cutting edge are negligible [49].

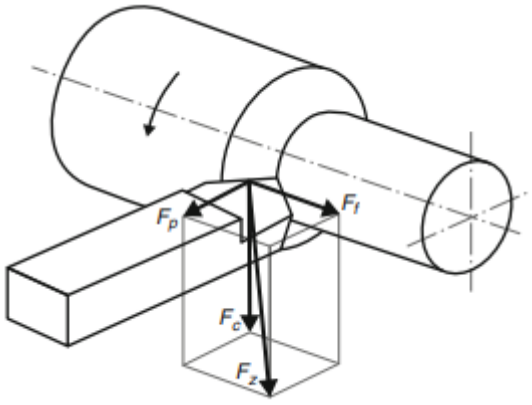


Figure 3.15: Force components in turning [49].

In turning operations, the resultant force that acts on the tool ($F_z$) can be decomposed into (Figure 3.15): feed force ($F_f$), radial or penetration force ($F_p$) and tangential or cutting force ($F_c$). The value of each of these components is dependent on the work material, the cutting tool geometry, cutting conditions and on the cutting angle and the area of the chip section.

The most effective way of force control is to change the depth of cut and feed; lower values lead to a decrease in cutting force which in turn contributes to an increased tool life. The cutting speed does not have a great influence on the cutting force; increasing the cutting speed could slightly

reduce this force component. When changes in the cutting parameters are not possible, forces can be controlled by the cutting tool geometry, in particular the rake angle; positive rake angles result in lower cutting forces, but on the other hand increase the possibility of tool fracture [49].

There is an increased interest in determining these parameters, in particular the cutting force, not only to derive the machining power needed for the operation, but also to study the tool wear that arises from the process.

### 3.6.1 Machining power

Specific power can be utilized to estimate the motor power needed to perform an operation for a given material. The power required for cutting is calculated as [49, 50]:

$$P = F_c \times v_c \tag{3.14}$$

Equation 3.14 only refers to the force and velocity in the tangential direction because, as aforementioned, in the radial and axial direction contributions are either null or negligible.

### 3.6.2 Specific cutting pressure

For evaluating the process' efficiency, it is useful to convert power into power per unit of material removal rate $Q$ (Eq. 3.13), called *unit power,* $P_u$, also known as *specific energy* $U$, defined as [46]:

$$U = P_u = \frac{P}{Q} = \frac{F_c}{a_p\, f} \tag{3.15}$$

Which is the same as specific cutting pressure, $K_c$ [N/mm$^2$], that depicts the relationship between the tangential force and the area of the uncut chip section, $S$, as follows:

$$K_c = \frac{F_c}{S} \tag{3.16}$$

where,
$S = f \times a_p$ [mm$^2$]

The value for $K_c$ can be experimentally determined, resorting to appropriate instrumentation, by determination of the tangential force. This value varies considerably with the work material and is affected by the cutting tool, cutting conditions, among other variables.

## 3.7 Surface finish

The surface finish of the machined workpieces is influenced by different factors that can be grouped as: (1) geometric factors, (2) work material and (3) vibration and machine tool factors [46].

The surface quality can be measured in terms of surface roughness resorting to a rugosimeter. From this, the values for the arithmetical mean deviation of the assessed profile $R_a$, the maximum height of the profile $R_{max}$, and the average distance between the highest peak and lowest valley $R_z$ can be measured.

The theoretical surface roughness, $R_{ta}$ and $R_{tmax}$, can be derived from Equations 3.17 [46] and 3.18 [56]. These equations only account for the geometric factors, particularly the nose radius $r_\varepsilon$ and feed rate $f$, being that they represent the determining factors for surface finish.

$$R_{ta} = \frac{f^2}{32\, r_\varepsilon} \tag{3.17}$$

$$R_{tmax} = \frac{f^2}{8\, r_\varepsilon} \tag{3.18}$$

From Figure 3.16 (a) it is possible to observe the influence of the nose radius; for the same feed rate a larger nose radius causes the feed marks to be less pronounced leading to a better surface finish. Whereas Figure 3.16 (b) depicts the influence of the feed rate; with a fixed nose radius a larger feed rate increases the separation between feed marks resulting in an increased roughness. All of these assumptions for the theoretical roughness values are corroborated by the previous equations.

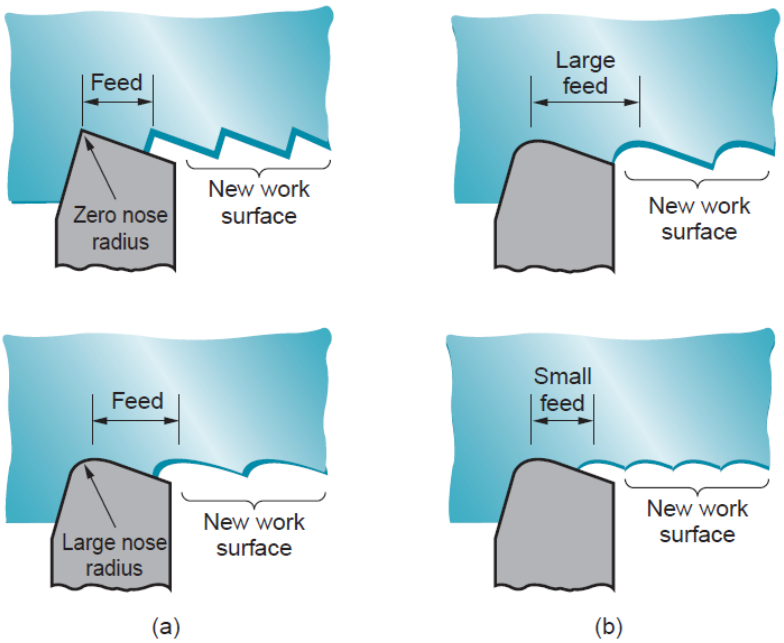


Figure 3.16: Influence of geometric factors on the theoretical finish of the work surface: (a) nose radius, (b) feed rate [46].

# Chapter 4

# Simulation of metal cutting

## 4.1 Introduction

Metal cutting processes comprise high strains, strain rates and temperatures, that associated with numerical complications make numerical modelling challenging. Finite element models (FEM) allow for simulating metal cutting processes with intricate tool geometries while taking into account the complex material behaviour under cutting conditions. This is a well established numerical method for finding approximate solutions to continuous field problems [54], that features important advantages, counted as follows:

- Material properties are commonly treated as strain, strain rate and temperature dependent;
- Freedom for modelling nonlinear geometric boundaries (e.g free surfaces);
- Enables predicting various process outputs, such as cutting forces, stresses, strain rates, temperatures, chip type, etc.
- Possibility of modelling different tool chip interactions, such as multiple friction/tribological definitions.

Other approaches for determining the ideal cutting conditions and tool geometries that resort to simplified analytic methods hold the advantage of providing a quick representation of the processes, however they have limited applications and are not suitable for describing complex processes, as is metal cutting.

In this chapter, the underlying aspects of finite element method for numerical simulation of metal cutting are explored, with emphasis to those relating with Deform$^{TM}$2D, namely in what concerns discretization strategies and material constitutive laws.

## 4.2 Model formulation

The Lagrangian and Eulerian approaches are the most common for discretizing the continuum in FEM. In the Lagrangian formulation, the finite element mesh attributed to the workpiece

deforms with the material. This approach is broadly used in metal cutting simulation for having the ability to determine chip geometry, from the initial stage to the steady state, as a function of cutting parameters, plastic deformation and material properties. Adding to the possibility of defining chip separation criteria to simulate discontinuous chips or material fracture [57]. Besides its advantages, this model has a disadvantage that arises from the severe plastic deformation involved in metal cutting, that in turn results in the distortion of elements, thus requiring remeshing. This drawback can be overcome by using an updated Lagrangian formulation with mesh adaptivity or automatic remeshing technique [48, 57].

In the Eulerian formulation, the mesh is spatially fixed, therefore requiring fewer elements for the analysis, which results in a reduction in computation time. With this model, cutting is simulated from a steady state and there is no possibility of chip separation modelling. One drawback that arises from this is the need to determine the boundaries and shape of the chip prior to the simulation [57]. In addition, the chip thickness, tool-chip contact length and contact conditions must be kept constant during analysis using the Eulerian approach.

The Arbitary Lagrangian Eulerian (ALE) technique is a combination of the above approaches that enables an independent motion for the mesh in relation to the material, as long as the domains under consideration remain the same [45].

## 4.3 Material laws

The material laws for FEM analysis can be divided into two groups (Figure 4.1): material models without elastic behaviour, that consider the material rigid until the elastic limit is reached, and the material models with elastic behaviour [54]. The first group translates into faster calculation and enables the acquisition of satisfactory simulation results for applications where the amount of elastic deformation is negligible comparing to plastic deformation. The latter are of interest when elastic deformation is not negligible.

The material constitutive laws for metal cutting simulation must be capable of adequately representing the deformation behaviour under high and low strain rates, within a broad range of temperatures and account for hardening and softening processes [58]. These material models are normally calibrated through experimental data from material testing under a relevant range of loads and conditions. Owing to the high strain and strain rates involved in metal cutting, several orders of magnitude higher than those involved in conventional compression and tensile testing [54, 58], it is desirable to have a material model that can be extrapolated outside the calibration range. From this, a physically based plasticity model is favoured over a phenomenological model, since it takes into account the physical aspects of deformation coupled with microstructural evolution, thus having a larger application domain.

Material laws for the simulation of metal cutting must describe the material flow stress, or instantaneous yield strength at which the material starts to plastically deform [57], as a function of strain, strain rate and temperature. The most widely used constitutive equations in metal cutting

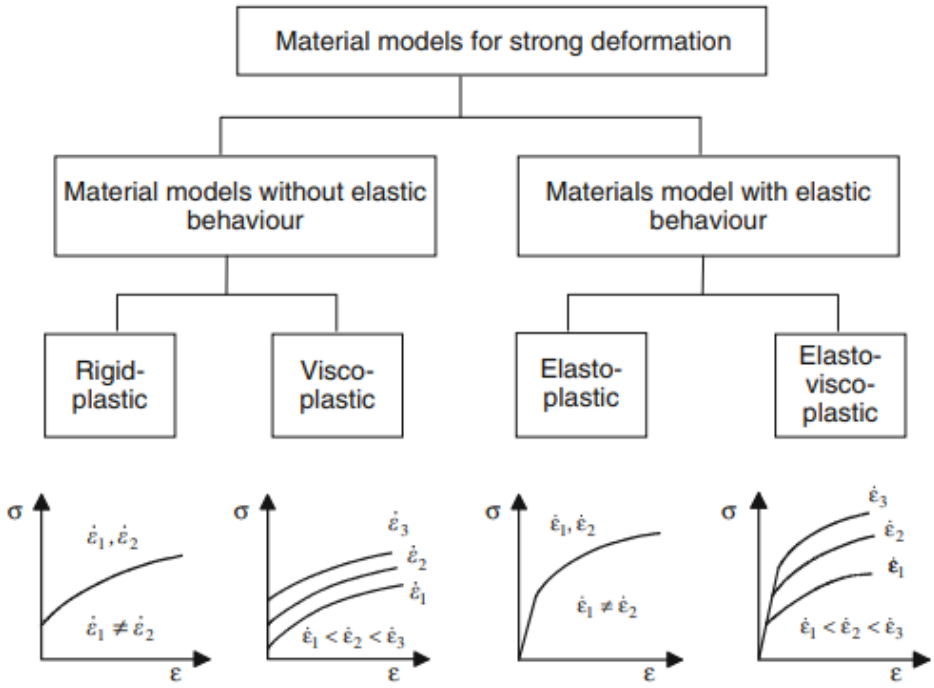


Figure 4.1: Classification of the material models for high plastic deformation [54].

are Oxley, Johnson-Cook and Zerilli-Armstrong; the first two being phenomenological based plasticity models and the third a physically based model. This thesis focuses on the most frequently implemented material model, the Johnson-Cook:

$$\sigma = (A + B\varepsilon^n) \cdot \left[1 + C \cdot ln\left(\frac{\dot{\varepsilon}}{\dot{\varepsilon}_0}\right)\right] \cdot \left[1 - \left(\frac{T - T_{room}}{T_{melt} - T_{room}}\right)^m\right] \tag{4.1}$$

In Equation 4.1, $\sigma$ is the flow stress as a function of equivalent plastic strain $\varepsilon$, equivalent plastic strain rate $\dot{\varepsilon}$ and temperature $T$. $T_{room}$ corresponds to the room temperature, $T_{melt}$ is the melting temperature of the workpiece material, $\dot{\varepsilon}_0$ is the reference equivalent plastic strain rate and $A$, $B$, $n$, $C$ and $m$ are material constants, predetermined based on flow stress data from the mechanical tests. In this material model, the first factor corresponds to the material strain hardening, while the second, corresponds to the viscosity term representing the increase in yield stress for high strain rates, concluding with the thermal softening term, which depicts the decrease in yield stress due to local thermal effects.

## 4.4 Software solutions

There are several finite elements programs that are customized for the simulation of metal cutting, thus enabling an easier setup and run of simulations, but at the same time, this specialized programs have a limited number of parameters that the user can modify. SFTC/DEFORM$^{TM}$and ADVANTEDGE$^{TM}$are examples of commercially available softwares for metal cutting simulations that include machining modules for easier interaction with the user.

For increased simulation flexibility, general purpose software, such as Abaqus™or Ansys are preferred [54]. These programs are suitable for a broader range of applications, but at the same time they are not as user friendly as specialized programs, therefore requiring a large amount of experience and time for setting up a model capable of portraying the desired phenomenon.

# Chapter 5

# Austenitic stainless steels

Austenitic stainless steels are the most widely used grade of stainless steels (SS) for general applications. They are extremely formable and weldable and can be strengthened by cold working, precipitation hardening or through the addition of nitrogen [59]. They have excellent toughness and strength which is maintained over a wide range of temperatures, and are distinguished by being non-magnetic.

Austenitic grades have a chromium content between 16-25% which renders them high corrosion resistance, and a maximum of 1.2% carbon. The combination of nickel, manganese, carbon and nitrogen in their composition stabilizes the austenitic face centered cubic structure (fcc).

On account of their exceptional properties and due to their wide applications in marine, biomedical, fuel cell, construction and automobile sectors [60, 61], there is growing interest in processing these alloys via AM, in particular the 316L grade, which is one of the most investigated materials for SLM [60, 62].

## 5.1 Characterization of AISI 316L stainless steel

The chemical composition of stainless steel type 1.4404 (316L) is shown in Table 5.1, in accordance to ASTM A276 standard. This grade is characterized by a low carbon content (<0.03%) resulting in a high resistance to grain boundary carbide precipitation. The addition of 2-3% of molybdenum increases the corrosion resistance, in particular the ability to resist pitting and cracking under aggressive environments. Manganese is added as a partial replacement for the relatively expensive nickel to stabilize the austenitic structure. Although this grade is characterized by a low carbon content, grain boundary precipitation can still occur at the high temperatures involved in AM processing, where some of the chromium reacts with carbon to produce chromium carbide while diminishing the chromium content of the surface [59].

### 5.1.1 Properties

In contrast to what has been stated for conventionally processed austenitic steels, when produced by AM, they often contain a small amount of ferrite. This is due to the rejection of solute at

Table 5.1: Chemical composition (wt%) of stainless steel 316L according to F3184-16.

| Element | C | Mn | P | S | Si | Cr | Ni | Mo | Fe |
|---|---|---|---|---|---|---|---|---|---|
| Min | | | | | | 16.0 | 10.0 | 2.0 | Bal. |
| Max | 0.030 | 2.00 | 0.045 | 0.030 | 1.00 | 18.0 | 14.0 | 3.00 | |

the solidifying interface, which causes the intercellular regions to be enriched with chromium and molybdenum resulting in the formation of ferrite [6]. Its content can be lowered by increasing the cooling rate, since there is less time for solute redistribution.

In general, as-built AM austenitic stainless steels present finer microstructures when compared to their conventionally manufactured counterparts, with refined grains due to rapid solidification and dendritic and cellular structures, thus resulting in increased hardness, yield and ultimate strengths and lower ductility [6, 63].

SLM processed austenitic stainless steel exhibit a slight anisotropy of properties, resulting from the anisotropy of their microstructure, with elongated grains and dendrites often oriented along the build direction. Typically their yield and ultimate strengths are higher in the longitudinal direction (Table 5.2) or otherwise approximately equal [6]. Moreover, the SLM produced 316L stainless steel exhibits higher yield and ultimate strengths, when compared to the conventional one (Table 5.2).

Table 5.2: Mechanical properties of 316L austenitic stainless steel fabricated by SLM and traditionally processed [6, 64].

| Process | Yield strength [MPa] | Tensile strength (UTS) [MPa] | Elongation [%] | Hardness HV |
|---|---|---|---|---|
| *Additive manufactured* | | | | |
| SLM | X-Y 624<br>Z 561 | | X-Y 31.0<br>Z 19.0 | 250-275 |
| SLM | X 534±6<br>Y 528±4<br>Z 444±27 | X 653±3<br>Y 659±3<br>Z 567±19 | X 16.2±0.8<br>Y 16.6±0.4<br>Z 8.0±2.9 | |
| SLM | X-Y 602±47<br>Z 557±14 | X-Y 664±7<br>Z591±12 | X-Y 30±0<br>Z 42±2 | 235 |
| SLM | X-Y 379±17<br>Z287±6 | X-Y 489±28<br>Z317±11 | x-Y23±6<br>Z 7±4 | |
| *Traditionally manufactured* | | | | |
| Forging | 170-290 | 480-560 | 40 | |
| Annealed | 241 | 586 | 50 | 215-225 |

### 5.1.2 Machinability

Austenitic steels are more challenging to machine when compared to ferritic or perlitic steels, due to their low thermal conductivity, high work hardening rates, high strength and ductility. This

translates into high tool wear rates, rough surface qualities and unfavorable chip geometries, such as ribbon and snarled chips [65].

Their low thermal conductivity results in high temperatures in the tool chip interface, which in turn triggers thermal wear mechanisms that can lead to the formation of craters on the rake face. This happens because the surrounding workmaterial is not able to absorb the heat generated in the deformation zones fast enough.

An approach to improve the chip formation and breakage, by lowering the applied deformations in the workpiece, is utilizing a small cutting edge radius, which at the same time increases the surface quality and inhibits the formation of burrs [65].

To address the tool wear problems, tools with hard coatings should be used, which also contributes to the resistance against the formation of build-up edges. As to choosing the method to synthesize the coating system, it should be taken into account that the high temperatures of the chemical vapor deposition (CVD) may diminish the fracture toughness of the cemented carbide tools, whereas the lower temperatures of the physical vapor deposition (PVD) enable retaining sharp cutting edges [65].

Cutting fluids are commonly used when machining austenitic stainless steels to provide lubrication between the tool and the chip and remove the heat generated in the shear zones.

In literature, some studies [43, 44] have already addressed post SLM fine machining of 316L stainless steel, focusing on the surface aspects, such as roughness, microhardness, microstructure, phase transformation, etc. It is reported a decrease in surface roughness to one quarter of the as-built average roughness, after fine-finishing in dry conditions [44]. Although this process results in high surface quality, other processes such as drag finishing and vibratory surface finish (Fig. 5.1) are recommended for post-processing of additive manufacturing parts [44], due to the limitations of fine machining in components with complex geometries.

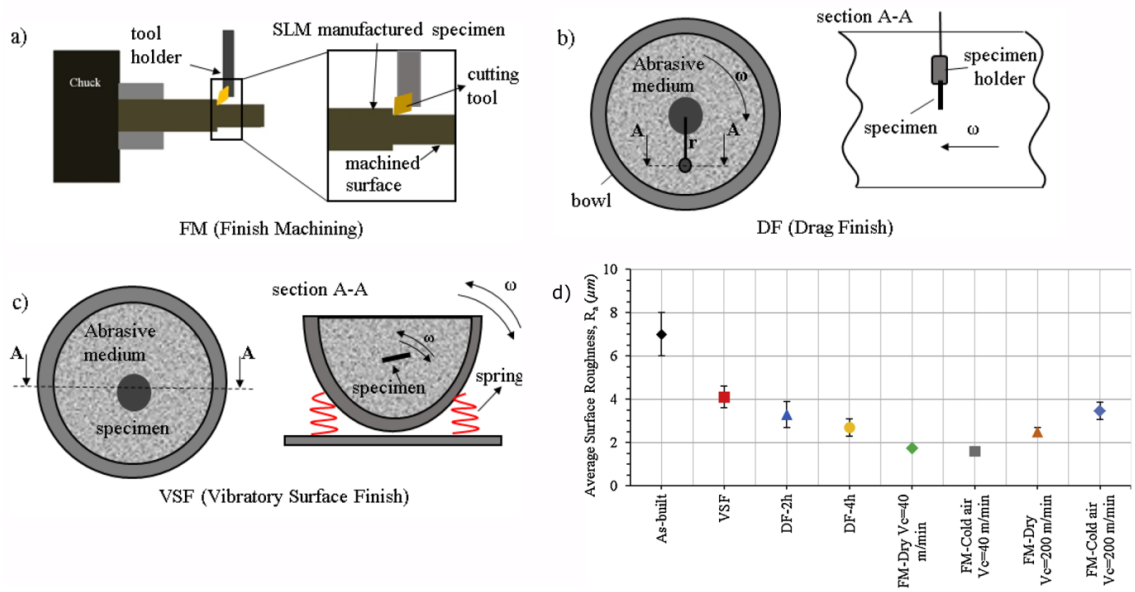


Figure 5.1: Post-processing operations of SLM AISI 316L: a) finish machining, FM, b) drag finish, DF, c) vibratory surface finish, VSF; d) resulting Ra after post-processing and their comparasion with the as-built [44].

# Chapter 6

# Experimental procedure

## 6.1 General considerations

The experimental part of this dissertation focuses on the machinability study of 316L stainless steel both additively and conventionally manufactured, as a means for comparing the SLM material with the wrought one in terms of surface finish and mechanical properties. Samples were subjected to external turning operations, in a conventional longitudinal lathe. Distinct parameters were considered, so that their influence could be studied in terms of cutting forces, surface finish and chip formation. In addition, cylindrical specimens where also subjected to quasi-static compression tests in order to characterize the material flow stress.

The specimens to be studied, produced by AM, were provided by an outside entity and came attached to the building substrate. Besides the compression and turning specimens, the build plate included different geometries which are outside of the scope of this thesis (multiaxial fracture and orthogonal cutting specimens). Initially a 3D scanning was performed on the build plate to compare with the digital files and infer on eventual distortions during the build. Following this, the division of the build plate into the different groups of samples took place, and a new 3D scanning was conducted to evaluate possible distortions.

The specimens where then separated from the substrate by milling of the buildplate up until the specimens surfaces. Samples of the material in the as-built state were characterized through metallography and mechanical testing, as well as the wrought material, to allow for comparison between the two. Microstructure and porosity were observed through optical and electronic microscopy and the surface roughness was measured with a rugosimeter.

In this chapter a description of the equipment and techniques used throughout the experimental part is given, as well as the results of preliminary experiments that enabled the material characterization for the proposed work.

## 6.2 Preparation of samples and material characterization

### 6.2.1 SLM parameters

Figure 6.1 shows the result of the SLM process (laser powder bed fusion, L-PBF), with the different geometrical specimens attached to a steel building plate. The selective laser melting of austenitic stainless steel 316L was carried out by a ytterbium laser with an average power of 200W and a spot size of 70 $\mu$m. The layer thickness of melted powder in a single pass was 50 $\mu$m. The studies that follow were conducted on the specimens as received from the SLM process, without any subsequent heat treatment.

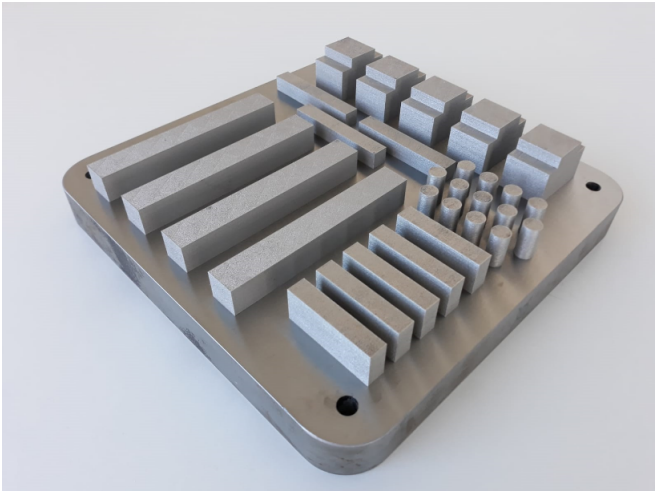

Figure 6.1: SLM built specimens attached to the substrate.

### 6.2.2 Division of the build plate and separation of the samples from the substrate

The build plate containing the AM specimens was divided into groups of equally geometric samples as shown in Figure 6.2, this being achieved by cutting with a mechanical saw, and the result is shown in Figure 6.3.

The samples were then separated by end milling the substrate until they were free, after which they were grinded to ensure a sound surface and parallel top and bottom surfaces. This was not the first choice for this stage; instead wire EDM was considered, but this option proved to be too expensive. Other options like mechanical cutting (tangential to the specimens base) were also discarded since they resulted in considerable material waste, given that the available saw showed tooth wear after 5 mm thickness cut.

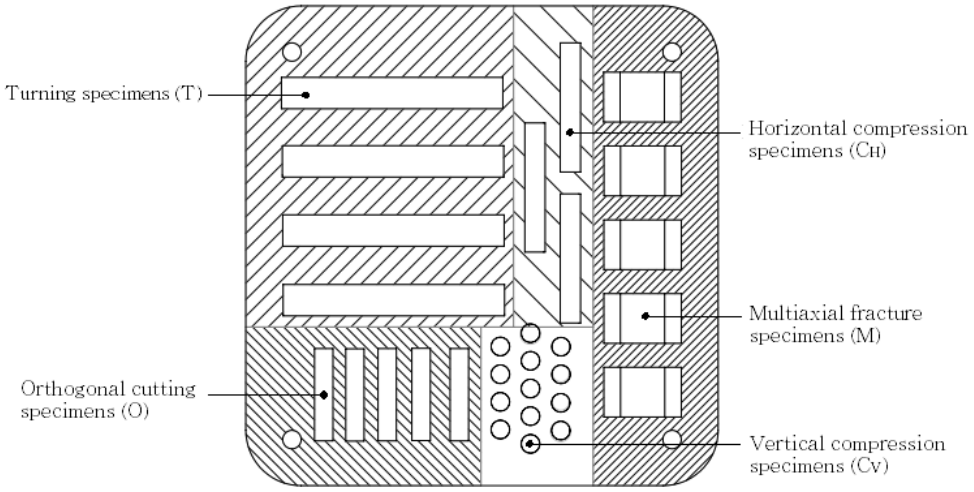


Figure 6.2: Schematics of the build plate division.

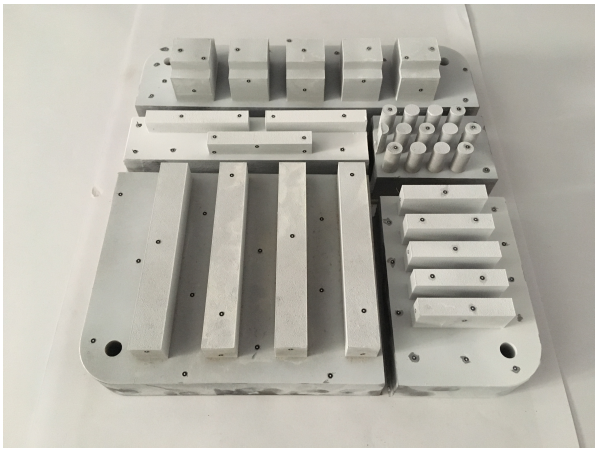

Figure 6.3: Build plate prepared for 3D scanning after mechanical cutting.

### 6.2.3 Chemical composition

For the characterization of 316L stainless steel, measurements of its chemical composition through spark emission spectroscopy, both for the conventional and AM material (Table 6.1), were performed in SPECTROMAXx equipment. It was verified that both the conventional and the additively manufactured 316L meet the chemical composition specified in F3184-16 Standard (Table 5.1).

The Mn content of the AM material is relatively lower compared to the conventional one, mainly because Mn is an alloying element with a melting temperature lower than steel. Hence during the SLM process this element may volatilize due to the high temperatures inherent to the process, as explained in Section 2.4.1. Nevertheless, the accuracy of this measurement has associated errors that may cause deviations in the chemical composition.

Table 6.1: Chemical composition (wt%) of 316L stainless steel.

| Element | C | Mn | P | S | Si | Cr | Ni | Mo | Fe |
|---|---|---|---|---|---|---|---|---|---|
| Conventional | 0.031 | 1.86 | 0.002 | 0.022 | 0.38 | 16.76 | 9.90 | 2.11 | Bal. |
| AM | 0.027 | 0.53 | 0.017 | <0.001 | 0.424 | 16.67 | 13.45 | 2.26 | Bal. |

### 6.2.4 Microstructures and defects

After removal from the substrate, samples of small dimensions were cut (disc saw cut) from the cylindrical specimens, for metallographic analysis in the as-built state. All samples were prepared with the same type of resin and the same hot assembly technique being submitted to the same polishing sequence. These samples' inspection was conducted by optical microscopy on an Olympus PMG3 microscope as well as on a ZEISS Axiophot optical microscope, and by electronic microscopy using a high resolution scanning electron microscope with X-Ray microanalysis and electron backscattered diffraction analysis: Quanta 400 FEG ESEM / EDAX Genesis X4M.

#### 6.2.4.1 Porosity

To evaluate the porosity of the material taking into account its orientation, a cylindrical specimen in the as-built state was sectioned in three different samples, each of which had both end surfaces polished. Figure 6.4 shows the schematics of this division, where the inscriptions refer to each of the surfaces analyzed.

A collection of photographs of each of the polished surfaces was obtained by optical microscopy; three photographs with magnification 50x of different areas for each surface, and subsequent image analysis through the ImageJ software was performed, the percentage of porosity was calculated, as the average value of the three areas.

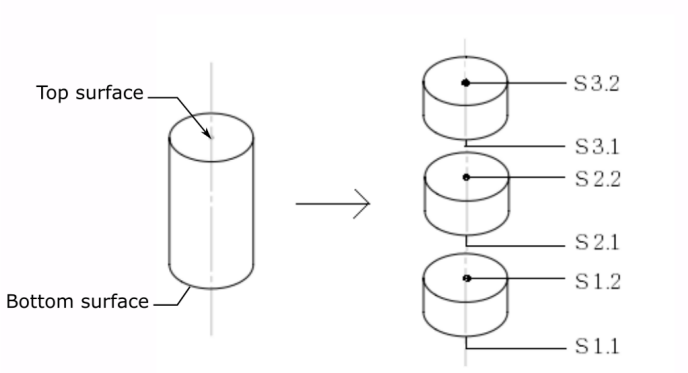


Figure 6.4: Schematics of the division of the cylindrical specimen.

Porosity measurements are obtained through the transformation of microscopic images of the surface into binary color maps (see Figure 6.5), concluding with the calculation of the area ratios.

These results show high porosity levels, with peaks closer to 5%, which correlate with results from Suryawanshi et al [66], where the measured porosity levels through image analysis reached

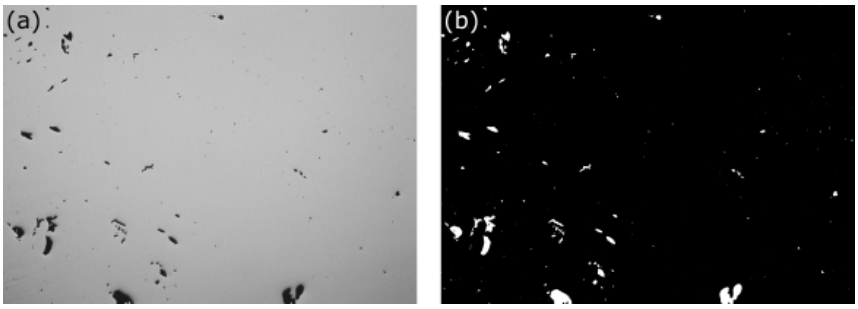


Figure 6.5: Example of the image analysis process of S1.1 surface (polished surface): (a) optical microscopy image of the polished surface and (b) image after processing.

Table 6.2: Porosity results with respect to the surfaces considered.

| Surface | S1.1 | S1.2 | S2.1 | S2.2 | S3.1 | S3.2 |
|---|---|---|---|---|---|---|
| % Porosity | 0.79 | 4.74 | 2.17 | 3.73 | 3.42 | 2.71 |

4.8%. It is, however, possible to achieve less porous SS316L parts through SLM processing [60, 62], with relative densities higher than 99%, through fine tuning of the SLM parameters.

There is no identifiable pattern in the porosity results with respect to the relative position of the surfaces in the cylinder, except for the low values (less than 1%) observed for the bottom surface, S1.1. Of the surfaces analyzed this is the nearest to the substrate, hence the low porosity can relate to the fact that this was one of the first layers to be constructed, thus avoiding some issues that arise from a defective overlap of layers, as explored in Section 2.4.2.

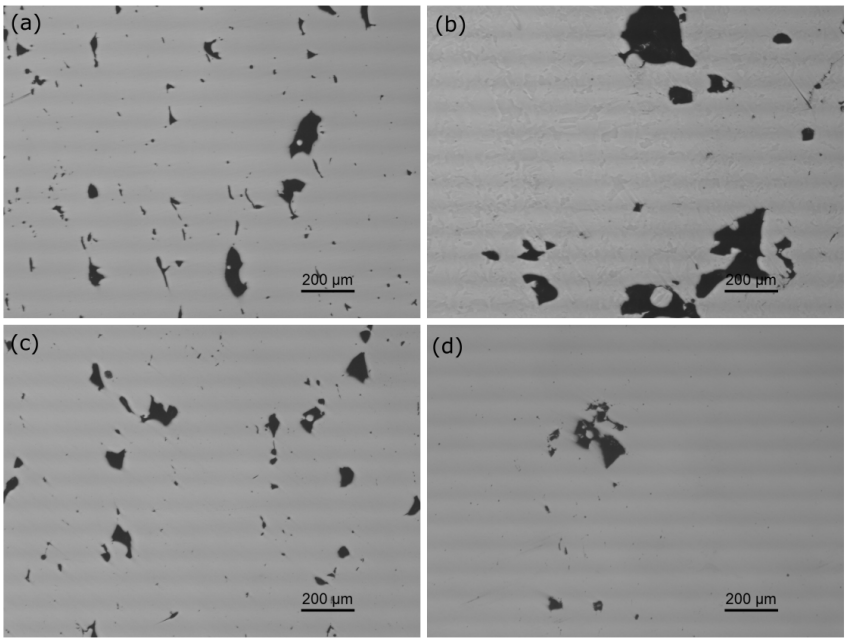


Figure 6.6: Optical micrographs showing pores in different regions of a section parallel to the building direction (XZ or YZ) (a) and (c), and on a section transverse to the building direction (XY) (b) and (d).

Figure 6.6 shows optical micrographs of different regions, both in the build plane (XZ or YZ) and in the scan plane (XY), for better understanding the levels of porosity obtained through image analysis.

#### 6.2.4.2 Microstructure

The samples for the microstructure analysis were etched with a Super Picral solution (20g picric acid + 100 HCL) for approximately 1 minute. In addition, an electrolytic etching with oxalic acid (10g oxalic acid + 90g distilled water) with 6V DC for 50 seconds was conducted on the samples to reveal other metallurgical characteristics. Figures 6.7 to 6.10 show the typical microstructures revealed by chemical and eletrolytic etching. It is possible to observe the continuity in grain growth through melt pools, the solidification structure, the overlap of melt pools along the layers and along the building direction. Note that the microstructures revealed by chemical etching emphasize the grain morphology, whereas electrolytical etching highlights the macrostructure of the melt pools and tracks.

The microstructures in Figure 6.7 (a) and (b) are coherent with those presented in literature [67–69], showing a cross section of the molten pools with a curved structure. Considering that the heat flux is higher in a direction perpendicular to the solid/liquid interface, the grain growth follows this preferential orientation, presenting cellular-columnar grains that grow through subsequent layers of melted powder, inheriting the orientation of the grains formed in the previous layer, displaying epitaxial growth characteristics [29, 70]. This translates into an anisotropy of mechanical properties for the SLM produced parts, as verified by results found in literature (Table 5.2) as well as the experimental compression results that will be further analysed. Figure 6.7 (f) shows the microstructure of the conventional material, characteristic of the solution annealed condition [67, 71, 72], exhibiting a certain amount of annealing twins and an absence of grain boundary precipitates. Figure 6.7 (c) and (d) show different microstructural defects: microcracks across crystallised grains and voids located between subsequent melt layers, respectively. The latter can be associated with poor wetting of the melt pool on the previously deposited layer, arising from the presence of superficial oxides as suggested in previous studies [67]. The presence of voids with an irregular shape and different sizes between scan tracks shown in Figure 6.7 (e), appears to be related with insufficient overlap between laser scan tracks or even due to a low laser power [73], leading to incomplete consolidation, as explored in Section 2.4.2.

Further microstructural defects typical of SLM technology can be observed in the micrographs shown in Figure 6.8. The presence of small spherical porosity, preferentially located between molten pools, Fig. 6.8 (a), that appears to be related to gas entrapment during layer building, and cracks across a crystallized grain, Fig. 6.8 (b) as well as irregular shaped voids between molten pools. Furthermore, Figure 6.8 (c) and (d) show the dendritic microstructure of non fully-melted powder particles between the well-developed cellular grain microstructure of fully melted particles. These slowly solidified powder particles show a preferential dendritic microstructure due to higher overcooling rates, as concluded in [67]. These unmelted particles are usually associated with lack of fusion voids, as shown in Figure 6.9(b). Figure 6.9(a) shows another lack of fusion

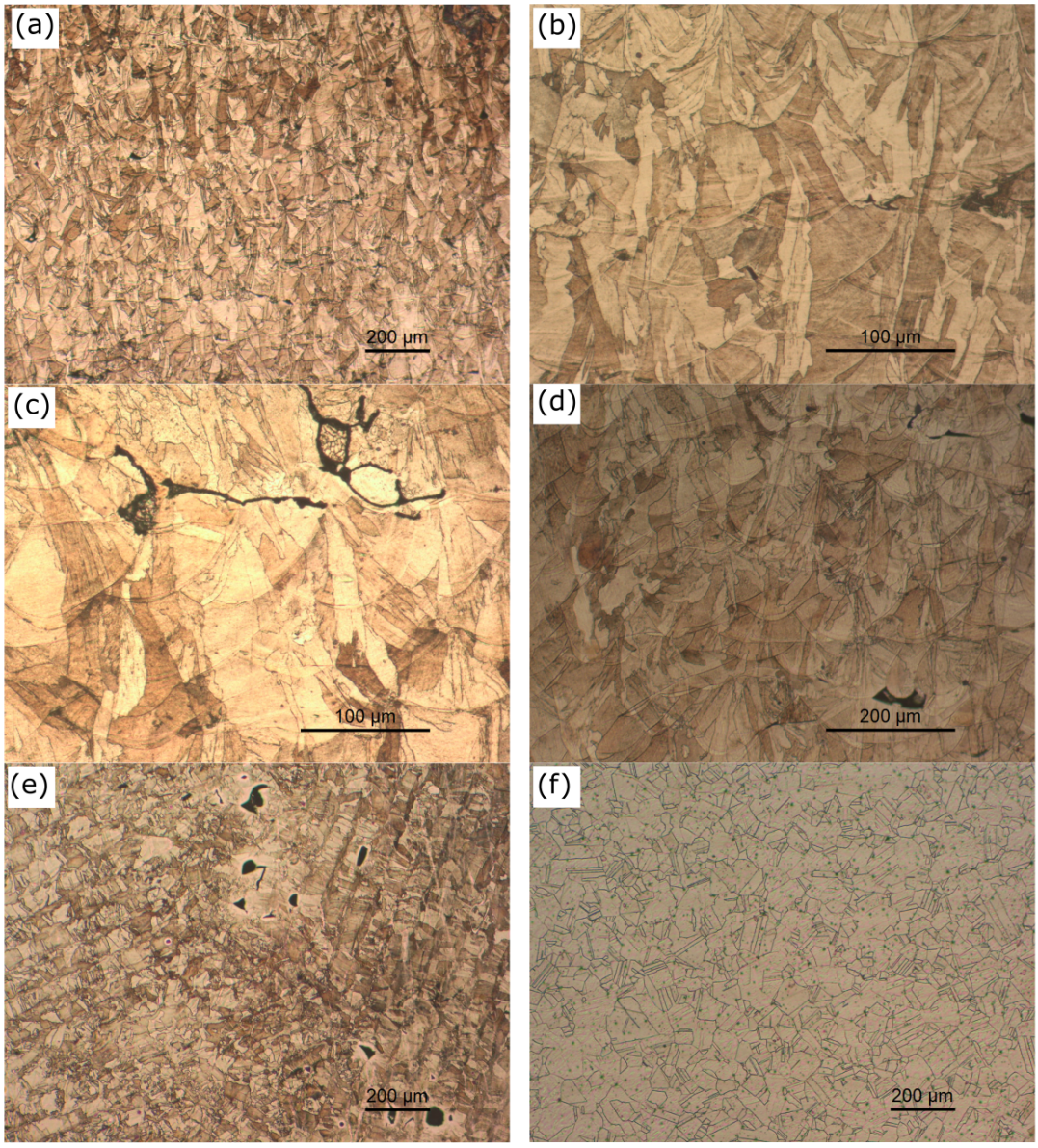


Figure 6.7: Optical microscopy images of the microstructure (chemically etched) on a section parallel to the building direction: (a) macrostructure of the melt pools showing the columnar crystal growth; (b) detail of the melt pools and grain structure; (c) detail of a crack in the microstructure; (d) pore resulting from lack of fusion between melt pools of subsequent layers. (e) Laser scans on a section transverse to the building direction. (f) Equiaxial crystals of the conventional material (characteristic of the annealed condition).

void between melt pools and, in the surroundings, it is possible to observe the internal structure of the columnar grains; each grain consists of a colony of cells with parallel growth direction, the difference in orientation between these colonies arises from the different cooling rates within the melt pool, consistent with what was found in literature [69, 74].

From Figure 6.10 (a) and (b) a hatch spacing of approximately 75 $\mu$m was calculated as the

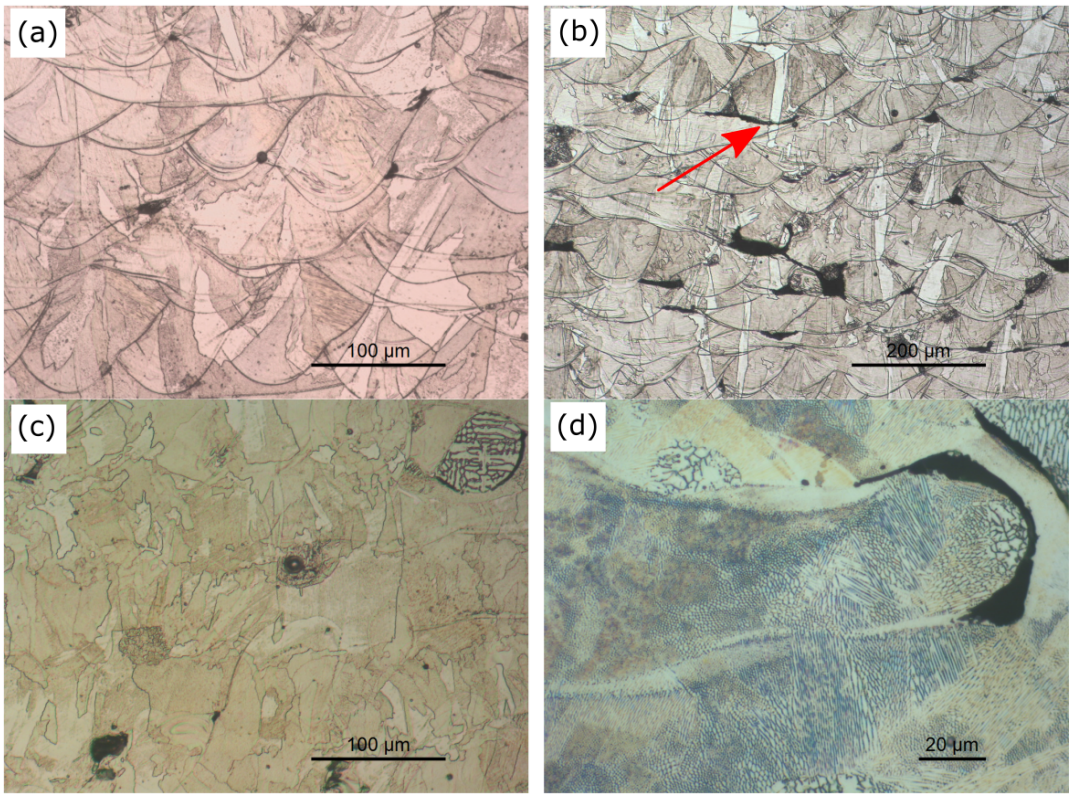


Figure 6.8: Optical microscopy images of the microstructure (electrolytically etched) on a section parallel to the building direction showing: (a) voids between molten pools and (b) cracks across solidified columnar grains. Micrographs of a section transverse to the building direction showing non fully-melted powder particles (c) and (d).

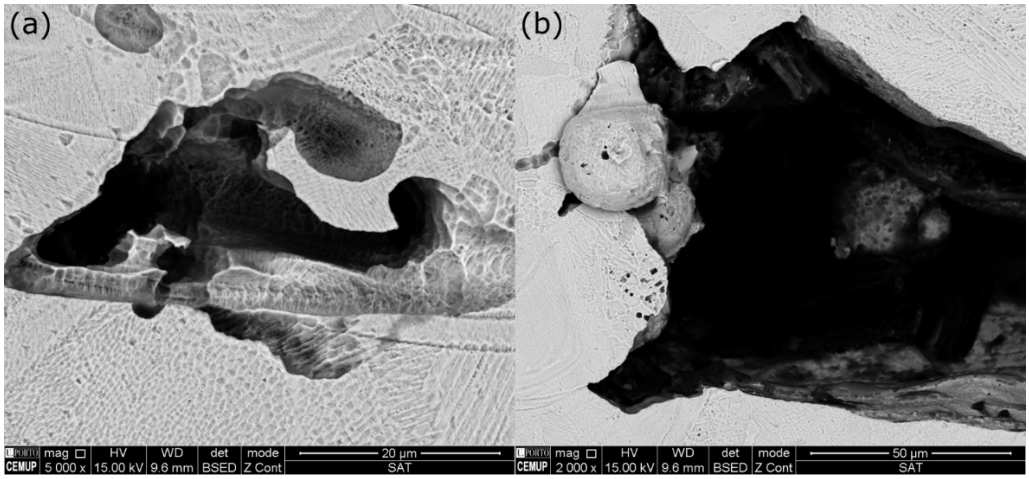


Figure 6.9: Backscattered SEM images of the microstructure on a section longitudinal to the building direction showing cellular substructure and lack of fusion porosity (a) with unmelted powder particles (b).

average of the measured distances shown, and in a similar approach the distance between molten pools was also measured, Fig. 6.10 (a). Figure 6.10 (d) shows the overlap between scan tracks

of successive layers, from where an average rotation angle between layers, of approximately 60 ° was measured.

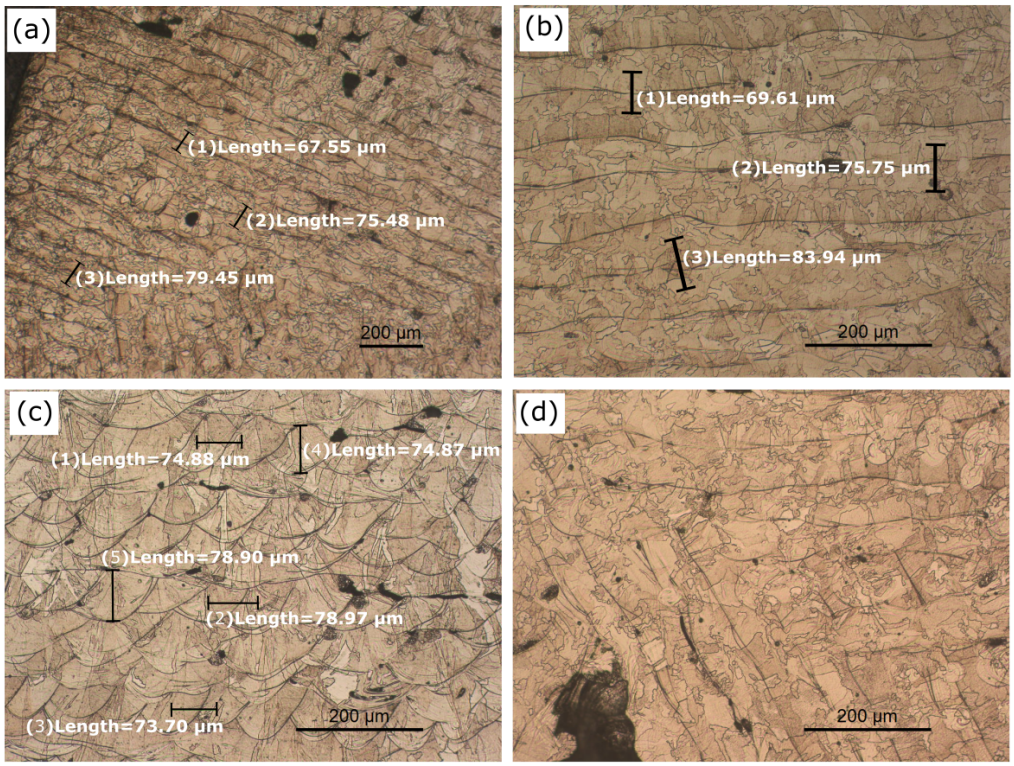


Figure 6.10: Optical microscopy images of the microstructure (electrolytically etched) on a section: transverse to the building direction: (a) and (b) measured distance between scan tracks, (d) scan rotation angle between successive layers; parallel to the building direction showing the measured distances between molten pools (c).

### 6.2.5 Roughness measurements

To evaluate the surface roughness of the samples in the as-built state, measurements were conducted in CETRIB-Tribology, Vibrations and Industrial Maintenance Unity (INEGI) in accordance with the DIN 4768 standard. For this purpose a HommelWorke rugosimeter, with a TKL300 probe was used (Figure 6.11(a)).

Measurements for the as-built state were carried out on a turning specimen - *T4* (Fig. 6.11(a)) and an orthogonal cutting specimen - *O5* (Figure 6.11(b)). For the top surface of each specimen and for each of the directions (longitudinal-$L$ and transverse-$T$) three measurements were taken, and three more on the lateral surface, in the building direction-$B$. Figure 6.12 (a) and (b) shows the roughness profiles obtained for the longitudinal direction, $L$, of the specimen T4 and for the building direction, $B$, of the specimen O5, respectively. Table 6.3 summarizes the average values of roughness for each of the directions considered for each specimen.

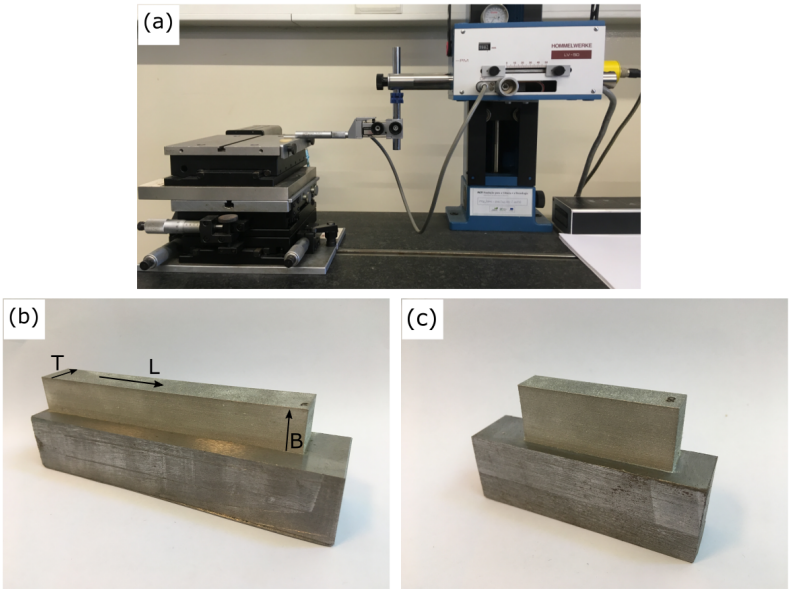


Figure 6.11: (a) HommelWorke rugosimeter. Directions for the roughness measurements and specimens analyzed: (b) turning specimen and (c) orthogonal cutting specimen.

Table 6.3: Average roughness values in $\mu$m for the as-built state.

| Specimen | Direction | Ra | Rz | Rmax |
|---|---|---|---|---|
| T4 | L | 11.06 | 55.64 | 73.52 |
| | T | 10.50 | 54.65 | 71.17 |
| | B | 8.99 | 49.68 | 63.54 |
| O5 | L | 11.11 | 53.97 | 75.73 |
| | T | 8.81 | 48.12 | 66.78 |
| | B | 10.79 | 57.72 | 72.59 |

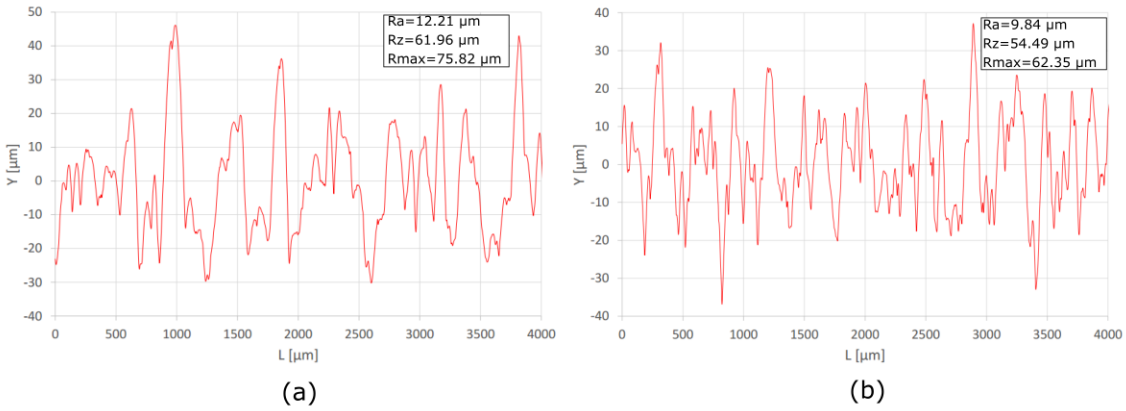


Figure 6.12: Roughness profiles of the second measurement: (a) specimen T4 in the longitudinal direction L; (b) specimen O5 in the building direction B.

Figure 6.13 shows a SEM image of the as-built surface, on a section parallel to the building direction, revealing a great amount of non fully melted powder particles, which correlates with the

surface roughness results. This emphasizes the importance of post-machining operations on SLM fabricated components.

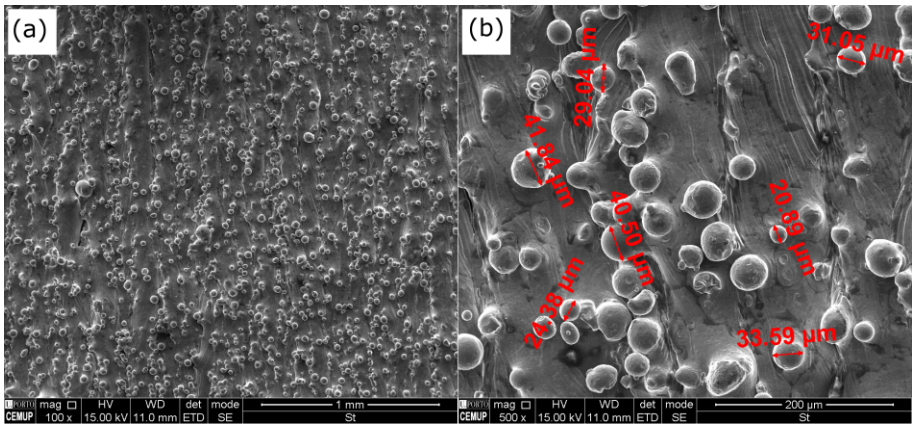


Figure 6.13: SEM image of the as-built surface on a section longitudinal to the building direction.

### 6.2.6 Compression tests

Quasi-static compression tests were performed for the AM and conventional specimens, in order to characterize the material flow stress. For this, the AM compression specimens (Figure 6.2), two of each both vertical and horizontal, and three conventional-material specimens were pre-machined into $\phi$6x6 mm cylinders (Figure 6.14) by means of a lathe. The test specimens were then placed in the testing machine between two tungsten carbide plates (Figure 6.15(a)).

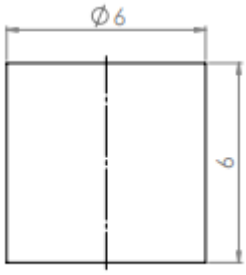


Figure 6.14: Compression test specimen drawing.

The compression tests were conducted at a quasi-static speed of 1mm/min, and the stopping criteria was set for a maximum displacement of 4mm or a maximum load of 90 kN. All experiments stopped for the maximum set load, and all tested specimens showed ductile behavior, displaying round lateral edges (barreling), Figure 6.15(c).

Figure 6.16 shows the true stress-strain curves obtained for the compression specimens, up to 0.8 strain value. It is worth mentioning that strain was computed from the machine actuator displacement but machine stiffness correction was performed.

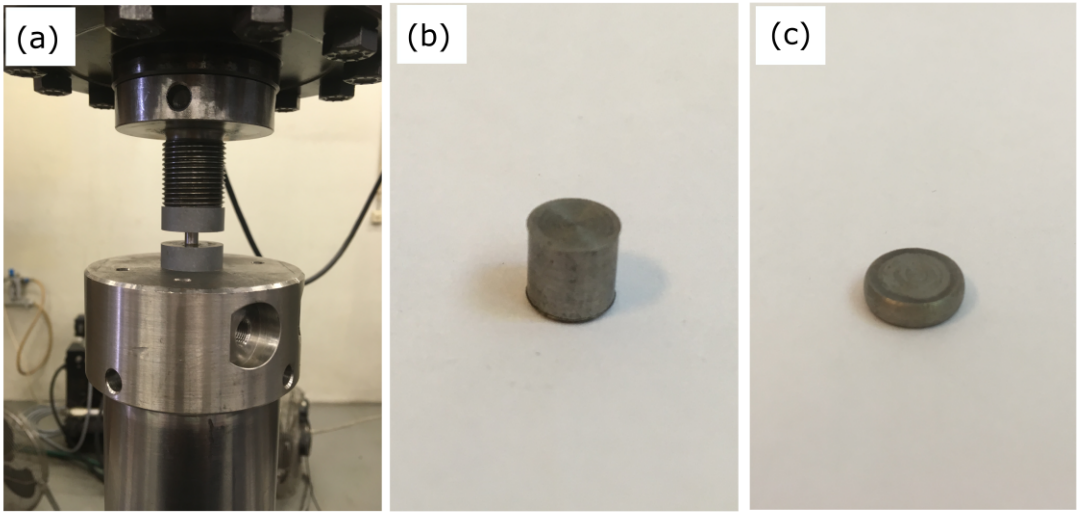


Figure 6.15: (a) Compression test specimen mounted on the compression system; (b) Test specimen before compression; (c) Test specimen after test.

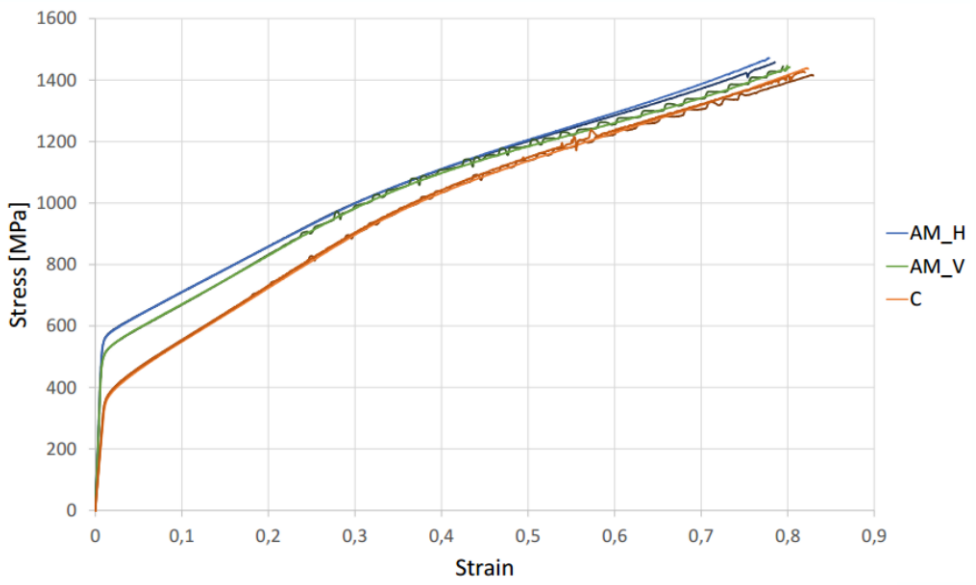


Figure 6.16: Stress-strain curves for the vertical (V) and horizontal (H) AM specimens and for the conventional (C) specimens.

The flow stress curves present good repeatability and it is possible to observe that the AM specimens have a higher yield strength (approximately 556 MPa for the horizontal, X-Y direction, and 504MPa for the vertical, Z direction, specimen) compared to the conventional ones (approximatelly 352MPa). Particularly, the horizontally built AM specimens exhibit 58% higher yield strength than the conventional ones, and 10% higher yield strength than the vertically built AM specimens, which is coherent with what was found in literature [75, 76].

## 6.3 Machining

### 6.3.1 Pre-machining of the samples

The turning specimens, both AM (Figure 6.2) and conventional had to be pre-machined into cylinders with $\phi$15x120 mm (Figure 6.17), prior to the turning tests. The latter were obtained by turning a $\phi$20 mm rod to the final dimensions. These specimens were machined with a centering hole in order to provide greater stability for the turning operation by using a counterpoint.

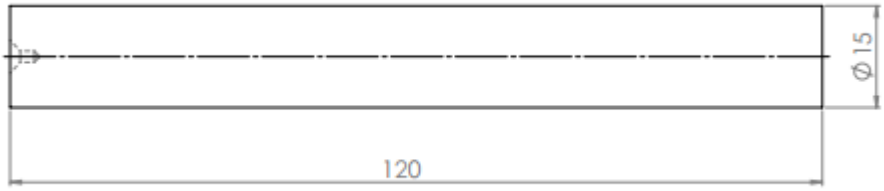


Figure 6.17: Turning test specimen drawing.

### 6.3.2 Cutting tools

Two cutting inserts with the same rhombic shape of 55º and distinct rake face geometries (flat and chip-break) were considered for the conducted experimental tests. It is important to note that finishing operations are the focus of this experimental campaign, being the chip breaking tool (DCGT 11T304-FS) fully suitable for the operation and the one with a flat rake face (DCMW 11T304) serving as control for performance comparison (cutting forces, chip morphology and surface quality).

These tools were chosen for fine cutting conditions (Section 6.3.4); with maximum depth of cut and feed rate of 0.5mm and 0.2 mm/rev, respectively. The small diameter of the turning specimens ($\phi$15 mm) limits the maximum depth of cut possible, since the intent is to efficiently utilize the material for various tests. Another imposed restriction is the limited cutting speeds attainable, owing to the specimens diameter and the maximum rotation frequency of the machine, 2500 rpm.

Table 6.4 presents the tools' geometries, which were selected (and gently provided) according to the expertise and experience of Palbit S.A.. Their dimensions, with respect to the nomenclature is shown in Figure 6.18. They are defined as positive turning inserts, since they have a relief angle of 7°, recommended for external turning of slender components, as are the turning specimens to be tested (Figure 6.17) and for low cutting forces that are expected in the experiments, since they are related to finishing and fine finishing operations.

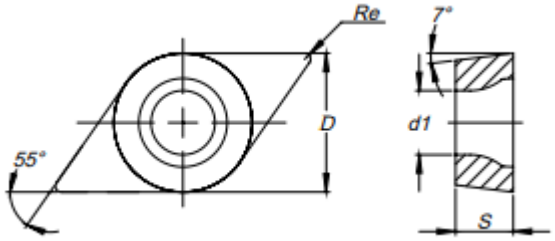


Figure 6.18: Geometric parameters of the inserts.

Table 6.4: Inserts designation and dimensions in accordance with Palbit® turning catalogue.

| Code | ISO reference | ANSI reference | Dimensions [mm] | | | |
|---|---|---|---|---|---|---|
| | | | D | S | $R_\varepsilon$ | d1 |
| T1<br>T2 | DCGT 11T304-FS<br>DCMW 11T304 | DCGT 32.51-FS<br>DCMW 32.51 | 9.525 | 3.97 | 0.40 | 4.40 |

#### 6.3.2.1 Toolholder

The toolholder was selected based on the geometry of the inserts, the dimensions of the experimental setup components (Section 6.3.3) and the direction of cut. This component, with the designation SDJC L 2020 K11, has a center screw system for holding the insert. Figure 6.19 shows its main geometrical parameters, including a side cutting edge angle of 93°; and its dimensions are indicated in Table 6.5.

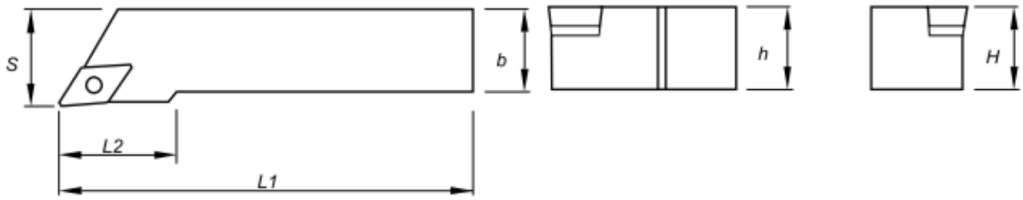


Figure 6.19: Toolholder geometrical features.

Table 6.5: Toolholder designation and dimensions in accordance with Palbit® turning catalogue.

| Reference | Dimensions [mm] | | | | |
|---|---|---|---|---|---|
| | H=h | b | L1 | L2 | S |
| SDJC L 2020 K11 | 20 | 20 | 125 | 22 | 25 |

#### 6.3.2.2 Cutting tool materials

Both inserts have cemented carbide substrates, but differ in the coating materials and method of fabrication. The insert with chip breaker has a titanium aluminum nitride (TiAlN) PVD coating, while the other has an alumina ($Al_2O_3$), Titanium CarboNitride (Ti(C,N)) CVD coating. The material grades for both inserts are indicated in Table 6.6, as well as their designation and description.

Table 6.6: Inserts' material grades in accordance with Palbit® turning catalogue.

| Code | ISO reference | Coating grade | Description |
|---|---|---|---|
| T1 | DCGT 11T304-FS | PH7920 | Micrograin carbide substrate grade with TiAlN PVD coating. Suitable for roughing to finishing operations under good cutting conditions to light interrupted cuts at medium cutting speeds. Recommended for turning of steels and stainless steels. |
| T2 | DCMW 11T304 | PH5705 | Carbide grade with $Al_2O_3$ and Ti(C,N) CVD coating, suitable for machining at high to medium cutting speeds under stable conditions. Recommended for turning of grey cast irons and hardened steels, and also a solution for high alloy steels. |

Regarding the low time periods of the machining experiments, significant wear on the inserts is not expected, thus allowing for the evaluation of the cutting conditions influence on the forces, type of chip formation and surface quality without the influence of the insert wear factor.

#### 6.3.2.3 Chip breaker geometry

The function of a chip breaker is to improve chip control and to reduce the cutting resistance; by adopting this feature the chips can be broken into smaller lengths, preventing their winding around the workpiece, thus decreasing vibration and damage of the insert and workpiece.

As mentioned above, the DCMW insert has a flat face without a chip breaker as shown in Figure 6.20(a), while the DCGT-FS insert, Figure 6.20(b), has a chip breaker suitable for finishing operations, with a small breaker width and a positive land, which increases its sharpness. These chip breakers are designed to decrease the chip curl radius so that they are easily broken, and owing to the low loads on the cutting edge during finishing operations, its sharpness is prioritized instead of strength.

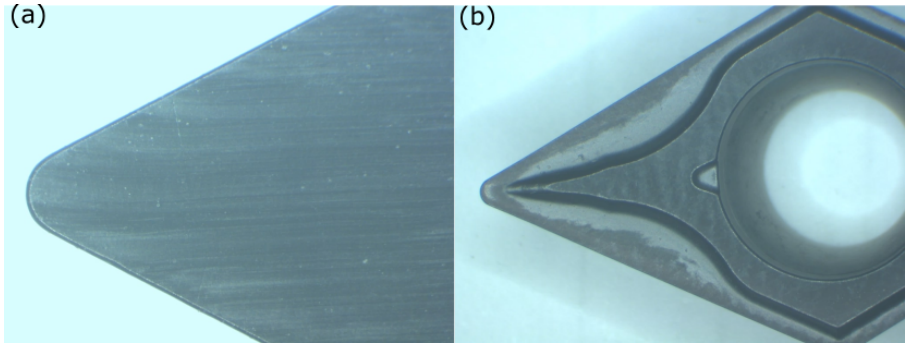


Figure 6.20: Palbit inserts: (a)DCMW 11T304, (b) DCGT 11T304-FS.

### 6.3.3 Experimental apparatus

Figure 6.21 shows the experimental setup schematics used for the turning operations. Each of the components involved in the experimental tests are explored ahead, from the machine-tool to the force measuring system.

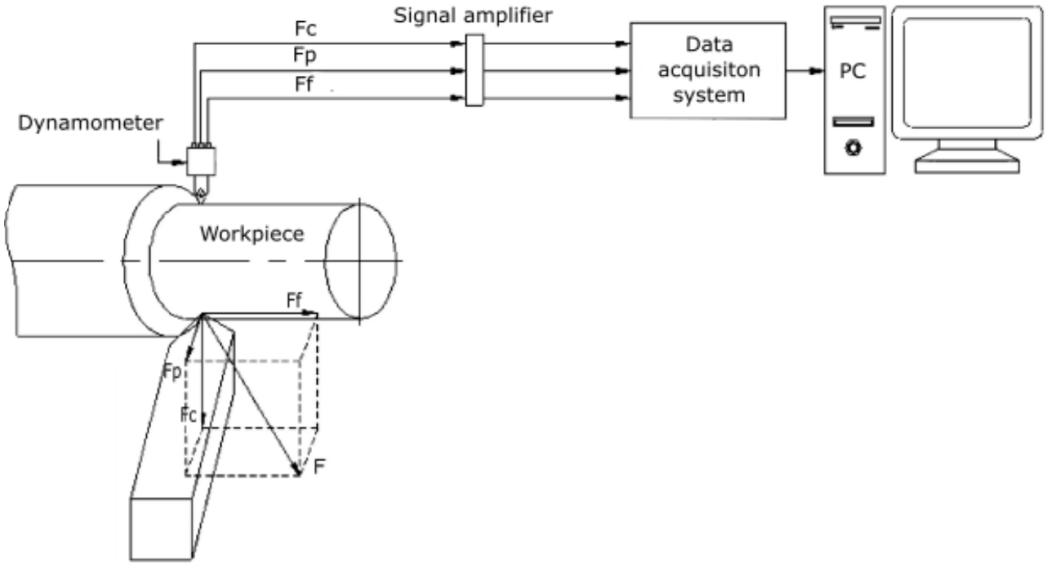


Figure 6.21: Schematics of the experimental setup. Adapted from [77].

The turning experiments were conducted in a conventional lathe EFI DU20 (DEMec), Figure 6.22, with 5.9 kW power and a stepped variation of rotation frequency with a maximum of 2500 rpm. The tests were performed with adequate instrumentation to measure the cutting force components ($F_f$, $F_p$ and $F_c$); specifically a piezoelectric dynamometer equipped with a signal amplifier and a data acquisition system. For this purpose a KISTLER 9257B piezoeletric dynamometer was used. It was equipped with a fastening system responsible for the correct attachment of the cutting tool as indicated by the manufacturer, Figure 6.23 (a). The cell's correct positioning was ensured so that the tool was aligned with the center of rotation of the clamping bush, as shown in Figure 6.23 (b).

Furthermore, a KISTLER 5070 multichannel charge amplifier, Fig. 6.24 (a), was responsible for converting the electrical signals (pC) from the dynamometer into the equivalent tension signals (V). It was necessary to make adjustments to the parameters in this signal amplifier, namely in scales, time constant and channels sensitivity to match the characteristics of the dynamometer and the type of test to be performed. The ADVANTECH portable data acquisition system, Fig. 6.24 (b), in combination with the computer software, enables the acquisition of data from the signal amplifier, that in turn allows for the subsequent data analysis of the cutting force components as function of the machining time.

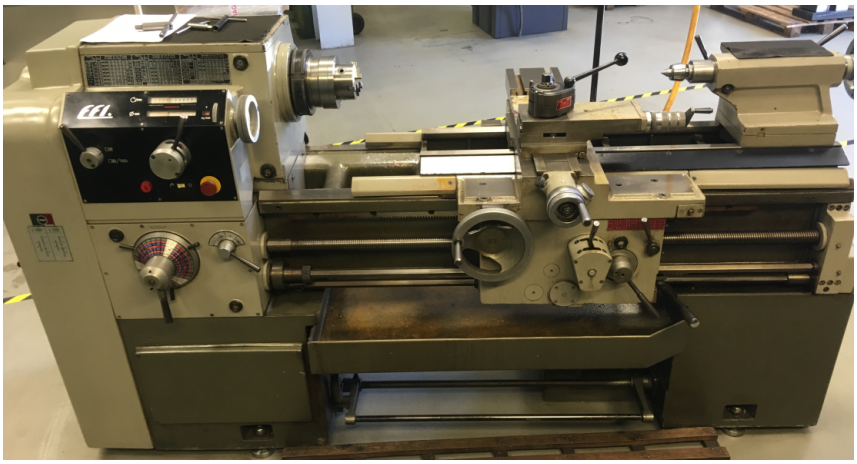

Figure 6.22: EFI DU20 conventional lathe.

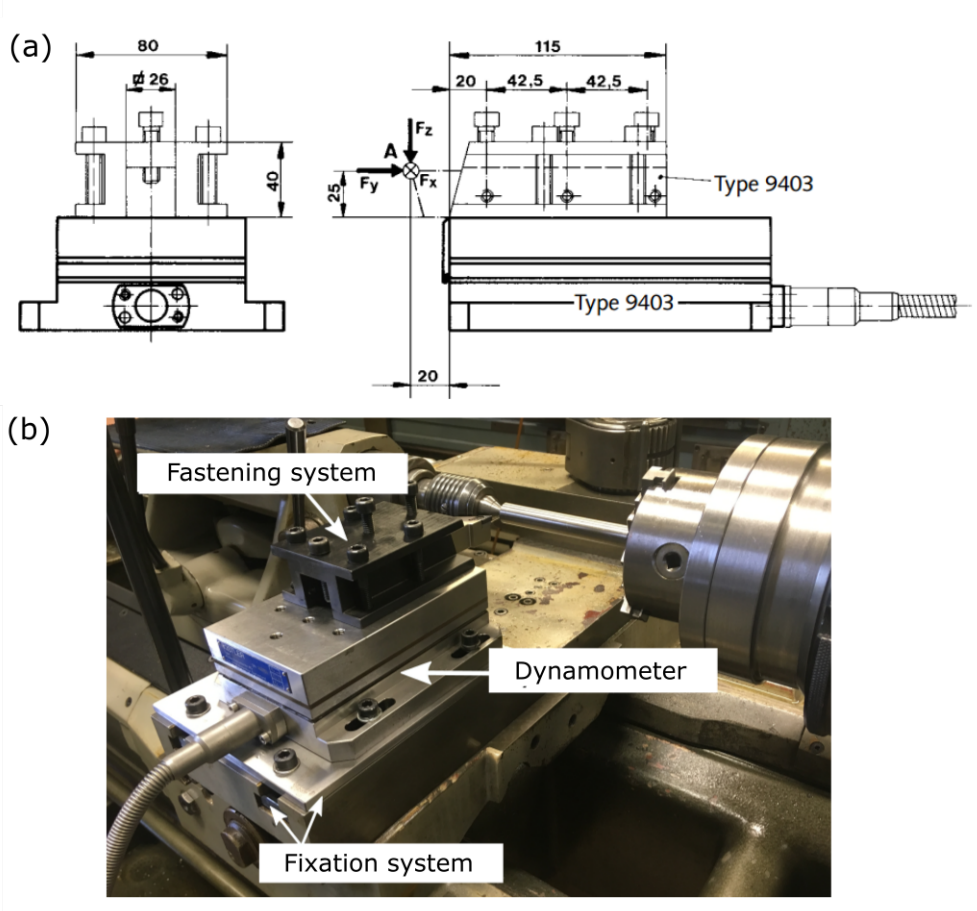


Figure 6.23: (a) Dynamometer type 9257B with mounted fastening system type 9403. Adapted from KISTLER multicomponent dynamometer data sheet 9257B 000-151e-07.18. (b) Detail of the dynamometer, fastening system and fixation system assembly.

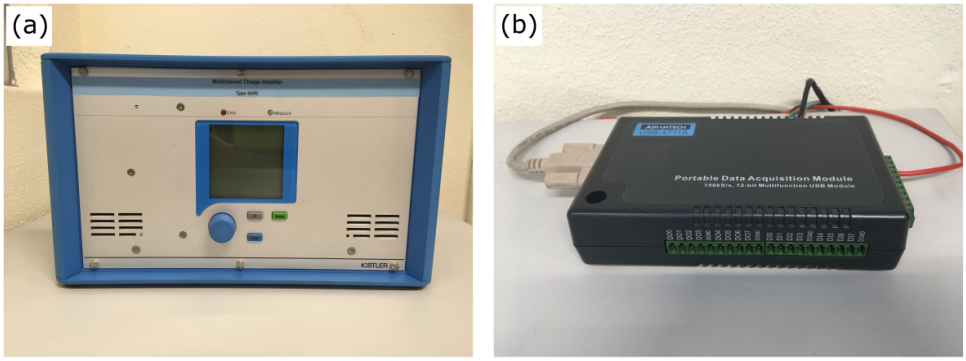


Figure 6.24: (a) KISTLER multichannel charge amplifier. (b) ADVANTECH portable data acquisition system.

### 6.3.4 Turning parameters

The turning experiments had the purpose of evaluating the machinability (focusing on finishing operations) of the AM AISI316L in terms of cutting forces, chip formation and resulting surface quality, and comparing the results with those of the conventional material.

The choice of parameters was restricted by both the machine-tool and the dimensions of the test specimens. This choice is also supported by the type of cutting operations that metallic AM components are usually submitted to. Two rotation frequencies were selected, 2500 rpm (the maximum allowed by the machine) and 1800 rpm and three depths of cut, 0.1, 0.3 and 0.5 mm for feed rates of 0.05, 0.1 and 0.2 mm/rev.

The turning sequence, conducted for each cutting tool is shown in Table 6.7; in Appendix B an extended table with the cutting conditions and respective operation coding can be consulted. Each specimen was divided into four zones with the same length, two of which were machined with the same type of tool, one with the rotation frequency of 2500 rpm and the other with 1800 rpm, for all the combinations of depths of cut and feeds (Figure 6.25). A total of four specimens were machined, two of the AM material and two more of the conventional one. For each specimen a new insert was used, each having completed a total of 18 cuts, corresponding to the sequence shown in Table 6.7. A final diameter of approximately $\phi$9.6 mm was achieved for each section of the turning specimens.

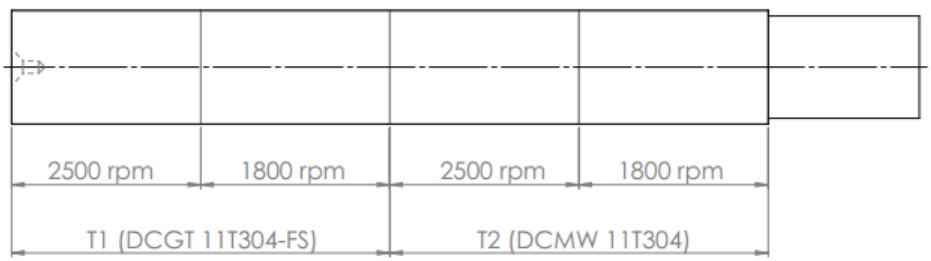


Figure 6.25: Schematics of the specimen sections for the turning experiments.

Table 6.7: Cutting conditions for the experiments conducted in the conventional lathe.

| n [rpm] | $f$[mm/rev] | $a_p$ [mm] | Diameter [mm] | $v_c$ [m/min] |
|---|---|---|---|---|
| 2500 | 0.2 | 0.5 | 15 | 118 |
| | 0.2 | 0.3 | 14 | 110 |
| | 0.2 | 0.1 | 13.4 | 105 |
| | 0.1 | 0.5 | 13.2 | 104 |
| | 0.1 | 0.3 | 12.2 | 96 |
| | 0.1 | 0.1 | 11.6 | 91 |
| | 0.05 | 0.5 | 11.4 | 90 |
| | 0.05 | 0.3 | 10.4 | 82 |
| | 0.05 | 0.1 | 9.8 | 77 |
| 1800 | 0.2 | 0.5 | 15 | 85 |
| | 0.2 | 0.3 | 14 | 79 |
| | 0.2 | 0.1 | 13.4 | 76 |
| | 0.1 | 0.5 | 13.2 | 75 |
| | 0.1 | 0.3 | 12.2 | 69 |
| | 0.1 | 0.1 | 11.6 | 66 |
| | 0.05 | 0.5 | 11.4 | 64 |
| | 0.05 | 0.3 | 10.4 | 59 |
| | 0.05 | 0.1 | 9.8 | 55 |

All the experiments were conducted in dry turning conditions, although as discussed in Section 5.1.2 this is not ideal, it was necessary due to the setup utilized for the dynamometer and to avoid the introduction of further variables in the tests.

Figure 6.26 shows the workpiece mounted on the clamping bush and counterpoint of the conventional lathe, with four distinct cutting zones marked.

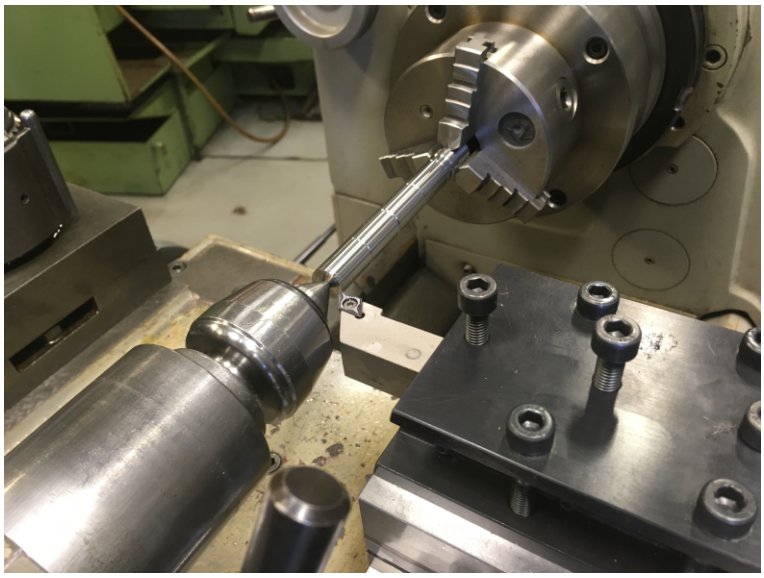

Figure 6.26: Detail of the workpiece assembly on the conventional lathe.

### 6.3.5 Surface analysis

Besides chip analysis, the surface quality was also measured in terms of surface roughness, as a way to compare the results obtained from machining with a chip breaker and without.

For this the last turning operation, that it is not contemplated in Table 6.7, was conducted in each of the two, additively and conventionally manufactured, test specimens with a different tool and with the same cutting conditions; depth of cut of 0.3 mm, three feed rates; 0.2, 0.1, 0.05 mm/rev, one for each section (Fig. 6.27) and a rotation frequency of 1800 rpm (Table 6.8). For these turning operations new inserts were used, each completing a total of three cuts, in order to study the influence of such operations on both the surface finish of the inserts and the test specimens as isolated factors from the previous cuts.

In this way it was possible to evaluate the influence of the feed rate and chip breaker on the surface roughness. For these measurements a Bruker optical profilometer with Vision64 software was used.

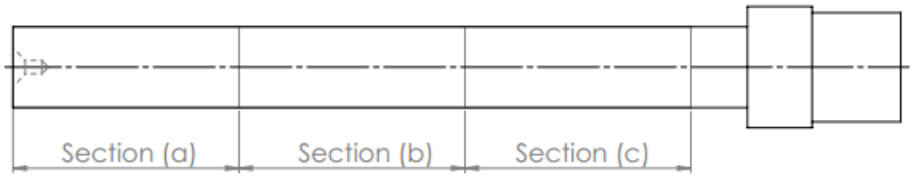


Figure 6.27: Schematics of the sections machined with different feeds for roughness measurements.

Table 6.8: Cutting conditions for surface analysis.

| Tool | $n$ [rpm] | $a_p$ [mm] | $f$[mm/rev] | Section |
|---|---|---|---|---|
| T1: DCGT 11T304-FS | 1800 | 0.3 | 0.2 | (a) |
| | | | 0.1 | (b) |
| | | | 0.05 | (c) |
| T2: DCMW 11T304 | 1800 | 0.3 | 0.2 | (a) |
| | | | 0.1 | (b) |
| | | | 0.05 | (c) |

# Chapter 7

# Experimental results and discussion

## 7.1 Machining power and cutting forces

Monitoring the forces involved in the turning experiments enabled the machinability assessment of both AM and conventional 316L. Furthermore, these studies provide a means for comparison between these two materials and also their response to the cutting conditions and tools tested.

A total of 144 external turning operations were performed, and for each, the output force spectrum was similar to the one presented in Figure 7.1. This graphic shows the three force components involved in turning ($F_f$, $F_p$ and $F_c$). Four regions can be identified in this graphic; the first, where no forces are recorded, corresponds to the lathe turned off, the second shows force fluctuation resulting from turning on the lathe spindle, the third is the actual turning/cutting forces measurement, and the last corresponds to the return of the cutting tool. The results presented in the succeeding sections only take into account a stable region of the third zone of measurements.

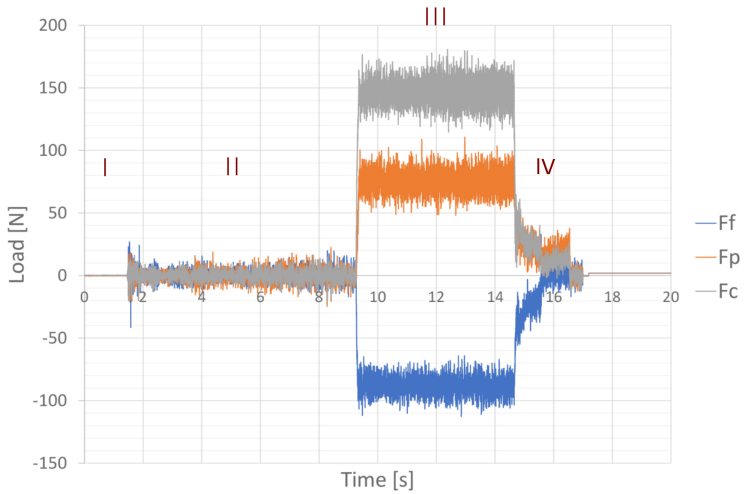


Figure 7.1: Load spectrum of the AM 316L turning operation with cutting tool T1, $n$=2500 rpm, $v_c$=104m/min, $f$=0.10 mm/rev and $a_p$=0.5 mm.

Due to the great amount of data originated from these experiments, presenting all graphics of the evolution of the forces with time proved to be impractical. Therefore, in the succeeding sections, an analysis of the average values of all force components over time, for the stable measurement region, is presented. A table with the average load values can be consulted in Appendix C. The error bars that appear in the graphics represent the standard deviation of the forces measured in relation to their average value, taking into account the fluctuations experienced during these measurements. First an analysis of the feed and penetration forces is preformed for the maximum rotation frequency, with relation to their variation with feed and depth of cut, respectively. Follows the analysis of the main cutting force for all cutting conditions tested, being that this force is the highest involved in the process, and accounts for 99% of the power required for turning [49]. Ending this analysis, is the evolution of the cutting pressure with the area of the chip section, for all conditions tested.

### 7.1.1 Evolution of the feed and penetration forces

The graphics presented in Figures 7.2 and 7.3 show the evolution of feed forces and penetration forces as a function of feed rate and depth of cut, respectively, for a rotation frequency of 2500 rpm. The fact that the cutting speeds did not remain constant throughout the variation of cutting conditions may have an influence on these results, although it is not expected to have a great effect on the comparative analysis between materials, and between cutting tools.

From these graphics (Fig. 7.2 and 7.3), it is noticeable that for all cutting conditions presented, cutting tool T2, the one without chip breaker, results in the highest feed and penetration forces for both materials. As for the differences between forces of the AM and conventional materials, there is not a well defined tendency relating to the cutting conditions. Moreover, the average penetration and feed forces obtained for the AM material machined with cutting tool T1 are in agreement with the values found in literature [78] for similar turning conditions.

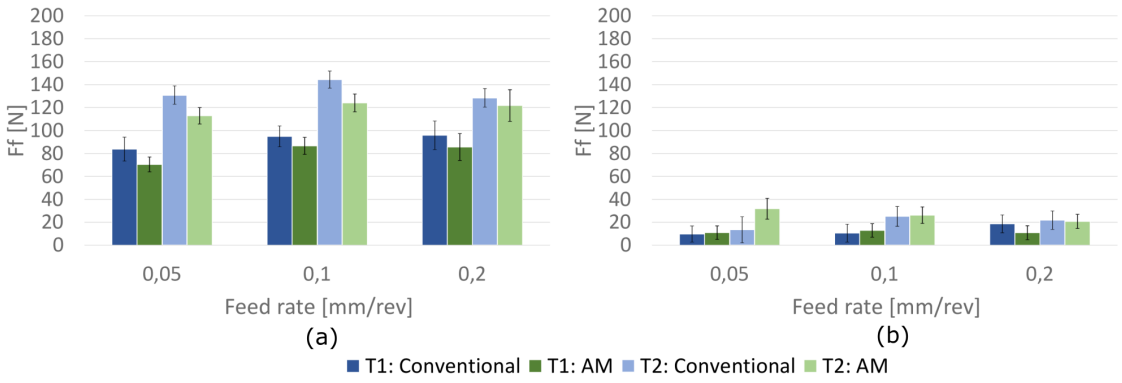


Figure 7.2: Evolution of the feed force as a function of feed rate for the AM and conventional specimens: (a) $n$=2500 rpm and $a_p$=0.5mm; (b) $n$=2500 rpm and $a_p$=0.1mm

Figure 7.2 shows a high dependency of the feed force on the depth of cut, for all feed rates tested, as was expected [49]; from a depth of cut of 0.5mm (a) to 0.1mm (b), the feed force,

of the cutting tool T1, for the conventional 316L showed a decrease of 85%, correspondent to approximately 74N, and of 84% for the AM 316L, correspondent to approximately 59N. Whereas the dependency upon feed rate is not so noticeable, with the values of feed force fluctuating with increased feed rate, for both materials and tools.

The graphics in Figure 7.3, show that the penetration force is not as dependent on feed rate as the contrary. Existing, however, a decrease of this force with decreasing feed rate; for tool T1, from a feed rate of 0.20 mm/rev (a) to 0.05mm/rev (b) of approximately 28% (17N) for the conventional 316L, and of approximately 24% (12N) for the AM 316L. As for the dependency upon depth of cut, similarly to what was stated for the feed force, there is not a clear tendency for both materials and tools.

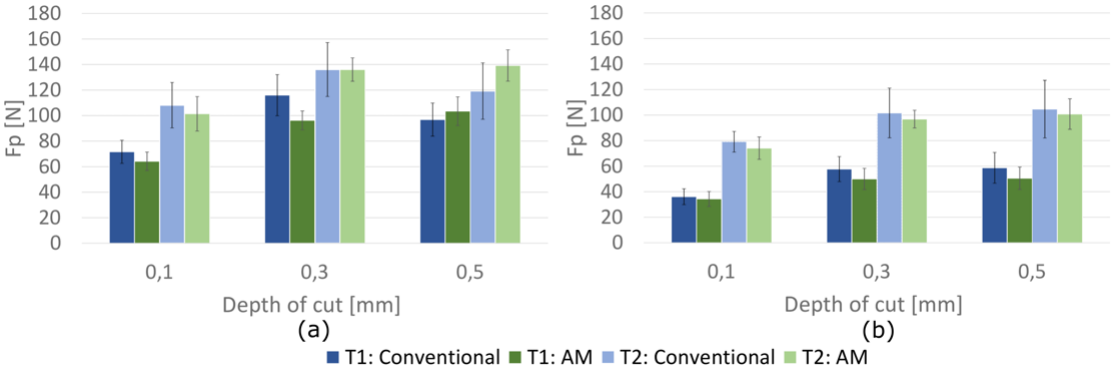


Figure 7.3: Evolution of the penetration force as a function of depth of cut for the AM and conventional specimens: (a) $n$=2500 rpm and $f$=0.2mm/rev; (b) $n$=2500 rpm and $f$=0.05mm/rev

### 7.1.2 Evolution of the main cutting force

Figure 7.4 shows the average cutting force ($F_c$), as a function of cutting speed, feed and depth of cut, of both AM and conventional 316L, for both cutting tools, T1 and T2. Again, the average cutting force values obtained for the AM material, machined with cutting tool T1, are in agreement with what was found in literature [78] for similar turning conditions, showing slight differences that can be attributed to differences in cutting speeds.

An analysis of the graphics in Figure 7.4 confirms what was stated in Section 3.6; more specifically that an increase in depth of cut and/or feed results in higher cutting forces, which is verified for both materials (AM and conventional) and both tools (T1 and T2). This is due to an increased chip section, which demands a higher cutting force to shear the chip.

Concerning the cutting speed, the conclusions drawn from these turning experiments slightly deviate from what was expected; that an increase in cutting speed would result in a decrease in cutting force, which can relate to the low cutting speeds tested, and the small difference between them for the same feed and depth of cut. In addition, when turning with low cutting speeds, this variation is more complex for materials that tend to form build-up edges [49], as is the case in these experiments as will be discussed ahead, in Section 7.3. Although the average cutting force

decreases with an increase of cutting speed for tool T2, with the exception of what is found for the combination of lowest feed and depth of cut (Fig. 7.4(a)), which is also where the smallest difference in cutting speed is (22 m/min), the same can not be stated for tool T1. For the latter, there is no pattern for the variation of cutting force with cutting speed, being that for different combinations of feed and depth of cut, the cutting force either increases or maintains approximately the same, with an increase in cutting speed. The only case where a considerable decrease is observed, for both the AM and conventional material, is for the combination of highest feed and depth of cut (Fig. 7.4(i)), which is also where the biggest difference in cutting speed is found (33m/min). The conclusion that can be taken, is that the cutting tool T2, the one without chip breaker, presents more sensitivity to an increase in cutting speed. Such increase may lead to higher temperatures in the flow zone and reduced contact area [49], which in turn favours the chip formation.

For all conditions tested, and for both the AM and conventional 316L, the cutting tool without chip breaker (T2) presents the highest cutting forces, which is in agreement with what was expected, since the use of a chip breaker promotes the chip evacuation, hence a lower resistance to shearing translates in decreased cutting forces.

Comparing the cutting forces of the AM and conventional material, there is not a clear pattern, for the cutting conditions tested, to take conclusions from. Although the AM specimens tested under quasi-static compression tests presented a higher mechanical resistance comparing to the conventional material, Section 6.2.6, there is not a direct relation to the turning experiments, since these results do not account for temperature effects. The high temperatures involved in turning result in material softening, thus the cutting forces for the AM material are not necessarily higher, as is depicted from the graphics (Fig. 7.4). The fact that the state of stress in the primary shear zone is a mixture of shear and compression does not allow for a direct relation regarding the characterization in compressive loading conditions.

To inquire about the fluctuations in the cutting force measurements for both AM and conventional, Figure 7.5 shows the force spectrum, for different cutting conditions; Fig. 7.5(a) and (b) for the case portrayed in Fig. 7.4(i) and Fig. 7.5(c) and (d) for the one in Fig. 7.4(e). This analysis is complementary to the preceding one, since this gives a more clear idea of what happened during the turning experiments. These graphics show that both materials experienced a similar fluctuation on the measured forces, which can be attributed in some extent to the vibration frequencies of the components involved in the process, where the defects presented in the AM material did not result in higher load scatter or higher extreme peaks. One conclusion that can be pointed out, from analyzing these graphics, is that for finer cutting conditions (Fig. 7.5(c)(d)) the magnitude of the force spectrum is lower comparing to that resulting of higher depth of cut, feed and cutting speed.

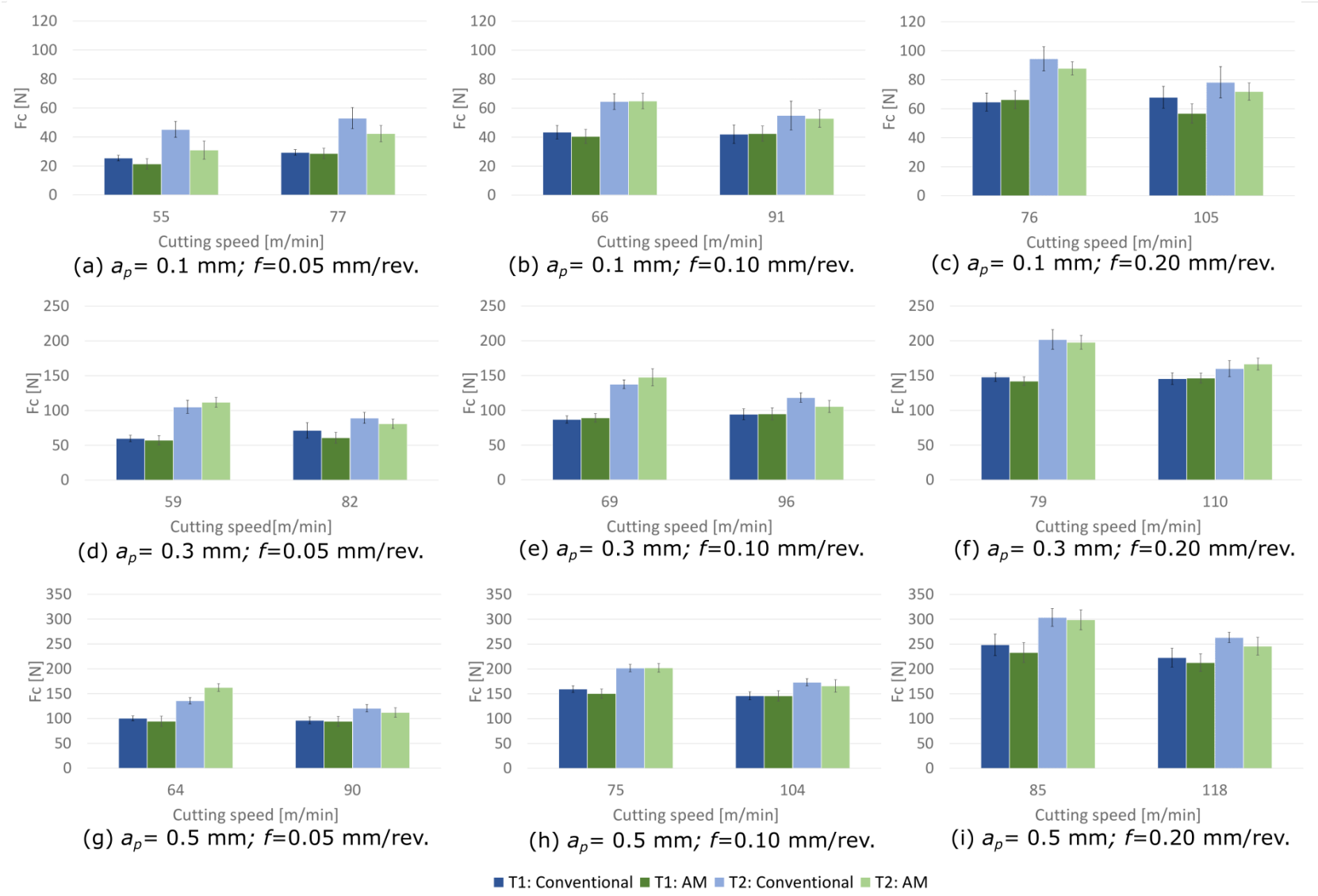


Figure 7.4: Evolution of the cutting force as a function of cutting speed, for the AM and conventional specimens, and for the different cutting conditions.

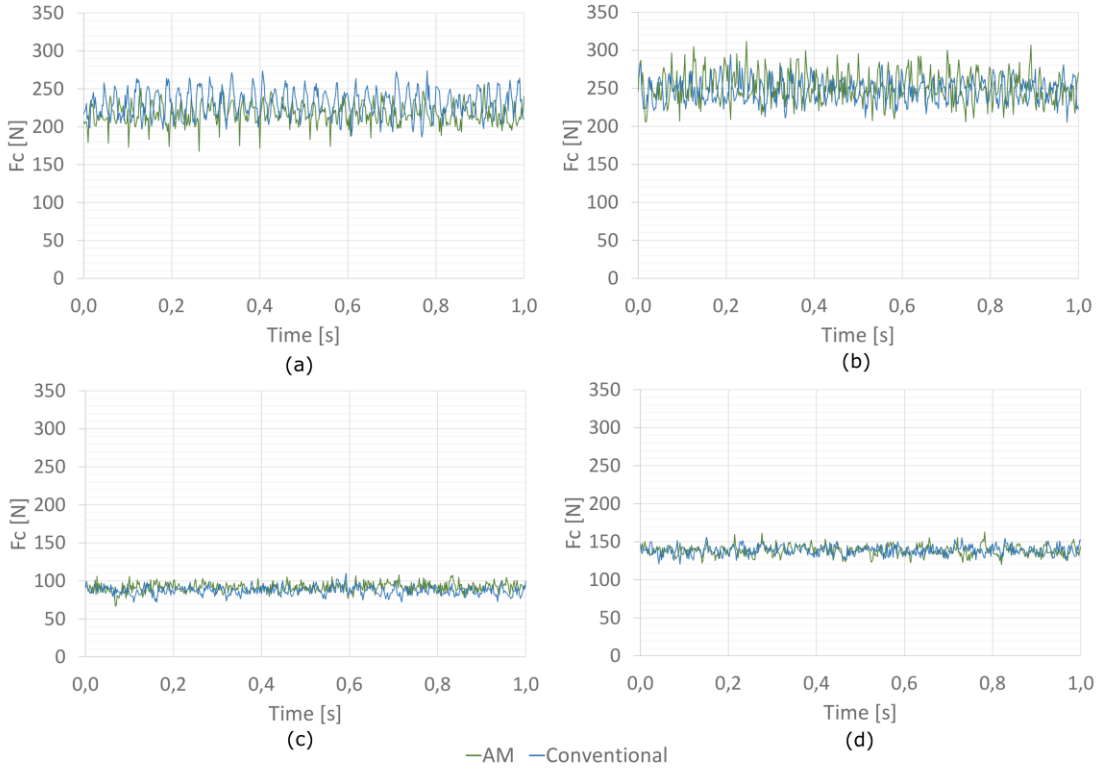


Figure 7.5: Cutting force spectrum of the AM and conventional 316L; for $v_c$=118 m/min, $f$=0.20 mm/rev and $a_p$=0.5 mm: (a) tool T1, (b) tool T2; and for $v_c$=69 m/min, $f$=0.10 mm/rev and $a_p$=0.3 mm: (c) tool T1, (d) tool T2.

### 7.1.3 Cutting power

The main cutting forces of the turning experiments, allow for estimating the cutting power required with respect to the different cutting conditions, from Equation 3.14. This enables the comparison, from a energetic point of view, between both AM and conventional 316L and between cutting tools.

In order to understand the influence of the cutting conditions on the resulting cutting power, its evolution as a function of feed rate and depth of cut, for a rotation frequency of 2500 rpm, is shown in Figures 7.6 and 7.7, respectively. From these graphics, it is possible to observe that the cutting power presents an approximately linear variation with both feed rate and depth of cut, for both cutting tools and materials.

Regarding the cutting tools, the one without chip breaker, T2, presents an overall greater power consumption than that of cutting tool T1, which is in agreement with what was expected, since this tool also resulted in higher cutting forces (Section 7.1.2).

For the majority of cutting conditions analyzed, the cutting power of the conventional material is higher than that of the AM one, or otherwise approximately equal, for both cutting tools.

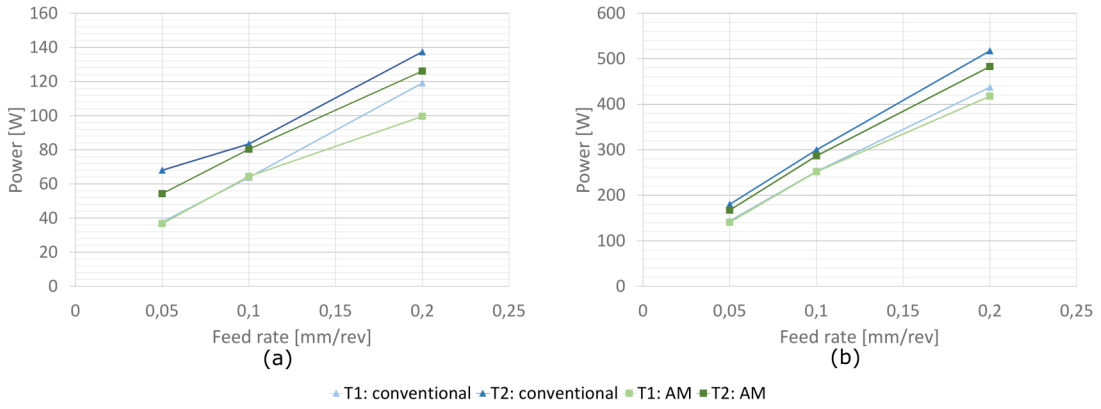


Figure 7.6: Cutting power as a function of feed rate for the AM and conventional specimens: (a) $n$=2500 rpm and $a_p$=0.1 mm; (b) $n$=2500 rpm and $a_p$=0.5 mm.

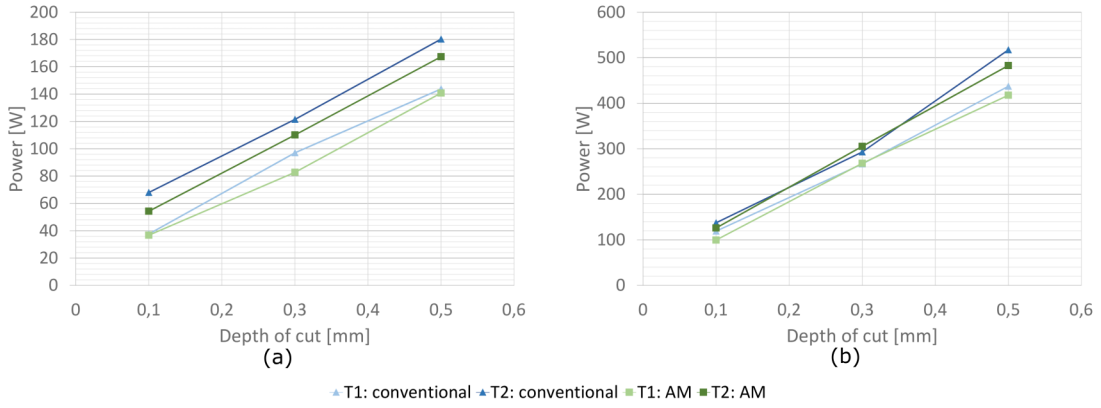


Figure 7.7: Cutting power as a function of depth of cut for the AM and conventional specimens: (a) $n$=2500 rpm and $f$=0.05 mm/rev; (b) $n$=2500 rpm and $f$=0.20 mm/rev.

### 7.1.4 Specific cutting pressure

Table 7.1 shows the cutting pressure ($K_c$), calculated from Equation 3.15, for the different combinations of depth of cut and feed rate, for both rotation frequencies tested. The highest value for the cutting pressure is achieved for the lowest area of the chip section, as was expected, for both tools and rotation frequencies. Of all experiments conducted, the highest cutting pressure, of 10603 MPa, is achieved when machining the conventional material with cutting tool T2, 0.05 mm/rev feed rate, 0.1 mm depth of cut and $v_c$=77m/min (n=2500rpm).

From the graphics in Figures 7.8 and 7.9 it is possible to observe an exponential growth tendency of the cutting pressure with a decrease of the chip cross-sectional area. Extrapolating these results, it is expected that for higher values of depth of cut and feed rate, the cutting pressure will have the tendency to become constant. It is in this range of cutting parameters (high depths of cut, feed rates and cutting speeds) that the cutting pressure becomes relevant for estimating the cutting forces involved in the process, by knowing beforehand the cross-sectional area of the chip.

Table 7.1: Cutting pressure, $K_c$, of the AM and conventional 316L, for different cutting conditions ($f$ and $a_p$) and tools (T1 and T2), for both rotation frequencies, 2500 and 1800 rpm.

| | | | $K_c$ [MPa] | | | | | | | |
|---|---|---|---|---|---|---|---|---|---|---|
| | | | Conventional | | | | AM | | | |
| | | | 2500rpm | | 1800rpm | | 2500rpm | | 1800rpm | |
| $f$ [mm/rev] | $a_p$ [mm] | $S$ [mm$^2$] | T1 | T2 | T1 | T2 | T1 | T2 | T1 | T2 |
| 0.05 | 0.1 | 0.005 | 5866 | 10603 | 5091 | 9055 | 5727 | 8463 | 4286 | 6192 |
| 0.10 | 0.1 | 0.010 | 4202 | 5494 | 4343 | 6455 | 4241 | 5288 | 4050 | 6493 |
| 0.05 | 0.3 | 0.015 | 4752 | 5950 | 3982 | 7009 | 4052 | 5393 | 3812 | 7450 |
| 0.20 | 0.1 | 0.020 | 3393 | 3915 | 3231 | 4726 | 2838 | 3593 | 3313 | 4392 |
| 0.05 | 0.5 | 0.025 | 3854 | 4832 | 4021 | 5437 | 3773 | 4486 | 3781 | 6499 |
| 0.10 | 0.3 | 0.03 | 3146 | 3943 | 2895 | 4583 | 3163 | 3518 | 2972 | 4919 |
| 0.10 | 0.5 | 0.05 | 2920 | 3469 | 3190 | 4036 | 2916 | 3316 | 3009 | 4044 |
| 0.20 | 0.3 | 0.06 | 2425 | 2665 | 2463 | 3366 | 2438 | 2776 | 2366 | 3296 |
| 0.20 | 0.5 | 0.100 | 2227 | 2634 | 2486 | 3036 | 2127 | 2458 | 2330 | 2988 |

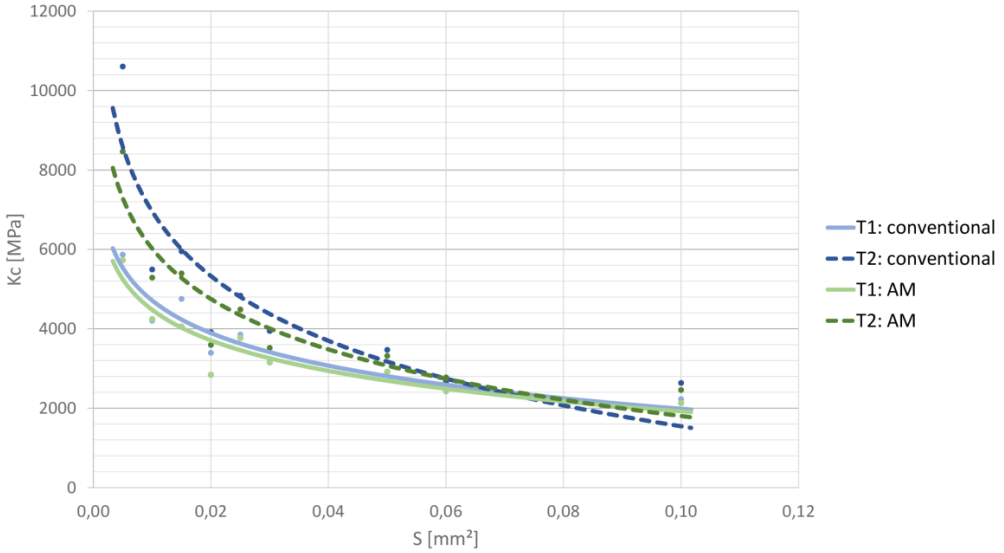


Figure 7.8: Cutting pressure, $K_c$, as a function of the area of the chip section, $S$, for the conventional and AM 316L, for a rotation frequency of 2500 rpm.

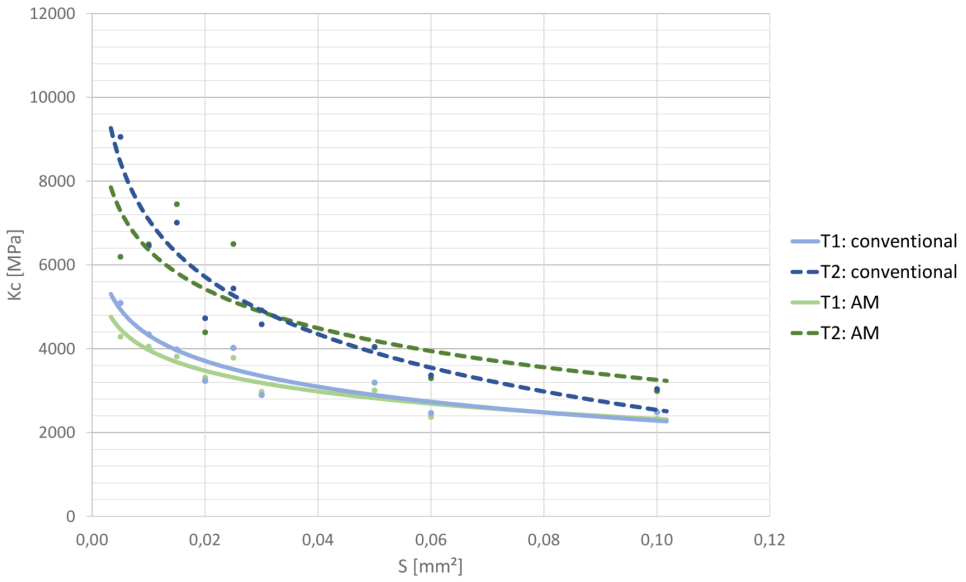


Figure 7.9: Cutting pressure, $K_c$, as a function of the area of the chip section, $S$, for the conventional and AM 316L, for a rotation frequency of 1800 rpm.

## 7.2 Chip analysis

After each test, samples of the resultant chips were collected for analysis and classification in accordance to ISO 3685 standard (Figure 3.9), the result is shown in Table 7.2. A comparative chart with the different shape and size chips with respect to the different cutting conditions and type of cutting tool is shown in Figures 7.10 and 7.11 for the conventional and AM material, respectively.

The chip form is an important criterion to determine the machinability in continuous processes, as is the case of turning, since it has an essential influence on process safety. From Table 7.2, it is possible to select the cutting parameters, for each cutting tool and material, that lead to a favourable chip formation. These favourable chips are all short, either tubular, spiral or conical (Type 2.2; 4.2; 5.2), and translate into a good surface finish and ease of chip disposal.

For both cutting tools, the smallest feed rate ($f$=0.05 mm/rev) and depth of cut ($a_p$=0.1 mm), which also correspond to the lower cutting speeds, lead to unfavourable chip formation, either long, snarled or discontinuous chip segments. This can be attributed to the lower attained stresses in thinner chips, that may not be enough to cause the chip to heavily deform leading to fracture. The chip breaker of tool T1 only leads to favourable chip forms for feed rates of 0.10 mm/rev and higher, given that for the lowest feed the plastic stress achieved by bending the chip is not high enough to break it [51]. Concerning the cutting speed, higher values lead to an increase in temperature on the chip formation zone, which increases the ductility of the steel resulting in less damage of the workpiece during the chip formation process [51].

Table 7.3 indicates the range of cutting parameters, for each tool with respect to the workpiece material, that lead to favourable chip formation. From this, it is noticeable that the AM 316L

Table 7.2: Classification of the chips, collected during the turning experiments, in accordance with ISO 3685 standard.

| | | | | Conventional | | AM | |
|---|---|---|---|---|---|---|---|
| Rotation frequency | Feed | Depth of cut | Cutting speed | Tool | | Tool | |
| [rpm] | [mm/rev] | [mm] | [m/min] | T1 | T2 | T1 | T2 |
| 2500 | 0.20 | 0.5 | 118 | 5.2 | 4.2 | 5.2 | 4.2 |
| | | 0.3 | 110 | 2.1 | 4.1 | 2.2 | 5.2 |
| | | 0.1 | 105 | 2.1 | 2.3 | 2.3 | 2.3 |
| | 0.10 | 0.5 | 104 | 4.2 | 4.2 | 4.2 | 4.2 |
| | | 0.3 | 96 | 4.2 | 4.2 | 4.2 | 4.2 |
| | | 0.1 | 91 | 2.3 | 4.3 | 2.1 | 4.3 |
| | 0.05 | 0.5 | 90 | 5.1 | 2.1 | 2.2 | 5.3 |
| | | 0.3 | 82 | 5.3 | 4.1 | 2.3 | 5.3 |
| | | 0.1 | 77 | 6.2 | 6.2 | 6.2 | 6.2 |
| 1800 | 0.20 | 0.5 | 85 | 5.2 | 4.2 | 5.2 | 4.2 |
| | | 0.3 | 79 | 2.1 | 4.2 | 2.2 | 5.2 |
| | | 0.1 | 76 | 2.1 | 2.3 | 2.1 | 2.3 |
| | 0.10 | 0.5 | 75 | 4.2 | 4.2 | 5.2 | 4.2 |
| | | 0.3 | 69 | 4.2 | 4.2 | 4.2 | 4.2 |
| | | 0.1 | 66 | 2.3 | 4.3 | 2.1 | 1.1 |
| | 0.05 | 0.5 | 64 | 5.1 | 2.3 | 5.2 | 1.2 |
| | | 0.3 | 59 | 5.3 | 4.3 | 5.1 | 6.2 |
| | | 0.1 | 55 | 6.2 | 4.1 | 6.2 | 4.3 |

2.2; 4.2;5.2: favourable chips.

allows for a wider range of depths of cut, compared to the conventional material. Moreover, the range of parameters for both tools is similar which can be an indicator that the use of a chip breaker, for the cutting conditions tested, is not crucial for the type of chip generated (short, long or segments) but has an influence on the chips' form (conical or helical), as can be further observed in the SEM images of Figures 7.12 and 7.13, where the first shows conical chips obtained from machining with cutting tool T1, and the second helical chips obtained from machining with cutting tool T2. This difference can be related to the direction of chip flow, which is influenced by the geometry of the chip breaker.

Table 7.3: Ideal cutting parameters for favourable chip formation for each cutting tool with respect to the material and cutting speed.

| | | $v_c$ [m/min] | | | |
|---|---|---|---|---|---|
| | | 69 - 85 | | 96 - 118 | |
| Tool | Material | $a_p$ [mm] | $f$ [mm/rev] | $a_p$ [mm] | $f$ [mm/rev] |
| T1 | Conv. | 0.5 | 0.10-0.20 | 0.5 | 0.10-0.20 |
| | AM | 0.3-0.5 | 0.10-0.20 | 0.3-0.5 | 0.10-0.20 |
| T2 | Conv. | 0.3-0.5 | 0.10-0.20 | 0.5 | 0.10-0.20 |
| | AM | 0.3-0.5 | 0.10-0.20 | 0.3-0.5 | 0.10-0.20 |

For both cutting tools tested with the maximum feed rate and depth of cut (0.20mm/rev and

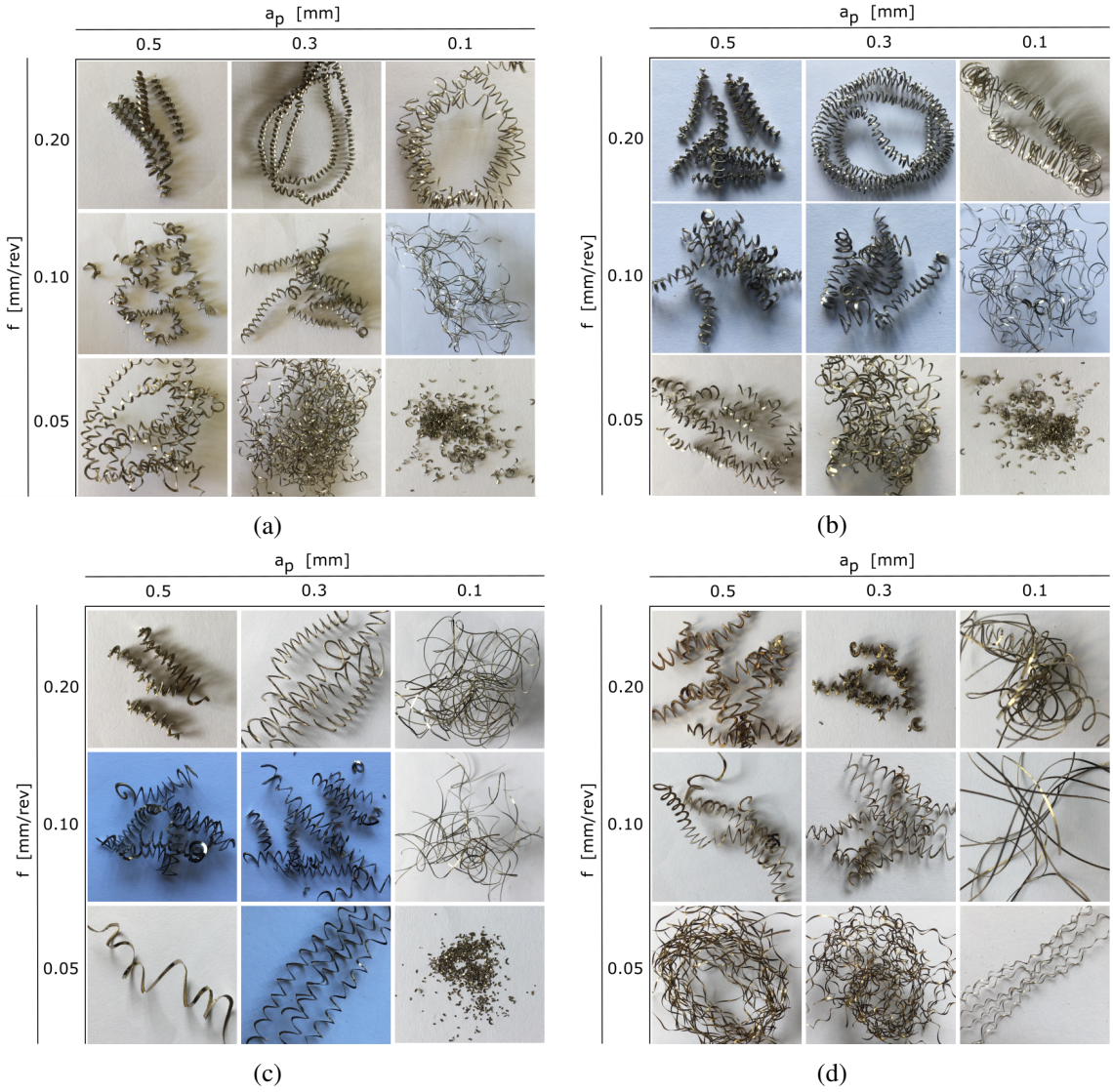


Figure 7.10: Chip geometry of the conventional material obtained from the turning experiments with: (a) T1, n=2500rpm; (b) T1, n=1800rpm; (c) T2, n=2500rpm; (d) T2, n=1800rpm.

0.5mm), the AM and conventional material show a serrated chip formation, characterized by a saw-tooth appearance (Fig. 7.12 and 7.13), as explored in Section 3.3.1.2. This is typical when cutting materials with low heat conductivity and high strength [79], and arises from an increased deformation in the shear zone, due to larger thermal softening of the material compared to strain and strain rate hardening, which results in the formation of a narrow band from where the heat conduction is negligible, so that the surrounding material is only slightly deformed [80]. Figures 7.12(b)(d) and 7.13(b)(d) show the adiabatic shear bands (ASB) in detail, were measurements of the adiabatic shear band spacing (ASBS) were taken; an average of 84$\mu$m for both materials machined with cutting tool T1, and an average of 135$\mu$m for both materials machined with cutting tool T2. These results lead to thinking that this spacing is not only dependent on the type of material but also on the cutting tool.

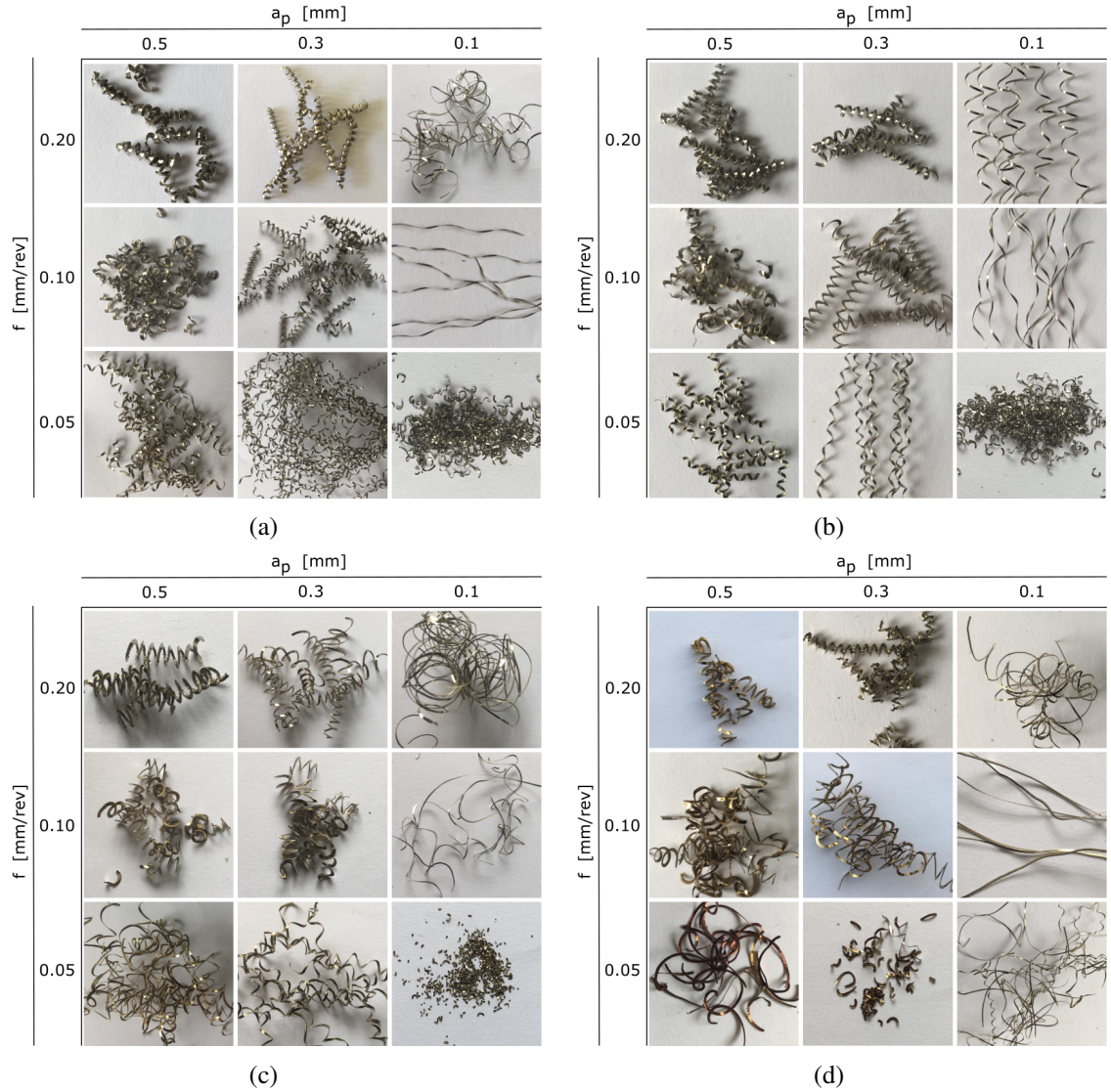


Figure 7.11: Chip geometry of the AM material, obtained from the turning experiments with: (a) T1, n=2500rpm; (b) T1, n=1800rpm; (c) T2, n=2500rpm; (d) T2, n=1800rpm.

From Figures 7.12 to 7.14 it is noticeable the difference in the surfaces topography of the same chip. The side of the chip that was in contact with the cutting tool reveals a smoother surface, arising from high contact pressures, temperatures and friction conditions in the tool-chip interface. This is further evidenced by Figure 7.14(d), where the boundary between these surfaces is showed in detail. Figure 7.14 shows some of the particularities found in the chips obtained from machining the AM specimens; specifically the well pronounced striations in the shear bands and porosity defects (Fig. 7.14(b)), and an increased depth between shear bands (Fig. 7.14(c)), that all together render the AM chips more brittle than the conventional ones, which was verified from their susceptibility for breakage during handling.

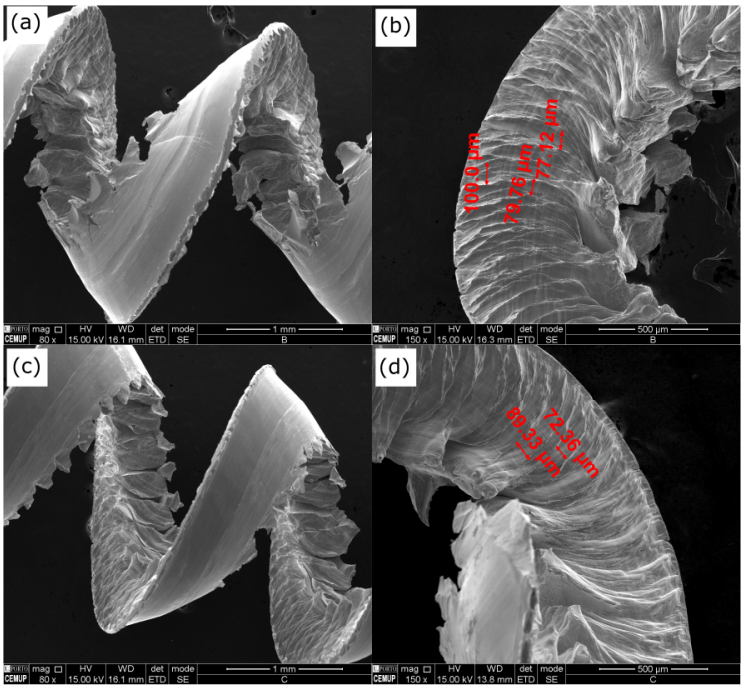


Figure 7.12: SEM images of the chips obtained from machining with cutting tool T1, $f$=0.20mm/rev, $a_p$=0.5: (a) conventional 316L, showing ASBS (b); (c) AM 316L, showing ASBS (d).

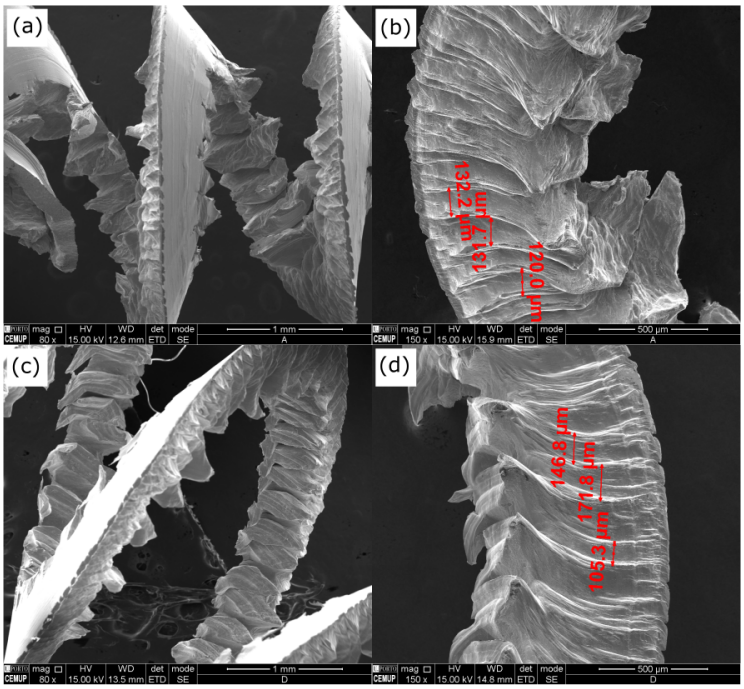


Figure 7.13: SEM images of the chips obtained from machining with cutting tool T2, $f$=0.20mm/rev, $a_p$=0.5: (a) conventional 316L, showing ASBS (b); (c) AM 316L, showing ASBS (d).

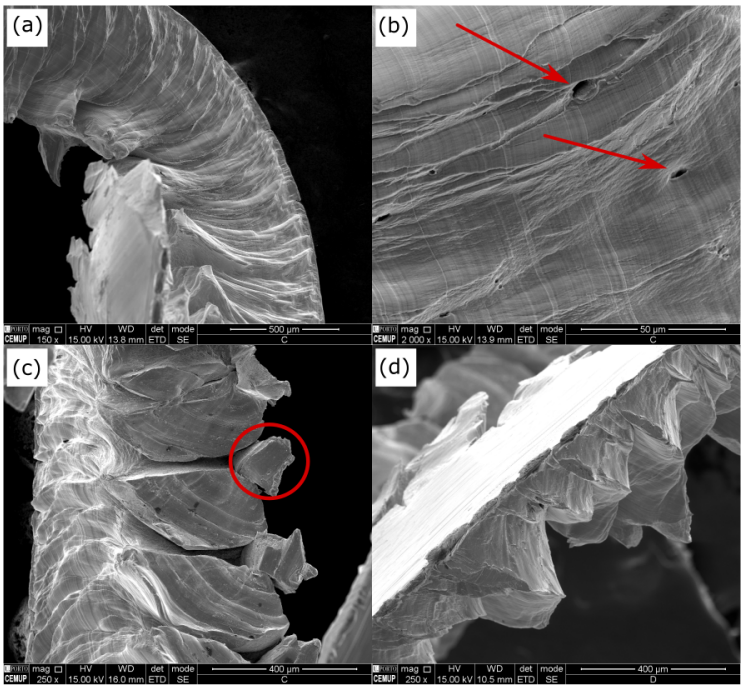


Figure 7.14: SEM images of the AM 316L chips obtained from machining with $f$=0.20mm/rev, $a_p$=0.5mm and: cutting tool T1 showing the ASB (a), porosity defects (b) and a detail of the saw-tooths; cutting tool T2 showing in detail the boundary between surfaces of the chip (d).

## 7.3 Surface analysis

### 7.3.1 Cutting tools surface analysis

A surface analysis of both cutting tools was conducted by scanning electronic microscopy, to infer on the tool wear of the rake face. In addition a energy-dispersive X-ray spectroscopy (EDS) analysis was conducted (Appendix D), in order to identify the compositional changes in the tool's surface, namely if there was any build-up edge formation during the experimental tests.

Figure 7.15 shows that both tools experienced crater wear, which consists of a cavity in the rake face of the tool that arises from the action of the chip sliding against the surface [46]. As a consequence of the abrasion between the work material and the tool, small portions of the tool's coating were removed, revealing the substrate material, as was verified by EDS. In addition, both tools revealed the formation of build-up edges.

The electron backscatter diffraction (EBSD) image of the cutting tool T2 (Fig. 7.15(d)) shows zones with different light intensities, corresponding to distinct chemical compositions. In this image are indicated five zones which were subjected to chemical characterization, the results revealed that Z1 corresponds to SS316L, Z2 to $Al_2O_3$, Z3 to TiCN, Z4 to SS316L and Z5 to WC. Regarding the cutting tool T1, from Figure 7.15(b), it is possible to distinguish that the chip breaker is damaged, and in its place has formed a build-up edge, which correlates with the deviations of the main cutting forces from what was expected (Section 7.1.2).

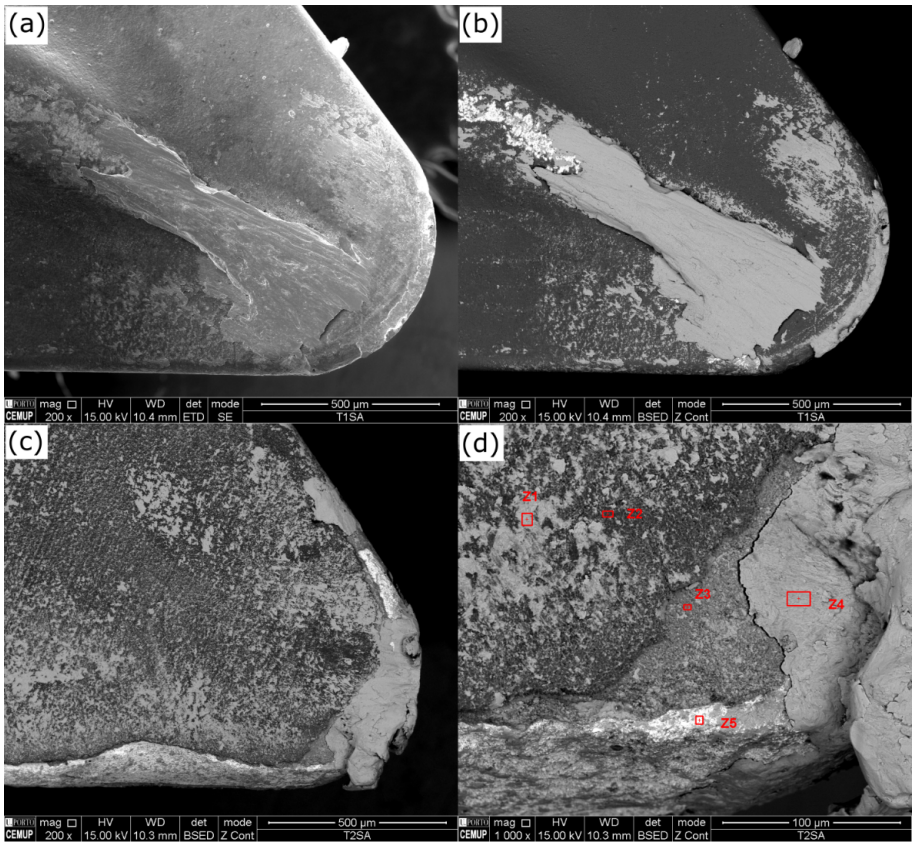


Figure 7.15: SEM images of the cutting tools' surface: (a)(b) DCGT, T1; (c)(d) DCMW, T2.

### 7.3.2 Workpiece surface analysis

The average surface roughness values (Ra and Rmax) of the machined samples, both conventional and additively manufactured, are expressed in Table 7.4, as well as the theoretical roughness values, calculated from Equations 3.17 and 3.18.

Table 7.4: Surface roughness values after machining, in $\mu$m, with $n$=1800 rpm and $a_p$=0.3 mm.

| | | Conventional | | AM | | Theoretical | |
|---|---|---|---|---|---|---|---|
| Tool | Feed [mm/rev] | Ra | Rmax | Ra | Rmax | Ra | Rmax |
| T1 | 0.05 | 0.41 | 3.43 | 0.38 | 2.43 | 0.20 | 0.78 |
| | 0.10 | 0.93 | 5.34 | 0.87 | 4.41 | 0.78 | 3.13 |
| | 0.20 | 2.37 | 11.45 | 1.93 | 8.88 | 3.13 | 12.50 |
| T2 | 0.05 | 0.70 | 4.51 | 0.41 | 3.46 | 0.20 | 0.78 |
| | 0.10 | 1.35 | 6.44 | 1.09 | 5.10 | 0.78 | 3.13 |
| | 0.20 | 3.22 | 14.70 | 2.65 | 12.75 | 3.13 | 12.5 |

As expected, an increase in feed rate resulted in an increased surface roughness for all samples, which is coherent with what was found in literature [43]. This tendency can be well recognized by observing the graphic in Figure 7.16.

Some conclusions can be drawn from these results; first, the average surface roughness of the

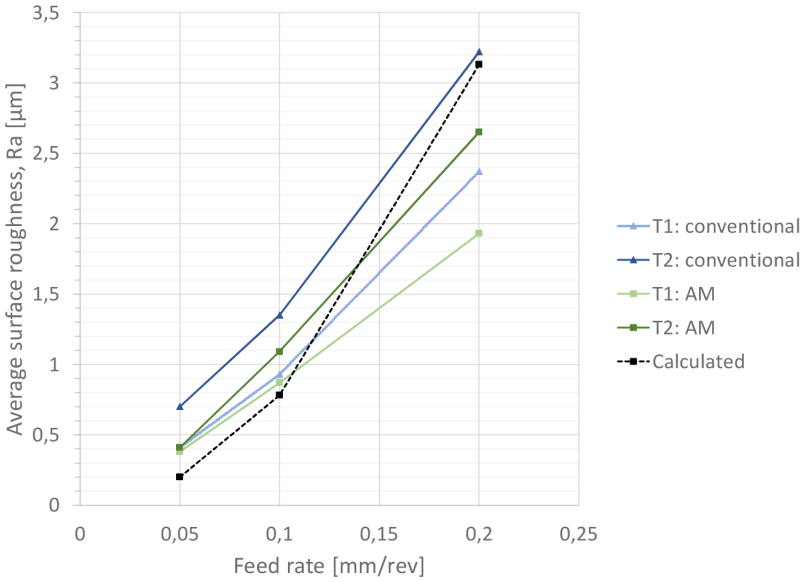


Figure 7.16: Surface roughness of the AM and conventional AISI 316L, after machining, as a function of the feed rate.

machined conventional specimens is higher than that of the AM specimens, for the same cutting tool and all feed rates. Particularly, for a feed rate of 0.20 mm/rev, the conventional specimens present an approximately 23% higher average surface roughness than the AM ones when machined with cutting tool T1, and approximately 22%higher when machined with cutting tool T2. And second, the average surface roughness of the specimens machined with cutting tool T2 is higher than that of the specimens machined with T1 (approximatelly 37% for the AM material machined with $f$=0.20mm/rev), which can be explained by the absence of a chip breaker. The flat rake face of the tool promotes a continuous chip formation, which winds around the workpiece in the cutting area jeopardizing the surface finish.

Figure 7.17 shows an example of the steps involved in the digital roughness measurements of the cylindrical specimens after machining, from the three dimensional cylindrical surface until the linear roughness profile From the three dimensional graphics, it is possible to observe the waving effects on the surface, resulting from the turning operation.

Figure 7.18 shows the scanning electron microscopy images of the AM specimen's surface machined with the cutting tool without chip breaker, T2. Figure 7.18(a) shows the surface contour resulting from machining with a feed rate of 0.20 mm/rev, which corresponds to the highest measured surface roughness arising from the pronounced feed marks. This turning operation also resulted in defects on the machined surface, such as the marks shown in Figure 7.18(b). As the feed rate decreases, the feed marks become less pronounced (Fig. 7.18(c) and (e)), in accordance to

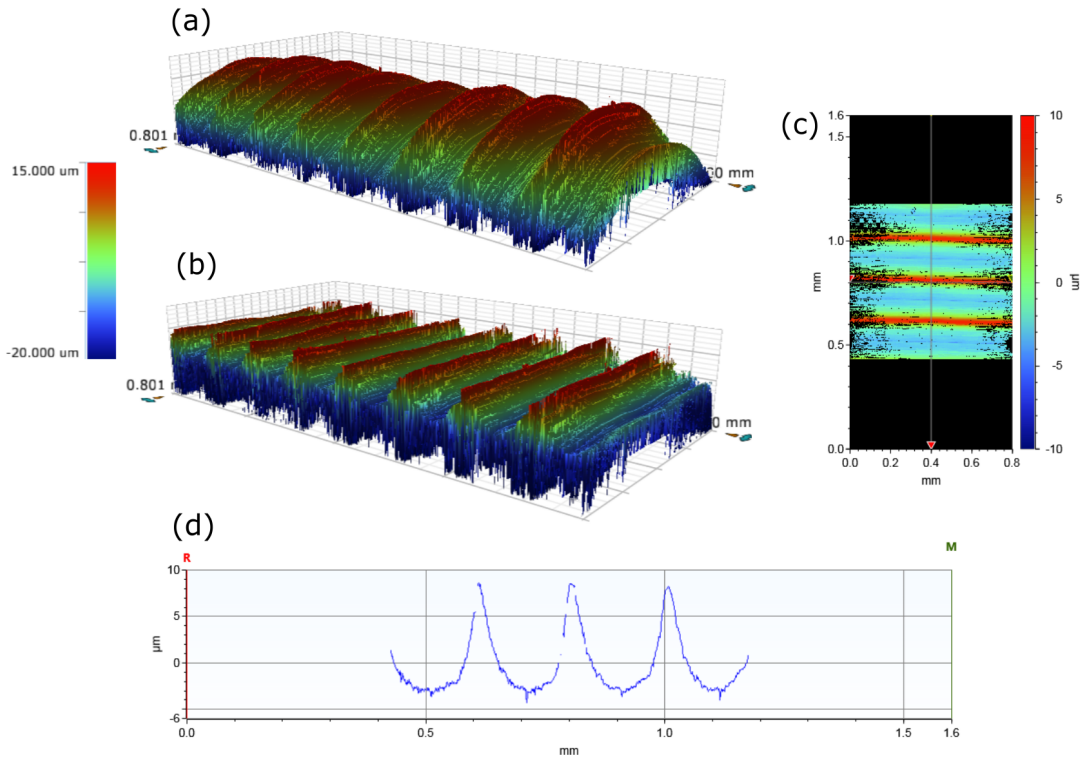


Figure 7.17: Surface roughness measurements by optical profilometer of the AM specimen machined with cutting tool T1 ($f$=0.20mm/rev): (a) 3D roughness distribution on the actual cylindrical surface; (b) respective 3D roughness distribution after conversion to a planar surface; (c) surface roughness distribution after filtering; (d) respective linear roughness profile.

what was stated in Section 3.7, however broken portions of chips can be observed embedded into the surface (Fig. 7.18(d) and (f)), resulting from breakage of the build-up edges formed in the tool's rake face (see Fig. 7.15). Additionally, an oblique waving effect can be observed on the surfaces machined with feed rates of 0.10 and 0.05 mm/rev (Fig. 7.18(c)(e)), being strongly pronounced for the latter, overcoming the effects of the feed marks on the surface contour (Fig. 7.18(e)).

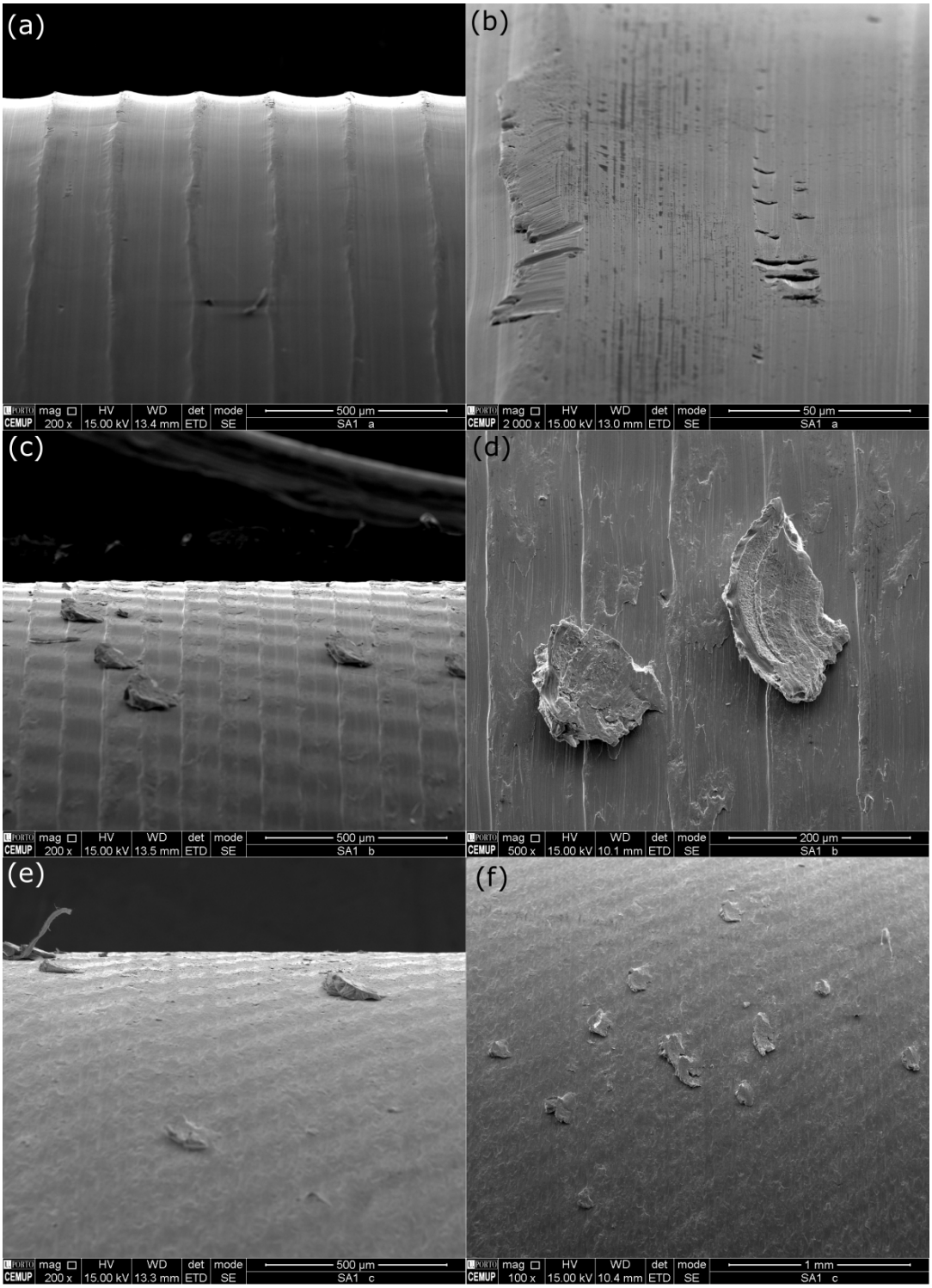


Figure 7.18: SEM images of the AM specimen's surface machined with the cutting tool T2: (a)(b) $f$=0.20 mm/rev; (c)(d) $f$=0.10 mm/rev; (e)(f) $f$=0.05 mm/rev.

# Chapter 8

# Orthogonal metal cutting preliminary studies

## 8.1 Introduction

In this chapter a numerical simulation of AISI 316L orthogonal cutting, using Deform$^{TM}$2D, was conducted. These simulations will be used to assist the design of orthogonal cutting studies to be preformed on future research on machinabillity studies on both the conventional and aditivelly manufactured steels.

The objective of this study is to infer about cutting forces involved in the process and chip formation, concluding with a comparison between the AM and conventional materials. This study aims for future validation with experimental data, from instrumented tests in a shaping machine, to which a fixation system has already been developed for adapting the KISTLER 257B piezoeletric dynamometer to it (Appendix E).

Initially an analysis of the kinematics of the mechanism, considered for the future experimental tests, was conducted, in order to identify the attainable speeds and allowable movements. The mechanism in question - quick return mechanism, is usually used as the base for shaping machines, as the one in Figure 8.1.

The parameters obtained from these analysis together with workpiece material and tool material and geometry enabled the numerical simulation of the process. These were 2D metal cutting simulations, using Deform$^{TM}$2D which aimed at reducing high computational times characteristic of this numerical simulations.

## 8.2 Quick-return mechanism

### 8.2.1 Kinematic analysis of a quick-return mechanism

The goal of kinematic analysis is to investigate the motion of individual components of the mechanism in dependence with the driver's motion, that is to calculate the position, velocity and acceleration of any of the mechanism points or links. For such analysis, the linkage dimensions

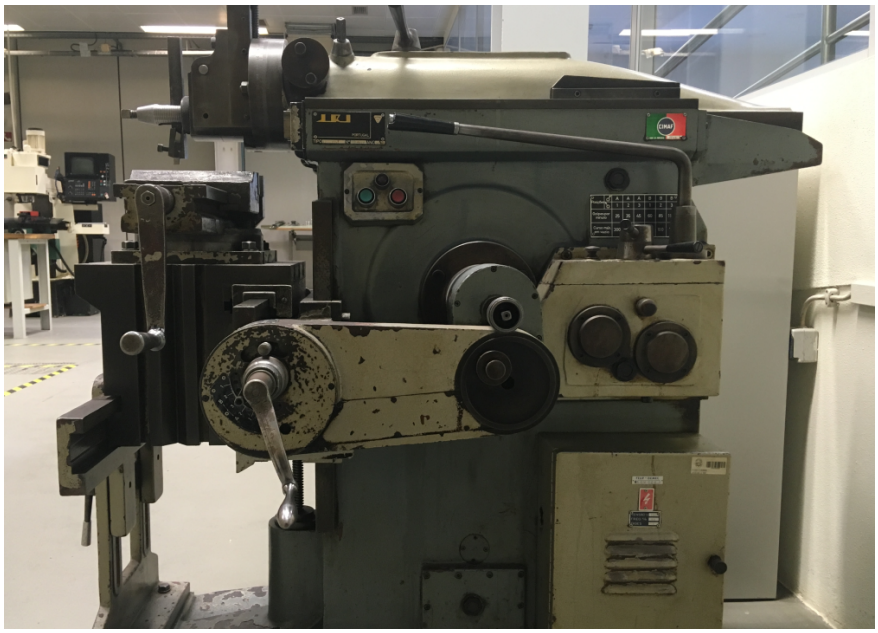

Figure 8.1: Shaping machine type L2-03.6 (DEMec).

as well as position, velocity and acceleration of as many points or links as degrees of freedom the linkage has, needs to be known [81].

This mechanism's kinematics was analytically analyzed, using numerical methods such as trigonometric rules, functions and differentiation. The basis for this analyzes is shown in Figure 8.2 - a kinematic scheme of the quick-return mechanism, where number 1 represents the frame and 2 the crank (or driver) that rotates at a constant angular velocity $\omega_{21}$.

The objective of this analysis is to define the movement of the ram, component 6, since the cutting tool is placed at the end of it. Other components, such as the sliding block 3, the rocker arm 4 and the connecting link 5 are responsible for connecting all parts of the mechanism and for transmitting motion.

In Figure 8.2, $O_{41}$ represents the origin of the coordinate system, and all points are described in terms of their relative position (x,y) from there. The angle $\phi_{21(t)}$ is a function of time $t$, and its kinematic dependency on time, if the angular velocity $\omega_{21}$ is constant, can be expressed as:

$$\omega_{21} = \frac{d\phi}{dt} \tag{8.1}$$

$$\int_0^{\phi_{21}} d\phi = \omega_{21} \cdot \int_0^t t \tag{8.2}$$

$$\phi_{21} = \omega_{21} \cdot t \tag{8.3}$$

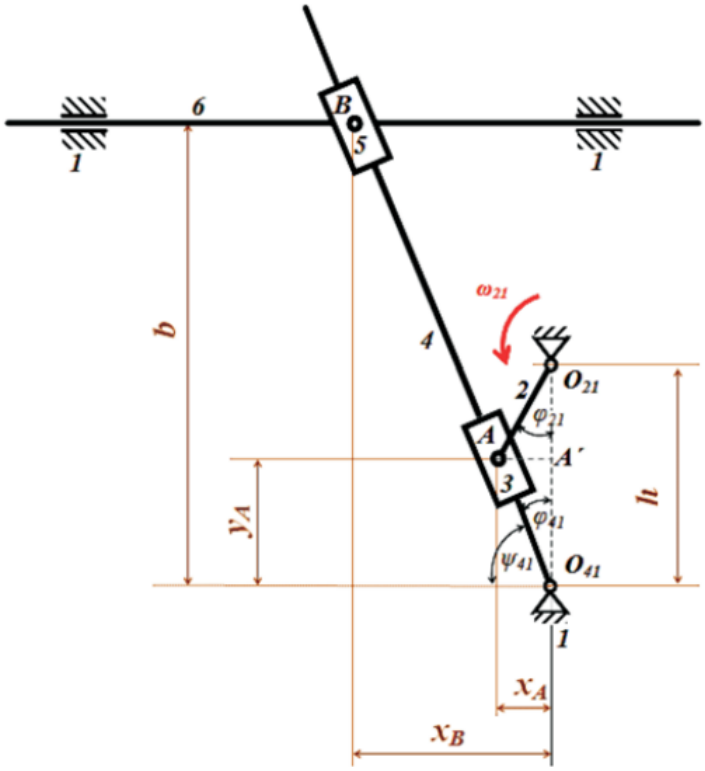


Figure 8.2: Kinematic scheme of a planar quick-return mechanism [82].

The x-coordinate of point B can be written as a function of $\psi_{41}$ by trigonometric relations, as follows:

$$x_B = \frac{b}{tan\psi_{41}} \tag{8.4}$$

Where $\psi_{41} = 90° - \phi_{41}$, resulting in:

$$x_B = \frac{b}{cotan\phi_{41}} = \frac{b}{1/tan\phi_{41}} = b \cdot tan\phi_{41} \tag{8.5}$$

From trigonometric analysis, $tan\phi_{41}$ is given by:

$$tan\phi_{41} = \frac{\overline{A'A}}{\overline{A'O_{41}}} = \frac{r \cdot sin\phi_{21}}{h - r \cdot \phi_{21}} \tag{8.6}$$

By combining Equations 8.3, 8.5 and 8.6, the x-coordinate of point B can be written as a function of the angular velocity $\omega_{21}$, as follows:

$$x_B = b \cdot \frac{r \cdot sin(\omega_{21} \cdot t)}{h - r \cdot cos(\omega_{21} \cdot t)} \tag{8.7}$$

The ram's velocity is the same as point B velocity, $v_B$, and can be obtained by differentiating Equation 8.7 in relation to time $t$:

$$v_B = \frac{dx_B}{dt} = \dot{x}_B \tag{8.8}$$

$$\dot{x}_B = b \cdot \frac{r \cdot \omega_{21} \cdot [h \cdot cos(\omega_{21} \cdot t) - r]}{[h - r \cdot cos(\omega_{21} \cdot t)]^2} \tag{8.9}$$

As for the acceleration of the ram as a function of time, it is obtained by differentiating the velocity in relation to time, as follows:

$$a_B = \frac{dv_B}{dt} = \ddot{x}_B \tag{8.10}$$

$$\ddot{x}_B = -b \cdot r \cdot \omega_{21}^2 \cdot sin(\omega_{21} \cdot t) \cdot C \tag{8.11}$$

Where C is a constant, given as follows:

$$C = \frac{h \cdot [h - r \cdot cos(\omega_{21} \cdot t)] + 2r \cdot [h \cdot cos(\omega_{21} \cdot t) - r]}{[h - r \cdot cos(\omega_{21} \cdot t)]^3} \tag{8.12}$$

This kinematic analysis can be applied to a variety of machines with a quick-return mechanism, as long as the constants, in this case distances and rotation speed, are set accordingly.

### 8.2.2 Shaping machine type L2-03.6

For the machine in question, shaping machine type L2-03.6, the distances $b = 694.5mm$ and $h = 413mm$ (Figure 8.2), were measured from the definition drawing, provided in the technical documents from the manufacturer.

Concerning the radius $r$ it varies according to the ram advances, which also results in different cutting speeds. The radius for each theoretical advance of the machine was calculated, and from that the maximum cutting speed was calculated, the results are shown in Table 8.1.

Table 8.1: Shaping machine type L2-03.6 parameters.

| [1]Angular velocity $\omega$ [rpm] | 25 | 35 | 45 | 60 | 85 | 115 |
|---|---|---|---|---|---|---|
| Max. stroke [mm] | 337.5[2] | 250[1] | 200[1] | 150[1] | 100[1] | 75[1] |
| [3]Radius, $r$ [mm] | 97.55 | 73.20 | 58.90 | 44.34 | 29.67 | 22.00 |
| [4]Max. cutting speed, $v_c$ [m/min] | 20.84 | 22.99 | 24.51 | 25.38 | 24.86 | 25.78 |

For the future orthogonal cutting experiments, it is desirable to have an approximately constant cutting speed throughout the cutting length. Taking this into account, a velocity of 20 m/min

[1]From the shaping machine technical documents.
[2]Measured in the shaping machine.
[3]Calculated for the maximum stroke.
[4]Calculated from Eq. 8.9.

was chosen for the succeeding metal cutting simulations, corresponding to the maximum stroke. Figure 8.3 shows the graphics of the ram velocity, for the maximum stroke, as a function of time (Fig. 8.3(a)) and ram position (Fig. 8.3(b)), showing an acceptable stable zone for the orthogonal cutting experiments. Whereas for the minimum stroke, this zone with constant velocity is considerably smaller (Fig. 8.3(a) and (b)), hence the choice of the maximum stroke for the experiments.

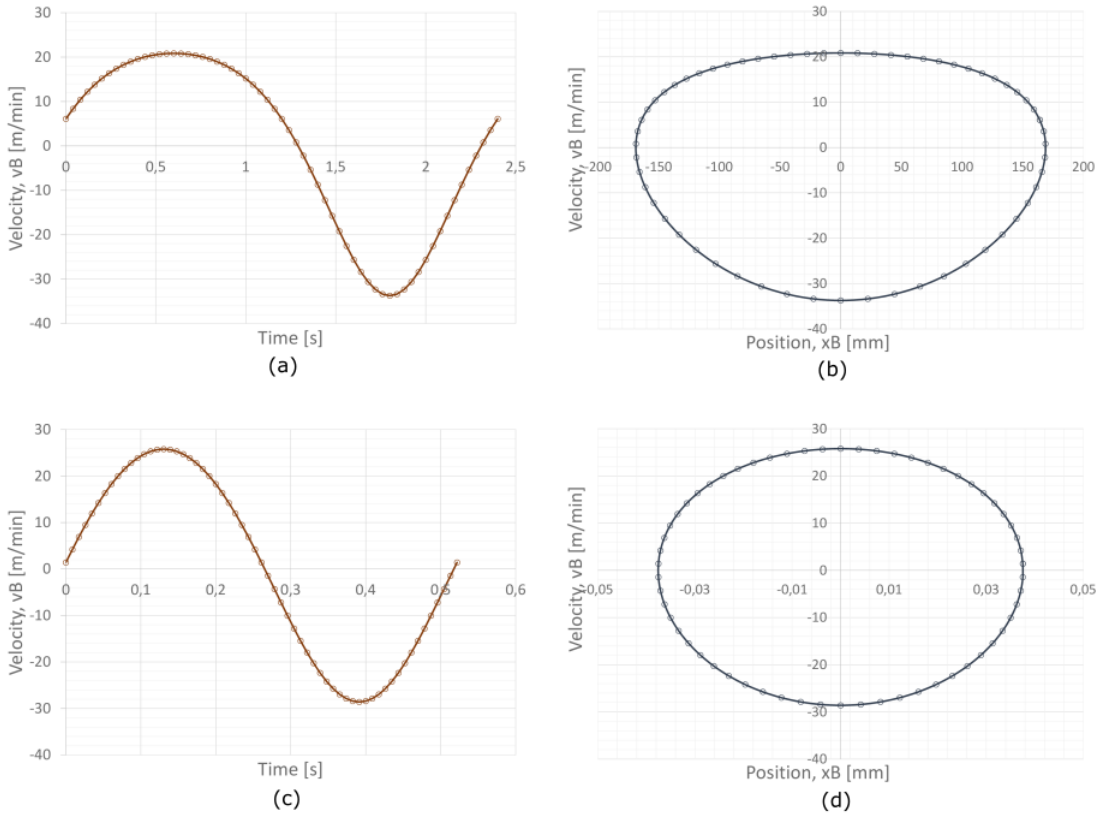


Figure 8.3: Ram velocity, $v_B$, for the maximum stroke as a function of: (a) time, $t$, and (b) position of the ram, $x_B$; and for the minimum stroke as a function of: (c) time, $t$, and (d) position of the ram, $x_B$.

## 8.3 Deform$^{TM}$2D

Deform$^{TM}$2D model is presented in Figure 8.4, this software uses an implicit Lagrangian formulation and includes an automatic remeshing routine, in order to avoid highly distorted meshes [54]. While the tool penetrates the workpiece, the elements at the tip of the tool are separated from the workpiece, enabling the formation of a chip. It is a thermo-mechanical simulation with elastic-plastic material modelling. In the succeeding simulations a shear friction model was used to characterize the friction interaction between the chip and the tool, with a constant shear friction factor of 0.6.

In the succeeding numerical simulations, the influence of two parameters on the cutting forces and chip formation were studied, namely: feed rate and rake angle.

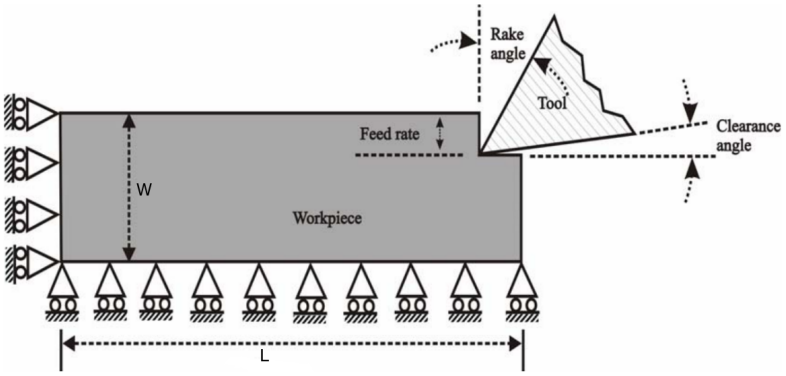


Figure 8.4: Finite element model of Deform2D [83].

### 8.3.1 Material characterization

Deform$^{TM}$has a material library, in which the materials are characterized based on their thermal and elastic properties and their flow stress curves, as a function of temperature, strain and strain-rate. This material library includes conventional AISI 316L, as for the AM material, its characterization had to be based on the flow stress curves from the compression tests (Section 6.2.6).

#### 8.3.1.1 AISI 316L conventionally manufactured

Figures 8.5 and 8.6 show the flow stress curves of AISI316L, as a function of strain, for different temperatures and strain-rates, made from the data in the software's material library.

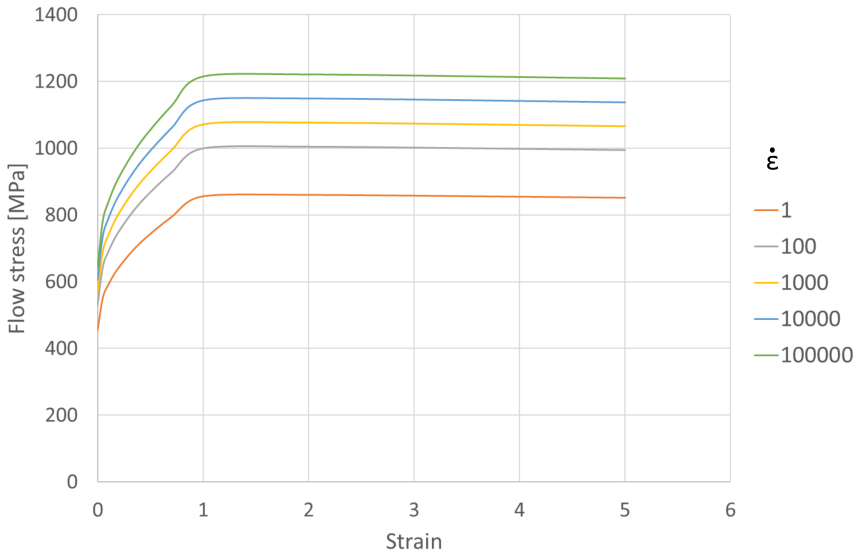


Figure 8.5: Flow stress curves of conventional AISI 316L for different stain rates and a temperature of 20°C.

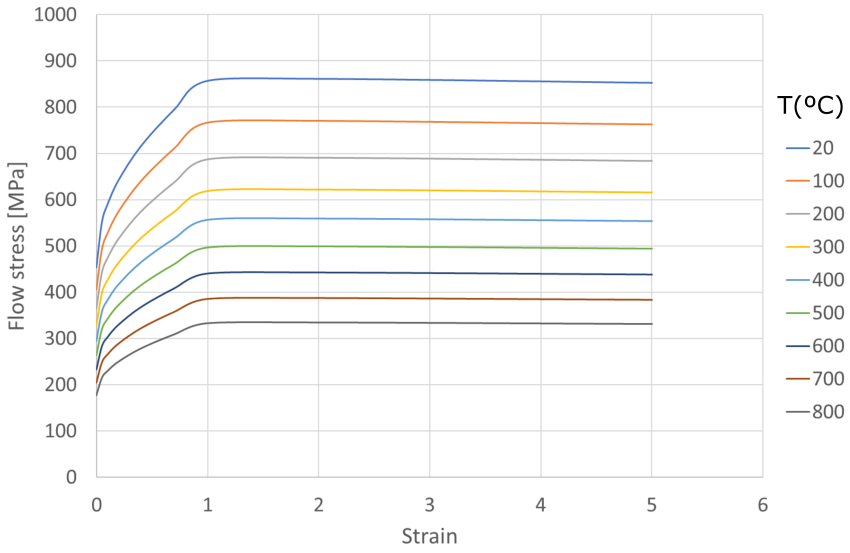


Figure 8.6: Flow stress curves of conventional AISI 316L for different temperatures and a strain rate of 1.

#### 8.3.1.2 AISI 316L aditivelly manufactured

Figures 8.7 and 8.8 show the flow stress curves of the aditivelly manufactured AISI316L, as a function of strain, for different temperatures and strain-rates. These curves were plotted based on the flow stress curve of the horizontal AM specimen (see Figure 6.2.6), obtained from the compression tests, correspondent to a strain rate of 1 and a temperature of 20°C. The first term of the Johnson-Cook material constitutive model parameters of this curve are as follows:

- A=507.3 MPa, the initial yield strength;
- B=1076.5 MPa, effect of strain hardening;
- n=0.64, effect of strain hardening.

Considering that only a quasi-static compression test was conducted, and that for the simulation it is necessary to define the flow stress as a function of various strain rates and temperatures, the approach adopted was as follows; for each strain considered, to the stresses obtained through experimental testing (corresponding to a strain rate of 1 and T=20°C), was incremented an amount of stress equal to the increment between flow stress curves of different strain rates, found for the conventional material. For the flow stress curves as a function of temperature, the plotting of the curves for the AM material followed the same approach; for each strain a decrement of stress was applied to the quasi-static flow stress curve, equal to that verified for the conventional material. Whereas for the thermal and elastic properties, namely thermal conductivity, heat capacity and Young modulus, these were defined as a function of temperature with the same data existent in the software for the conventional material. Although this is not ideal, due to the inherent differences between the two materials, it was found to be a good approximation to deal with the lack of data for the AM 316L.

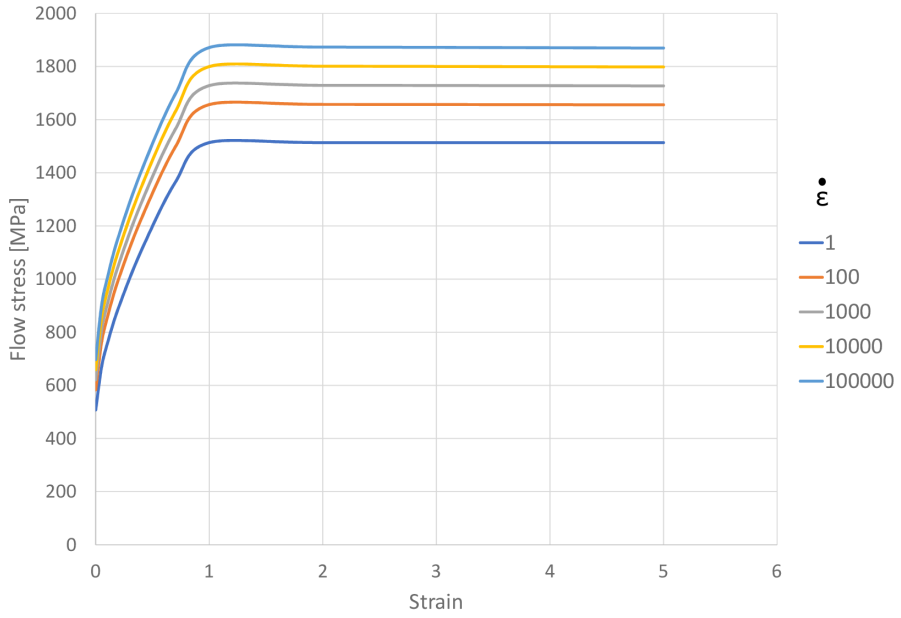


Figure 8.7: Flow stress curves of AM AISI 316L for different stain rates and a temperature of 20°C.

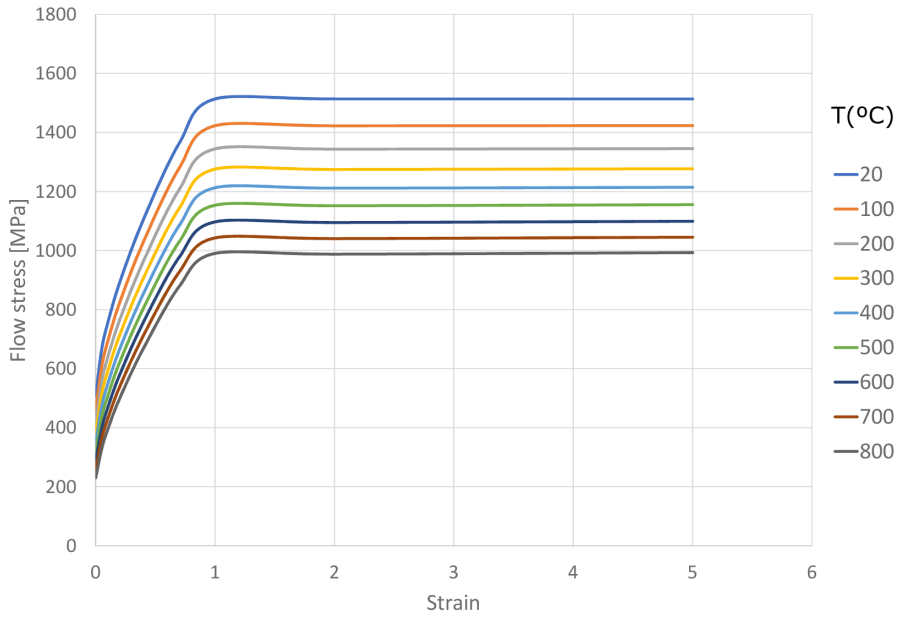


Figure 8.8: Flow stress curves of conventional AISI 316L for different temperatures and a strain rate of 1.

### 8.3.2 Process parameters

The metal cutting simulations, for both the AM and conventional material, were conducted with a cutting speed of 20 m/min for two different feed rates, 0.05 and 0.20 mm/rev. Concerning the cutting tool, the material and geometry were chosen based on the workpiece material (AISI316L); a tungsten carbide (WC) tool with a clearance angle of 7° and two different rake angles, 5° and 12° (refer to Fig. 8.4). These parameters are expressed in Table 8.2.

Table 8.2: Orthogonal cutting simulation parameters.

| Cutting speed [m/min] | Clearance angle ($\theta_c$) | Rake angle ($\alpha$) | Feed rate [mm/rev] |
|---|---|---|---|
| 20 | 7° | 5° | 0.05<br>0.20 |
| | | 12° | 0.05<br>0.20 |

## 8.4 Results

### 8.4.1 Load results

The load results from the Deform$^{TM}$simulations, for both AM and conventional AISI 316L, are presented in Figure 8.9, according to the simulation time. Two distinct zones can be observed in these graphics; the first depicts the initial stage of chip formation, characterized by higher loads, and the second, where the load attains a stable force plateau, represents steady state conditions of chip formation. For the subsequent analysis, the average load for each simulation was calculated from the steady state represented in these graphics.

Figure 8.10 shows the average load results, per mm of thickness of the workpiece (chip width), for both AM and conventional material. For both rake angles tested, an increase in feed rate results in an increase in the cutting force for both materials, as was expected. As for the influence of the rake angle on the cutting force, an increase of a positive rake angle should result in lower cutting forces, as discussed in Section 3.6, which is verified for all cases, except for the conventional material when cut with a feed rate of 0.05mm/rev. Overall the AM material requires higher cutting forces, resulting from its higher yield stresses under all conditions, temperature and strain rate.

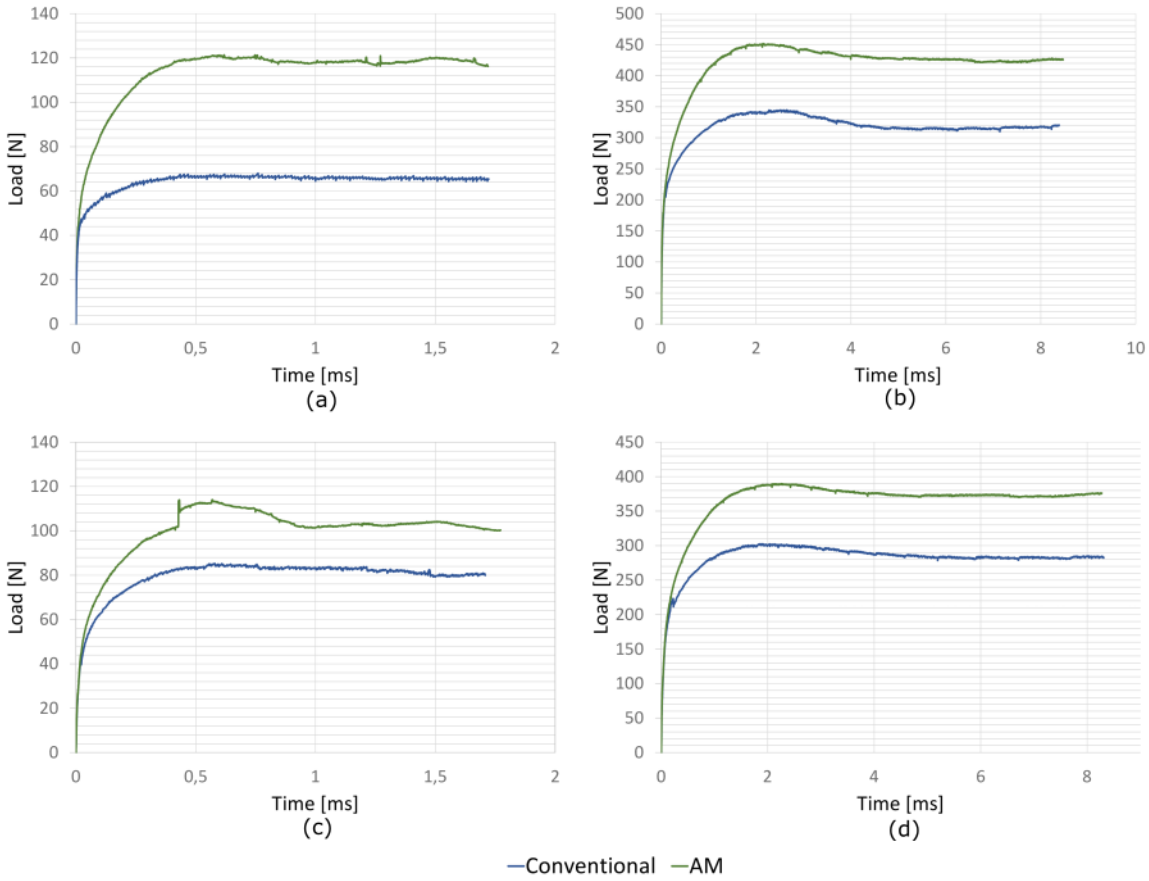


Figure 8.9: Load as a function of time for both AM and conventional 316L: (a) $\alpha$=5° and $f$=0.05mm/rev; (b) $\alpha$=5° and $f$=0.20mm/rev; (c) $\alpha$=12° and $f$=0.05mm/rev; (d) $\alpha$=12° and $f$=0.20mm/rev.

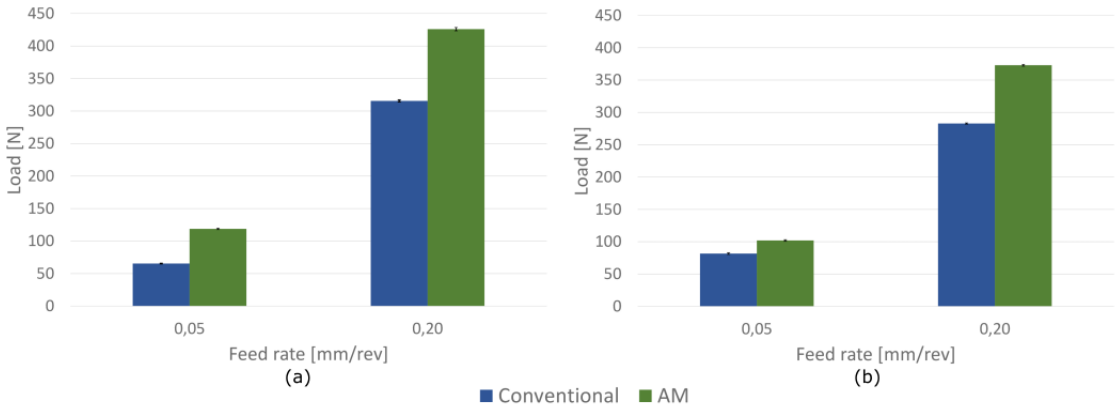


Figure 8.10: Evolution of the average load as a function of feed rate, for both AM and conventional 316L: (a) $\alpha$=5°; (b) $\alpha$=12°.

### 8.4.2 Chip formation

Figures 8.11 and 8.12 show the chip geometry of the conventional and AM AISI316L, respectively, for the simulations with distinct rake angles and feed rates. Concerning the effects of the rake angle on the chip geometry, it is noticeable that an increase in this angle results in a decreased chip thickness, as can be observed for the AM material in Fig. 8.12 from (a) to (b) and from (b) to (c), and also for the conventional material in Fig. 8.4 (b) to (d). As for the influence of feed rate on the chip formation, a lower effective stress can be observed for higher feed rates, for both materials and rake angles.

Contrary to what was found in the experimental turning operations, these simulations did not result in serrated chip formation, which is related to the absence of a damaged model in the simulations. Several authors [57] have simulated adiabatic shearing and serrated chip formation using Lagrangian analysis by employing a damage criteria.

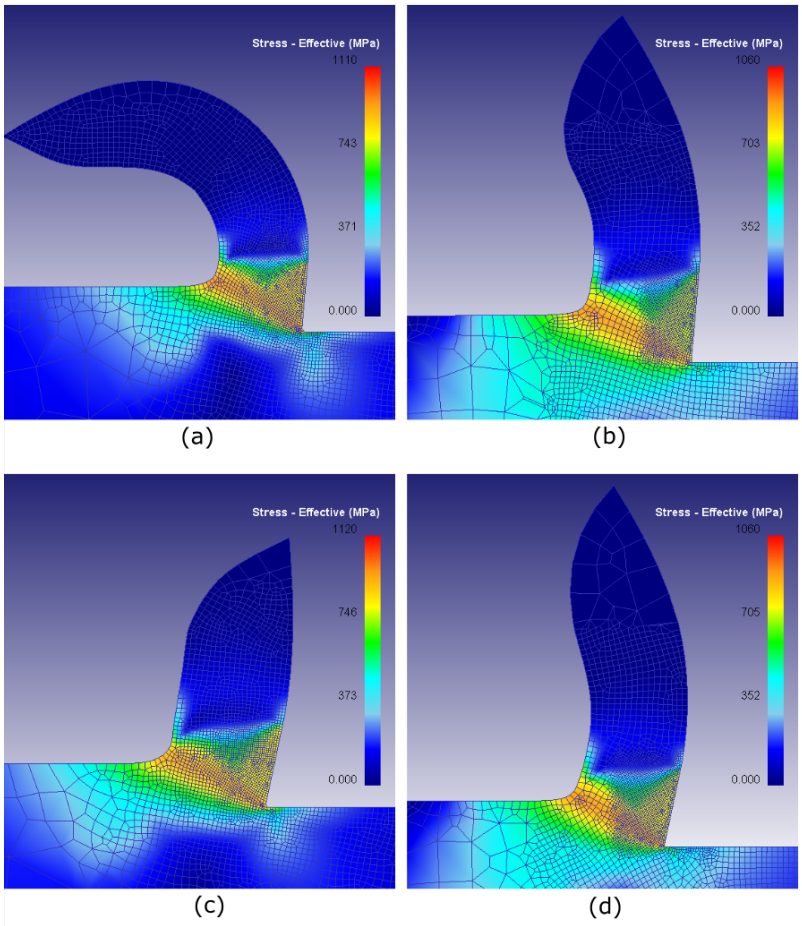


Figure 8.11: Chip geometry of the conventional 316L, with the effective stress distribution, for $v_c$=20m/min and $\theta_c$=7°: (a) $\alpha$=5° and $f$=0.05mm/rev; (b) $\alpha$=5° and $f$=0.20mm/rev; (c) $\alpha$=12° and $f$=0.05mm/rev; (d) $\alpha$=12° and $f$=0.20mm/rev.

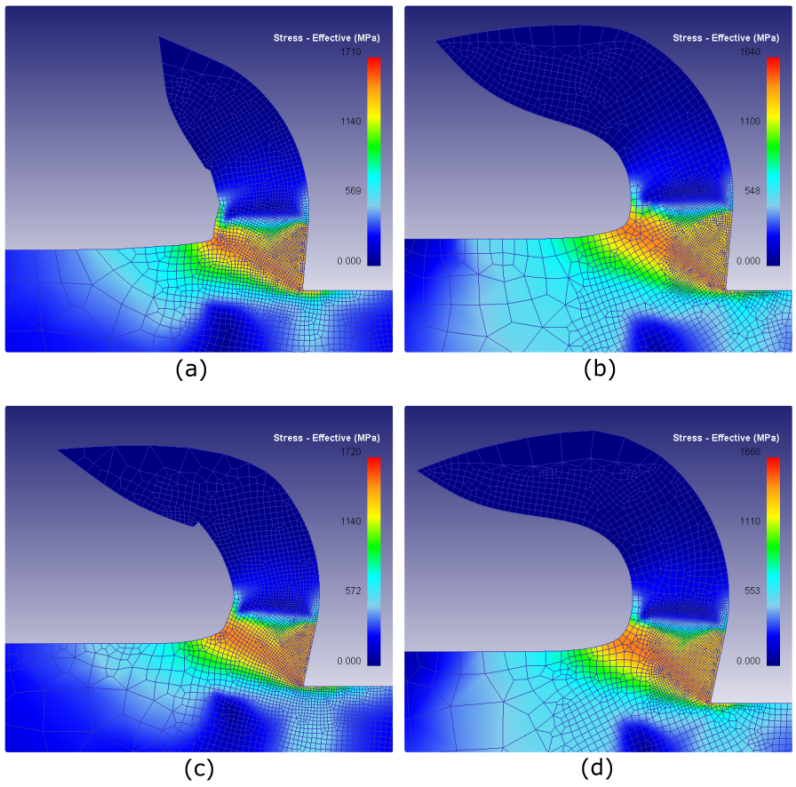


Figure 8.12: Chip geometry of the AM 316L, with the effective stress distribution, for $v_c$=20m/min and $\theta_c$=7°: (a) $\alpha$=5° and $f$=0.05mm/rev; (b) $\alpha$=5° and $f$=0.20mm/rev; (c) $\alpha$=12° and $f$=0.05mm/rev; (d) $\alpha$=12° and $f$=0.20mm/rev.

# Chapter 9

# Conclusions and future work

## 9.1 Conclusions

In this section, the conclusions drawn from the experimental procedures, in terms of material characterization, machining power and cutting forces, chip formation and surface finish are presented, as well as preliminary conclusions derived from the 2D metal cutting simulations.

### 9.1.1 Material characterization

- The flow stress curves revealed a higher yield strength for the AM 316L compared to the conventional material. Furthermore, a higher yield strength is achieved in a direction transverse to the building direction (horizontal AM specimen, XY plane) compared to that of the building direction (vertical AM specimen, Z direction).

### 9.1.2 Machining power and cutting forces

- The cutting forces are highly dependent on depth of cut and feed rate, as expected. An increase in depth of cut and/or feed rate results in a significant increase of the main cutting force for both AM and conventional AISI 316L materials.

- For the range of parameters tested, the main cutting force is not highly influenced by the cutting speed, in the range of tested speeds between 55 and 118 m/min. Revealing, however, a decrease of this force component with an increase in cutting speed for the DCMW cutting insert, for both materials.

- The DCMW cutting insert results in higher cutting forces than DCGT insert, for both materials.

- The cutting power shows an approximately linear variation with both depth of cut and feed rate. The DCMW insert results in a higher power consumption compared to the DCGT insert. The power required for cutting the conventional material, in the conditions tested, is either higher or approximately equal to that of the AM material, for both inserts. A

maximum cutting power of 517W was achieved for the conventional material machined with the DCMW insert, for the maximum depth of cut and feed rate tested.

- The specific cutting pressure shows a tendency to become constant for higher depths of cut and feed rates, whereas for finer cutting conditions it shows an exponential growth tendency, reaching a maximum of 10603MPa, for the conventional material machined with DCMW insert for a chip cross sectional area of 0.005mm$^2$.

### 9.1.3 Chip forms

- The type and form of the chips is highly dependent upon depth of cut and feed rate, for both cutting inserts and materials.
- For both inserts and materials, the lowest depth of cut (0.1mm) and feed rate (0.05mm/rev) lead to unfavourable chip formation, either long, snarled or discontinuous chip segments.
- Comparing the AM and conventional 316L, the first allows a wider range of depths of cut (0.3-0.5mm) and feed rates (0.10-0.20mm/rev), for both the DCMW and DCGT inserts, for favourable chip formation: short tubular, spiral or conical chips.

### 9.1.4 Surface finish

- Both DCGT and DCMW inserts reveal wear on the rake face, showing wear in the coating layers, exposing the substrate material, in addition to the formation of build-up edges.
- Surface roughness values are highly sensible to the insert used and the feed rate, resulting in higher average roughness values for the DCMW insert and for the highest feed rate (0.20mm/rev).
- For the same insert, the average surface roughness is higher for the conventional material, for all feed rates, reaching a maximum Ra=3.22$\mu$m for the DCMW insert with a feed rate of 0.20mm/rev.
- Surface analysis of the AM material machined with DCMW insert reveals broken portions of chips embedded into the surface and an oblique waving pattern, for feed rates of 0.10 and 0.05 mm/rev.

### 9.1.5 FEM simulation

- The simulated cutting forces are highly influenced by the feed rate, and in a lower scale by the cutting tool's rake angle; an increase in feed rate increases the cutting force, whereas an increase in positive rake angle results in lower cutting forces.
- For all conditions tested in the two dimensional numerical model, the AM 316L showed higher cutting forces, reaching a maximum of 426N, per millimeter thickness of the workpiece, for 5° rake angle and a feed rate of 0.20mm/rev.

## 9.2 Future works

- Experimentally testing higher cutting speeds in turning operations, other than in the conventional lathe, to enable the establishment of predictive process data in terms of cutting forces, power and specific cutting pressure.
- Process temperature monitoring during turning operations, to infer about its influence on cutting forces and chip formation.
- Further machinability studies on AM 316L, under different machining operations, such as milling or drilling.
- Further studies on the characteristics of surface integrity, such as microhardness, microstructure and phase transformation of AM stainless steel 316L after machining.
- Flow stress characterization of the AM 316L under high strain rates and temperatures, and thermal and elastic characterization over a wide range of temperatures, in order to develop an accurate material constitutive model that simulates the material behaviour in metal cutting.
- Development of a more sophisticated material model for the AM 316L that accounts for stress fields, material recrystalization and microstructural effects. In addition to characterizing the anisotropy of properties inherent to AM.
- Experimental validation on a shaping machine of the two dimensional orthogonal cutting simulations.

# References


[1] Danielle Strong, Michael Kay, Brett Conner, Thomas Wakefield, and Guha Manogharan. Hybrid manufacturing – integrating traditional manufacturers with additive manufacturing (AM) supply chain. 21:159–173. ISSN 2214-8604. doi: 10.1016/j.addma.2018.03.010. URL http://www.sciencedirect.com/science/article/pii/S2214860417305444.

[2] Longyu Zhang, Haiwei Dong, and Abdulmotaleb El Saddik. From 3D Sensing to Printing: A Survey. 12(2):1–23, . ISSN 15516857. doi: 10.1145/2818710. URL http://dl.acm.org/citation.cfm?doid=2837041.2818710.

[3] Ian Gibson, David Rosen, and Brent Stucker. Introduction and Basic Principles. In Ian Gibson, David Rosen, and Brent Stucker, editors, *Additive Manufacturing Technologies: 3D Printing, Rapid Prototyping, and Direct Digital Manufacturing*, pages 1–18. Springer New York. ISBN 978-1-4939-2113-3. doi: 10.1007/978-1-4939-2113-3_1. URL https://doi.org/10.1007/978-1-4939-2113-3_1.

[4] Terry Wholers. Wholers report 2018.

[5] ISO/ASTM 52900:2015. Additive manufacturing — General principles — Terminology. URL https://www.iso.org/obp/ui/#iso:std:iso-astm:52900:ed-1:v1:en.

[6] T. DebRoy, H. L. Wei, J. S. Zuback, T. Mukherjee, J. W. Elmer, J. O. Milewski, A. M. Beese, A. Wilson-Heid, A. De, and W. Zhang. Additive manufacturing of metallic components – Process, structure and properties. 92:112–224. ISSN 0079-6425. doi: 10.1016/j.pmatsci.2017.10.001. URL http://www.sciencedirect.com/science/article/pii/S0079642517301172.

[7] Dirk Herzog, Vanessa Seyda, Eric Wycisk, and Claus Emmelmann. Additive manufacturing of metals. 117:371 – 392. ISSN 1359-6454. doi: https://doi.org/10.1016/j.actamat.2016.07.019. URL http://www.sciencedirect.com/science/article/pii/S1359645416305158.

[8] W. J. Sames, F. A. List, S. Pannala, R. R. Dehoff, and S. S. Babu. The metallurgy and processing science of metal additive manufacturing. 61(5):315–360, . ISSN 0950-6608, 1743-2804. doi: 10.1080/09506608.2015.1116649. URL http://www.tandfonline.com/doi/full/10.1080/09506608.2015.1116649.

[9] Albert Patterson, Sherri Messimer, and Phillip A Farrington. Overhanging Features and the SLM/DMLS Residual Stresses Problem: Review and Future Research Need. doi: 10.3390/technologies5020015.

[10] Nesma T. Aboulkhair, Nicola M. Everitt, Ian Ashcroft, and Chris Tuck. Reducing porosity in AlSi10Mg parts processed by selective laser melting. 1-4:77–86. ISSN 2214-8604. doi: 10.1016/j.addma.2014.08.001. URL http://www.sciencedirect.com/science/article/pii/S2214860414000062.

[11] Haize Galarraga, Diana A. Lados, Ryan R. Dehoff, Michael M. Kirka, and Peeyush Nandwana. Effects of the microstructure and porosity on properties of Ti-6Al-4V ELI alloy fabricated by electron beam melting (EBM). 10:47–57. ISSN 2214-8604. doi: 10.1016/j.addma.2016.02.003. URL http://www.sciencedirect.com/science/article/pii/S2214860416300331.

[12] D. D. Gu, W. Meiners, K. Wissenbach, and R. Poprawe. Laser additive manufacturing of metallic components: Materials, processes and mechanisms. 57(3):133–164, . ISSN 0950-6608. doi: 10.1179/1743280411Y.0000000014. URL https://doi.org/10.1179/1743280411Y.0000000014.

[13] C. Y. Yap, C. K. Chua, Z. L. Dong, Z. H. Liu, D. Q. Zhang, L. E. Loh, and S. L. Sing. Review of selective laser melting: Materials and applications. 2(4):041101. doi: 10.1063/1.4935926. URL https://aip.scitation.org/doi/abs/10.1063/1.4935926.

[14] G. Casalino, S. L. Campanelli, N. Contuzzi, and A. D. Ludovico. Experimental investigation and statistical optimisation of the selective laser melting process of a maraging steel. 65:151–158. ISSN 0030-3992. doi: 10.1016/j.optlastec.2014.07.021. URL http://www.sciencedirect.com/science/article/pii/S0030399214002011.

[15] J. Mazumder, J. Choi, K. Nagarathnam, J. Koch, and D. Hetzner. The direct metal deposition of H13 tool steel for 3-D components. 49(5):55–60. ISSN 1543-1851. doi: 10.1007/BF02914687. URL https://doi.org/10.1007/BF02914687.

[16] Jean-Pierre Kruth and Ben Vandenbroucke. Selective laser melting of biocompatible metals for rapid manufacturing of medical parts. 13(4):196–203. ISSN 1355-2546. doi: 10.1108/13552540710776142. URL https://www.emeraldinsight.com/doi/full/10.1108/13552540710776142.

[17] C. C. Ng, M. M. Savalani, M. L. Lau, and H. C. Man. Microstructure and mechanical properties of selective laser melted magnesium. 257(17):7447–7454. ISSN 0169-4332. doi: 10.1016/j.apsusc.2011.03.004. URL http://www.sciencedirect.com/science/article/pii/S0169433211003576.

[18] Lore Thijs, Maria Luz Montero Sistiaga, Ruben Wauthle, Qingge Xie, Jean-Pierre Kruth, and Jan Van Humbeeck. Strong morphological and crystallographic texture and resulting yield strength anisotropy in selective laser melted tantalum. 61(12):4657–4668. ISSN 1359-6454. doi: 10.1016/j.actamat.2013.04.036. URL http://www.sciencedirect.com/science/article/pii/S1359645413003091.

[19] Mushtaq Khan and Phill Dickens. Selective Laser Melting (SLM) of pure gold. 43(2):114–121. ISSN 2190-7579. doi: 10.1007/BF03214976. URL https://doi.org/10.1007/BF03214976.

[20] C. V. Mikler, V. Chaudhary, T. Borkar, V. Soni, D. Choudhuri, R. V. Ramanujan, and R. Banerjee. Laser additive processing of Ni-Fe-V and Ni-Fe-Mo Permalloys: Microstructure and magnetic properties. 192:9–11. ISSN 0167-577X. doi: 10.1016/j.matlet.

2017.01.059. URL http://www.sciencedirect.com/science/article/pii/S0167577X1730068X.

[21] Yiyu Shen, Yingqi Li, Chen Chen, and Hai-Lung Tsai. 3D printing of large, complex metallic glass structures. 117:213–222. ISSN 0264-1275. doi: 10.1016/j.matdes.2016.12.087. URL http://www.sciencedirect.com/science/article/pii/S0264127516316148.

[22] A. Kirchner, B. Klöden, J. Luft, T. Weißgärber, and B. Kieback. Process window for electron beam melting of Ti-6Al-4V. 58(4):246–249. ISSN 0032-5899. doi: 10.1179/0032589915Z.000000000244. URL https://doi.org/10.1179/0032589915Z.000000000244.

[23] W. J. Sames, F. A. List, S. Pannala, R. R. Dehoff, and S. S. Babu. The metallurgy and processing science of metal additive manufacturing. 61(5):315–360, . ISSN 0950-6608, 1743-2804. doi: 10.1080/09506608.2015.1116649. URL http://www.tandfonline.com/doi/full/10.1080/09506608.2015.1116649.

[24] Oleg D. Neikov. Introduction. In Oleg D. Neikov, Stanislav S. Naboychenko, Irina V. Murashova, Victor G. Gopienko, Irina V. Frishberg, and Dina V. Lotsko, editors, *Handbook of Non-Ferrous Metal Powders*, pages 1–4. Elsevier. ISBN 978-1-85617-422-0. doi: 10.1016/B978-1-85617-422-0.00027-6. URL http://www.sciencedirect.com/science/article/pii/B9781856174220000276.

[25] Anatoliy Popovich and Vadim Sufiiarov. Metal Powder Additive Manufacturing. pages 215–236. ISBN 978-953-51-2480-1 978-953-51-2479-5. doi: 10.5772/63337.

[26] W.J. Sames, Francisco Medina, W.H. Peter, Sudarsanam Babu, and Ryan Dehoff. Effect of Process Control and Powder Quality on Inconel 718 Produced Using Electron Beam Melting. pages 409–423, . doi: 10.1002/9781119016854.ch32.

[27] Hengfeng Gu, Haijun Gong, Deepankar Pal, H Rafi, Thomas Starr, and Brent Stucker. Influences of Energy Density on Porosity and Microstructure of Selective Laser Melted 17-4PH Stainless Steel. .

[28] Noriko Read, Wei Wang, Khamis Essa, and Moataz M. Attallah. Selective laser melting of AlSi10Mg alloy: Process optimisation and mechanical properties development. 65:417–424. ISSN 0261-3069. doi: 10.1016/j.matdes.2014.09.044. URL http://www.sciencedirect.com/science/article/pii/S0261306914007468.

[29] E. Liverani, S. Toschi, L. Ceschini, and A. Fortunato. Effect of selective laser melting (SLM) process parameters on microstructure and mechanical properties of 316L austenitic stainless steel. 249:255–263. ISSN 0924-0136. doi: 10.1016/j.jmatprotec.2017.05.042. URL http://www.sciencedirect.com/science/article/pii/S0924013617302169.

[30] Wayne E. King, Holly D. Barth, Victor M. Castillo, Gilbert F. Gallegos, John W. Gibbs, Douglas E. Hahn, Chandrika Kamath, and Alexander M. Rubenchik. Observation of keyhole-mode laser melting in laser powder-bed fusion additive manufacturing. 214(12):2915–2925. ISSN 0924-0136. doi: 10.1016/j.jmatprotec.2014.06.005. URL http://www.sciencedirect.com/science/article/pii/S0924013614002283.

[31] A. Bauereiß, T. Scharowsky, and C. Körner. Defect generation and propagation mechanism during additive manufacturing by selective beam melting. 214(11):2522–2528. ISSN 0924-0136. doi: 10.1016/j.jmatprotec.2014.05.002. URL http://www.sciencedirect.com/science/article/pii/S0924013614001691.

[32] Dongdong Gu and Yifu Shen. Balling phenomena in direct laser sintering of stainless steel powder: Metallurgical mechanisms and control methods. 30(8):2903–2910. ISSN 0261-3069. doi: 10.1016/j.matdes.2009.01.013. URL http://www.sciencedirect.com/science/article/pii/S0261306909000181.

[33] Giovanni Strano, Liang Hao, Richard M. Everson, and Kenneth E. Evans. Surface roughness analysis, modelling and prediction in selective laser melting. 213(4):589–597. ISSN 0924-0136. doi: 10.1016/j.jmatprotec.2012.11.011. URL http://www.sciencedirect.com/science/article/pii/S0924013612003366.

[34] Luke N. Carter, Moataz M. Attallah, and Roger C. Reed. Laser Powder Bed Fabrication of Nickel-Base Superalloys: Influence of Parameters; Characterisation, Quantification and Mitigation of Cracking. In *Superalloys 2012*, pages 577–586. John Wiley & Sons, Ltd. ISBN 978-1-118-51643-0. doi: 10.1002/9781118516430.ch64. URL https://onlinelibrary.wiley.com/doi/abs/10.1002/9781118516430.ch64.

[35] Leonhard Hitzler, Johann Hirsch, Burkhard Heine, Markus Merkel, Wayne Hall, and Andreas Öchsner. On the Anisotropic Mechanical Properties of Selective Laser-Melted Stainless Steel. 10(10). ISSN 1996-1944. doi: 10.3390/ma10101136.

[36] Xiaoyuan Lou, Michelle A. Othon, and Raul B. Rebak. Corrosion fatigue crack growth of laser additively-manufactured 316L stainless steel in high temperature water. 127: 120–130. ISSN 0010-938X. doi: 10.1016/j.corsci.2017.08.023. URL http://www.sciencedirect.com/science/article/pii/S0010938X1731082X.

[37] Zhi Gang Wang, Yu Sheng Shi, Rui Di Li, Qingsong Wei, and Jin Hui Liu. Manufacturing AISI316L Components via Selective Laser Melting Coupled with Hot Isostatic Pressing. 675-677:853–856. doi: 10.4028/www.scientific.net/MSF.675-677.853.

[38] K. Alrbaey, D. Wimpenny, R. Tosi, W. Manning, and A. Moroz. On Optimization of Surface Roughness of Selective Laser Melted Stainless Steel Parts: A Statistical Study. 23(6):2139–2148. ISSN 1544-1024. doi: 10.1007/s11665-014-0993-9. URL https://doi.org/10.1007/s11665-014-0993-9.

[39] Bartłomiej Wysocki, Joanna Idaszek, Joanna Zdunek, Krzysztof Rożniatowski, Marcin Pisarek, Akiko Yamamoto, and Wojciech Święszkowski. The Influence of Selective Laser Melting (SLM) Process Parameters on In-Vitro Cell Response. 19(6). ISSN 1422-0067. doi: 10.3390/ijms19061619. URL http://www.mdpi.com/1422-0067/19/6/1619.

[40] D. Brown, C. Li, Z. Y. Liu, X. Y. Fang, and Y. B. Guo. Surface integrity of Inconel 718 by hybrid selective laser melting and milling. 13(1):26–31. ISSN 1745-2759. doi: 10.1080/17452759.2017.1392681. URL https://doi.org/10.1080/17452759.2017.1392681.

[41] Daniel Eisenbarth, Fabian Soffel, and Konrad Wegener. Effects of direct metal deposition combined with intermediate and final milling on part distortion. 14(2):130–134. ISSN 1745-2759. doi: 10.1080/17452759.2018.1532799. URL https://doi.org/10.1080/17452759.2018.1532799.

[42] Olusola Oyelola, Peter Crawforth, Rachid M'Saoubi, and Adam T. Clare. Machining of Additively Manufactured Parts: Implications for Surface Integrity. 45:119–122. ISSN 2212-8271. doi: 10.1016/j.procir.2016.02.066. URL http://www.sciencedirect.com/science/article/pii/S2212827116003486.

[43] Yusuf Kaynak and Ozhan Kitay. Porosity, Surface Quality, Microhardness and Microstructure of Selective Laser Melted 316L Stainless Steel Resulting from Finish Machining. 2(2): 36. doi: 10.3390/jmmp2020036. URL https://www.mdpi.com/2504-4494/2/2/36.

[44] Yusuf Kaynak and Özhan Kıtay. The effect of post-processing operations on surface characteristics of 316L stainless steel produced by selective laser melting. in press. doi: 10.1016/j.addma.2018.12.021.

[45] F. Klocke. Machining and Machinability. In K. H. Jürgen Buschow, Robert W. Cahn, Merton C. Flemings, Bernhard Ilschner, Edward J. Kramer, Subhash Mahajan, and Patrick Veyssière, editors, *Encyclopedia of Materials: Science and Technology*, pages 4683–4688. Elsevier, . ISBN 978-0-08-043152-9. doi: 10.1016/B0-08-043152-6/00816-0. URL http://www.sciencedirect.com/science/article/pii/B0080431526008160.

[46] Ahmed M. Karim. Fundamentals of Modern Manufacturing: Materials, Processes, and Systems 5th Edition - by (Mikell P. Groover). URL https://www.academia.edu/35100247/Fundamentals_of_Modern_Manufacturing_Materials_Processes_and_Systems_5th_Edition_-_by_Mikell_P._Groover_.

[47] P. N. Rao. *MANUFACTURING TECHNOLOGY VOL-II 2E*. Tata McGraw-Hill Education. ISBN 978-0-07-008769-9.

[48] Cenk Kılıçaslan. Modelling of metal cutting by finite element method.

[49] Hans Kurt Toenshoff. Cutting, Fundamentals. In Luc Laperrière and Gunther Reinhart, editors, *CIRP Encyclopedia of Production Engineering*, pages 345–357. Springer Berlin Heidelberg. ISBN 978-3-642-20617-7. doi: 10.1007/978-3-642-20617-7_6633. URL https://doi.org/10.1007/978-3-642-20617-7_6633.

[50] Mridul Singal. *Fundamentals of Machining and Machine Tools*. I. K. International Pvt Ltd. ISBN 978-81-89866-66-2.

[51] Hans Kurt Tönshoff and Berend Denkena. *Chip Formation*, pages 21–36. Springer Berlin Heidelberg, . ISBN 978-3-642-33256-2 978-3-642-33257-9. doi: 10.1007/978-3-642-33257-9_2. URL http://link.springer.com/10.1007/978-3-642-33257-9_2.

[52] Hans Kurt Tönshoff and Berend Denkena. *Chip Control*, pages 37–48. Springer Berlin Heidelberg, . ISBN 978-3-642-33256-2 978-3-642-33257-9. doi: 10.1007/978-3-642-33257-9_3. URL http://link.springer.com/10.1007/978-3-642-33257-9_3.

[53] Hans Kurt Tönshoff and Berend Denkena. Cutting Materials. In Hans Kurt Toenshoff and Berend Denkena, editors, *Basics of Cutting and Abrasive Processes*, Lecture Notes in Production Engineering, pages 159–188. Springer Berlin Heidelberg, . ISBN 978-3-642-33257-9. doi: 10.1007/978-3-642-33257-9_8. URL https://doi.org/10.1007/978-3-642-33257-9_8.

[54] Fritz Klocke. *Manufacturing Processes 1: Cutting*. Springer Science & Business Media, . ISBN 978-3-642-11979-8.

[55] Mitsubishi materials. Mitsubishi C008A Catalog. URL http://www.mitsubishicarbide.com/application/files/6915/1668/5748/catalog_c008b_technical_data.pdf.

[56] Hans Kurt Tönshoff and Berend Denkena. Surface and Subsurface Properties. In Hans Kurt Toenshoff and Berend Denkena, editors, *Basics of Cutting and Abrasive Processes*, Lecture Notes in Production Engineering, pages 349–370. Springer Berlin Heidelberg, . ISBN 978-3-642-33257-9. doi: 10.1007/978-3-642-33257-9_16. URL https://doi.org/10.1007/978-3-642-33257-9_16.

[57] Tugrul Özel. The influence of friction models on finite element simulations of machining. 46(5):518–530. ISSN 0890-6955. doi: 10.1016/j.ijmachtools.2005.07.001. URL http://www.sciencedirect.com/science/article/pii/S0890695505001550.

[58] J. M. Rodríguez, P. Jonsén, and A. Svoboda. Simulation of metal cutting using the particle finite-element method and a physically based plasticity model. 4(1):35–51. ISSN 2196-4386. doi: 10.1007/s40571-016-0120-9. URL https://doi.org/10.1007/s40571-016-0120-9.

[59] P. Lambert. 6 - Sustainability of metals and alloys in construction. In Jamal M. Khatib, editor, *Sustainability of Construction Materials (Second Edition)*, Woodhead Publishing Series in Civil and Structural Engineering, pages 105–128. Woodhead Publishing. ISBN 978-0-08-100995-6. doi: 10.1016/B978-0-08-100370-1.00006-8. URL http://www.sciencedirect.com/science/article/pii/B9780081003701000068.

[60] Zhongji Sun, Xipeng Tan, Shu Beng Tor, and Wai Yee Yeong. Selective laser melting of stainless steel 316L with low porosity and high build rates. 104:197–204. ISSN 0264-1275. doi: 10.1016/j.matdes.2016.05.035. URL http://www.sciencedirect.com/science/article/pii/S0264127516306372.

[61] K. Saeidi, X. Gao, Y. Zhong, and Z. J. Shen. Hardened austenite steel with columnar subgrain structure formed by laser melting. 625:221–229. ISSN 0921-5093. doi: 10.1016/j.msea.2014.12.018. URL http://www.sciencedirect.com/science/article/pii/S0921509314015056.

[62] Yuan Zhong, Leifeng Liu, Stefan Wikman, Daqing Cui, and Zhijian Shen. Intragranular cellular segregation network structure strengthening 316L stainless steel prepared by selective laser melting. 470:170–178. ISSN 0022-3115. doi: 10.1016/j.jnucmat.2015.12.034. URL http://www.sciencedirect.com/science/article/pii/S0022311515304037.

[63] Tuan D. Ngo, Alireza Kashani, Gabriele Imbalzano, Kate T.Q. Nguyen, and David Hui. Additive manufacturing (3D printing): A review of materials, methods, applications and challenges. 143:172–196. ISSN 13598368. doi: 10.1016/j.compositesb.2018.02.012. URL https://linkinghub.elsevier.com/retrieve/pii/S1359836817342944.

[64] Bo Song, Xiao Zhao, Shuai Li, Changjun Han, Qingsong Wei, Shifeng Wen, Jie Liu, and Yusheng Shi. Differences in microstructure and properties between selective laser melting and traditional manufacturing for fabrication of metal parts: A review. 10(2):111–125. ISSN 2095-0241. doi: 10.1007/s11465-015-0341-2. URL https://doi.org/10.1007/s11465-015-0341-2.

[65] Dieter Lung. Machinability of High-Alloyed Steel and Stainless Steel. In Luc Laperrière and Gunther Reinhart, editors, *CIRP Encyclopedia of Production Engineering*, pages 787–791. Springer Berlin Heidelberg. ISBN 978-3-642-20617-7. doi: 10.1007/978-3-642-20617-7_6699. URL https://doi.org/10.1007/978-3-642-20617-7_6699.

[66] Jyoti Suryawanshi, K. G. Prashanth, and U. Ramamurty. Mechanical behavior of selective laser melted 316L stainless steel. 696:113–121. ISSN 0921-5093. doi: 10.1016/j.msea.2017.04.058. URL http://www.sciencedirect.com/science/article/pii/S0921509317305105.

[67] Zbigniew Brytan. Comparison of Vacuum Sintered and Selective Laser Melted Steel AISI 316L. 62. doi: 10.1515/amm-2017-0314.

[68] Baicheng Zhang, Lucas Dembinski, and Christian Coddet. The study of the laser parameters and environment variables effect on mechanical properties of high compact parts elaborated by selective laser melting 316L powder. 584:21–31, . ISSN 0921-5093. doi: 10.1016/j.msea.2013.06.055. URL http://www.sciencedirect.com/science/article/pii/S0921509313007065.

[69] Tomasz Kurzynowski, Konrad Gruber, Wojciech Stopyra, Bogumiła Kuźnicka, and Edward Chlebus. Correlation between process parameters, microstructure and properties of 316 L stainless steel processed by selective laser melting. 718:64–73. ISSN 0921-5093. doi: 10.1016/j.msea.2018.01.103. URL http://www.sciencedirect.com/science/article/pii/S0921509318301473.

[70] Wen Shifeng, Li Shuai, Wei Qingsong, Chunze Yan, Zhang Sheng, and Shi Yusheng. Effect of molten pool boundaries on the mechanical properties of selective laser melting parts. 214 (11):2660–2667. ISSN 0924-0136. doi: 10.1016/j.jmatprotec.2014.06.002. URL http://www.sciencedirect.com/science/article/pii/S0924013614002258.

[71] Junjie Chen, Qian Xiao, Zhanpeng Lu, Xiangkun Ru, Guangdong Han, Yongwu Tian, and Tetsuo Shoji. The Effects of Prior-Deformation on Anodic Dissolution Kinetics and Pitting Behavior of 316L Stainless Steel. 11:1395–1415.

[72] Woei-Shyan Lee, Tao-Hsing Chen, Chi-Feng Lin, and Wen-Zhen Luo. Dynamic Mechanical Response of Biomedical 316L Stainless Steel as Function of Strain Rate and Temperature. 2011. ISSN 1565-3633. doi: 10.1155/2011/173782. URL https://www.ncbi.nlm.nih.gov/pmc/articles/PMC3246303/.

[73] G. Miranda, S. Faria, F. Bartolomeu, E. Pinto, S. Madeira, A. Mateus, P. Carreira, N. Alves, F. S. Silva, and O. Carvalho. Predictive models for physical and mechanical properties of 316L stainless steel produced by selective laser melting. 657:43–56. ISSN 0921-5093. doi: 10.1016/j.msea.2016.01.028. URL http://www.sciencedirect.com/science/article/pii/S0921509316300272.

[74] Chunlei Qiu, Mohammed Al Kindi, Aiman Salim Aladawi, and Issa Al Hatmi. A comprehensive study on microstructure and tensile behaviour of a selectively laser melted stainless steel. 8(1):7785. ISSN 2045-2322. doi: 10.1038/s41598-018-26136-7. URL https://www.nature.com/articles/s41598-018-26136-7.

[75] Todd M. Mower and Michael J. Long. Mechanical behavior of additive manufactured, powder-bed laser-fused materials. 651:198–213. ISSN 0921-5093. doi: 10.1016/j.msea.2015.10.068. URL http://www.sciencedirect.com/science/article/pii/S092150931530530X.

[76] G. T. Gray Iii, V. Livescu, P. A. Rigg, C. P. Trujillo, C. M. Cady, S. R. Chen, J. S. Carpenter, T. J. Lienert, and S. Fensin. Structure/property (constitutive

and dynamic strength/damage) characterization of additively manufactured 316L SS. 94:02006. ISSN 2100-014X. doi: 10.1051/epjconf/20159402006. URL https://www.epj-conferences.org/articles/epjconf/abs/2015/13/epjconf-dymat2015_02006/epjconf-dymat2015_02006.html.

[77] Süleyman Yaldız and Faruk Ünsaçar. A dynamometer design for measurement the cutting forces on turning. 39(1):80–89. ISSN 02632241. doi: 10.1016/j.measurement.2005.07.008. URL https://linkinghub.elsevier.com/retrieve/pii/S0263224105000801.

[78] Grzegorz Struzikiewicz, Wojciech Zębala, Andrzej Matras, Magdalena Machno, Łukasz Ślusarczyk, Sebastian Hichert, and Fabian Laufer. Turning Research of Additive Laser Molten Stainless Steel 316L Obtained by 3D Printing. 12(1). ISSN 1996-1944. doi: 10.3390/ma12010182. URL https://www.ncbi.nlm.nih.gov/pmc/articles/PMC6337284/.

[79] Hong Wu and Sandy To. Serrated chip formation and their adiabatic analysis by using the constitutive model of titanium alloy in high speed cutting. 629:368–373. doi: 10.1016/j.jallcom.2014.12.230.

[80] Juan Rodríguez Prieto, J M. Carbonell, Juan Cante, Javier Oliver, and P Jonsén. Generation of segmental chips in metal cutting modeled with the PFEM. 61. doi: 10.1007/s00466-017-1442-z.

[81] Antonio Simón Mata, Alex Bataller Torras, Juan Antonio Cabrera Carrillo, Francisco Ezquerro Juanco, Antonio Jesús Guerra Fernández, Fernando Nadal Martínez, and Antonio Ortiz Fernández. Kinematic Analysis of Mechanisms. Relative Velocity and Acceleration. Instant Centers of Rotation. In Antonio Simón Mata, Alex Bataller Torras, Juan Antonio Cabrera Carrillo, Francisco Ezquerro Juanco, Antonio Jesús Guerra Fernández, Fernando Nadal Martínez, and Antonio Ortiz Fernández, editors, *Fundamentals of Machine Theory and Mechanisms*, Mechanisms and Machine Science, pages 21–110. Springer International Publishing. ISBN 978-3-319-31970-4. doi: 10.1007/978-3-319-31970-4_2. URL https://doi.org/10.1007/978-3-319-31970-4_2.

[82] Katarina Monkova, Peter Monka, Sergej Hloch, and Jan Valícek. Kinematic analysis of quick-return mechanism in three various approaches. 18:295–299.

[83] Halil Bil. Simulation of orthogonal metal cutting by finite element analysis.

# Appendix A

# Methods for powder production

Table A.1: Methods for metal powder production [24].

| Method of production | Processing character | Material | Characteristic of powder particles | |
|---|---|---|---|---|
| | | | Median mass diameter ($d_m$) (µm) | Shape |
| *Mechanical methods* | | | | |
| Comminution of solids | Machining | Brass, bronze, Mg, Al, Cu | $3 \cdot 10^3$–$10^3$ | Chips |
| | Hammer mills | Sinter cakes | $5 \cdot 10^3$–50 | Angular, irregular |
| | Ball and rod mills, self-grinding | Bronze, Al, Ag, Ti, Ni, Cr | $5 \cdot 10^3$–10 | Scaly, flake |
| | Mill rolls and bowl mills | The same | $10^4$–20 | Irregular, scaly |
| | Vibratory mills | Metals, alloys | 10–0.2 | Scaly |
| | Medium agitating mills (attritors) | Metals, alloys | 15–0.1<br>40–1.0 | Scaly<br>Irregular |
| | Jet mills | Mo, Be, tungsten alloys | <40 | Flaked |
| Atomization of melts | Water granulation | Metals, alloys | $5 \cdot 10^3$–$10^3$ | Spherical, irregular |
| | Water atomization | Metals, alloys | $2 \cdot 10^3$–1.0 | Irregular |
| | Gas atomization | Metals, alloys | 500–10 | Spherical, irregular |
| | Centrifugal atomization | Al alloys, Be alloys, Mg, Mo, Ni alloys | 150–50 | Spherical, irregular |
| | Rotating electrode process | Ti alloys, Ni alloys | 300–150 | Spheroidal Irregular, angular |
| *Chemical and electrolytic methods* | | | | |
| Reduction metal oxides | Oxide reduction by reducing atmospheres | Ni, Co, Cu, W, Mo | 300–20 | Spongy, granular, (conglomerates) |
| | Precipitation from solution | Ti, W, Precious metals | 100 nano-size | Spongy, irregular, angular |
| | Hydrogenation, dehydrogenation | Ti, Zr, Hf | 200–20 | Irregular, angular |
| | Hydrometallurgical processing in leach autoclaves | Ni, Co, Cu, Precious metals | 70–10 | Spongy, granular, briquettes |
| | Metallothermy | Tantalum, niobium, magnesium, titanium, thorium, zirconium, vanadium | 300–20 | The same |
| | Carbothermy | Aluminum, magnesium, niobium, tungsten | 400–20 | Spongy |
| | Carbonyl process | Ni, Co, W, Mo | 300–0.1 | Spongy, acicular |
| Electrolysis | Electrolysis of aqueous solutions | Copper, tin, lead, zinc, nickel | 400–ultrafine | Dendritic |
| | Electrolysis from melts | Aluminum, magnesium, titanium, tantalum, niobium, vanadium, zirconium | 400–10 | Dendritic |
| *Physical-chemical methods* | | | | |
| Gas phase precipitation | Evaporation and condensation | Zn, Mg, Ti, Ag, Cd, Bi | Ultrafine, Nano-size | Conglomerate of particles, clusters |
| *Other methods* | | | | |
| Mechanical alloying | Ball milling | Metals, alloys | Ultrafine, Nano-size | Agglomerate of particles, clusters |
| Spray granulation | Fluidized bed spray granulator | Al, Co, pyrophoric rare earths | $5 \cdot 10^3$–$10^3$ | Spherical |

# Appendix B

# Codes for the turning experiments

Table B.1: Code names adopted for the turning experiments.

| $d_0$[mm] | n[rpm] | $v_c$ | Cutting tool | $f$[mm/rev] | $a_p$[mm] | t[s] | Code |
|---|---|---|---|---|---|---|---|
| 15 | 2500 | 118 | T1 | 0.20 | 0.5 | 2.4 | V1T1f3a1 |
| 14 | 2500 | 110 | T1 | 0.20 | 0.3 | 2.4 | V1T1f3a2 |
| 13.4 | 2500 | 105 | T1 | 0.20 | 0.1 | 2.4 | V1T1f3a3 |
| 13.2 | 2500 | 104 | T1 | 0.10 | 0.5 | 4.8 | V1T1f2a1 |
| 12.2 | 2500 | 96 | T1 | 0.10 | 0.3 | 4.8 | V1T1f2a2 |
| 11.6 | 2500 | 91 | T1 | 0.10 | 0.1 | 4.8 | V1T1f2a3 |
| 11.4 | 2500 | 90 | T1 | 0.05 | 0.5 | 9.6 | V1T1f1a1 |
| 10.4 | 2500 | 82 | T1 | 0.05 | 0.3 | 9.6 | V1T1f1a2 |
| 9.8 | 2500 | 77 | T1 | 0.05 | 0.1 | 9.6 | V1T1f1a3 |
| 15 | 1800 | 118 | T1 | 0.20 | 0.5 | 2.4 | V2T1f3a1 |
| 14 | 1800 | 110 | T1 | 0.20 | 0.3 | 2.4 | V2T1f3a2 |
| 13.4 | 1800 | 105 | T1 | 0.20 | 0.1 | 2.4 | V1T1f3a3 |
| 13.2 | 1800 | 104 | T1 | 0.10 | 0.5 | 4.8 | V2T1f2a1 |
| 12.2 | 1800 | 96 | T1 | 0.10 | 0.3 | 4.8 | V2T1f2a2 |
| 11.6 | 1800 | 91 | T1 | 0.10 | 0.1 | 4.8 | V2T1f2a3 |
| 11.4 | 1800 | 90 | T1 | 0.05 | 0.5 | 9.6 | V2T1f1a1 |
| 10.4 | 1800 | 82 | T1 | 0.05 | 0.3 | 9.6 | V2T1f1a2 |
| 9.8 | 1800 | 77 | T1 | 0.05 | 0.1 | 9.6 | V2T1f1a3 |
| 15 | 2500 | 118 | T1 | 0.20 | 0.5 | 2.4 | V1T2f3a1 |
| 14 | 2500 | 110 | T1 | 0.20 | 0.3 | 2.4 | V1T2f3a2 |
| 13.4 | 2500 | 105 | T1 | 0.20 | 0.1 | 2.4 | V1T2f3a3 |
| 13.2 | 2500 | 104 | T1 | 0.10 | 0.5 | 4.8 | V1T2f2a1 |
| 12.2 | 2500 | 96 | T1 | 0.10 | 0.3 | 4.8 | V1T2f2a2 |
| 11.6 | 2500 | 91 | T1 | 0.10 | 0.1 | 4.8 | V1T2f2a3 |
| 11.4 | 2500 | 90 | T1 | 0.05 | 0.5 | 9.6 | V1T2f1a1 |
| 10.4 | 2500 | 82 | T1 | 0.05 | 0.3 | 9.6 | V1T2f1a2 |
| 9.8 | 2500 | 77 | T1 | 0.05 | 0.1 | 9.6 | V1T2f1a3 |
| 15 | 1800 | 118 | T1 | 0.20 | 0.5 | 2.4 | V2T2f3a1 |
| 14 | 1800 | 110 | T1 | 0.20 | 0.3 | 2.4 | V2T1f3a2 |
| 13.4 | 1800 | 105 | T1 | 0.20 | 0.1 | 2.4 | V1T1f3a3 |
| 13.2 | 1800 | 104 | T1 | 0.10 | 0.5 | 4.8 | V2T2f2a1 |
| 12.2 | 1800 | 96 | T1 | 0.10 | 0.3 | 4.8 | V2T2f2a2 |
| 11.6 | 1800 | 91 | T1 | 0.10 | 0.1 | 4.8 | V2T2f2a3 |
| 11.4 | 1800 | 90 | T1 | 0.05 | 0.5 | 9.6 | V2T2f1a1 |
| 10.4 | 1800 | 82 | T1 | 0.05 | 0.3 | 9.6 | V2T2f1a2 |
| 9.8 | 1800 | 77 | T1 | 0.05 | 0.1 | 9.6 | V2T2f1a3 |

# Appendix C

# Average load values of the turning experiments

Table C.1: Average load values of the turning experiments.

| Code | Conventional | | | AM | | |
|---|---|---|---|---|---|---|
| | $F_f$ [N] | $F_p$ [N] | $F_c$ [N] | $F_f$ [N] | $F_p$ [N] | $F_c$ [N] |
| V1T1f3a1 | 95.8 | 96.8 | 222.7 | 85.6 | 103.4 | 212.7 |
| V1T1f3a2 | 61.2 | 116.0 | 145.5 | 49.4 | 96.2 | 146.3 |
| V1T1f3a3 | 18.6 | 71.6 | 67.9 | 10.9 | 64.2 | 56.8 |
| V1T1f2a1 | 94.9 | 80.9 | 146.0 | 86.6 | 74.2 | 145.8 |
| V1T1f2a2 | 50.7 | 79.2 | 94.4 | 47.8 | 73.2 | 94.9 |
| V1T1f2a3 | 10.6 | 48.0 | 42.0 | 12.9 | 48.4 | 42.4 |
| V1T1f1a1 | 83.8 | 58.7 | 96.4 | 70.4 | 50.5 | 94.3 |
| V1T1f1a2 | 44.3 | 57.7 | 71.3 | 37.3 | 50.0 | 60.8 |
| V1T1f1a3 | 9.7 | 36.1 | 29.3 | 10.9 | 34.3 | 28.6 |
| V2T1f3a1 | 113.5 | 119.7 | 248.6 | 102.5 | 108.1 | 233.0 |
| V2T1f3a2 | 57.2 | 108.1 | 147.8 | 47.1 | 91.1 | 142.0 |
| V1T1f3a3 | 15.0 | 64.4 | 64.6 | 13.2 | 59.2 | 66.3 |
| V2T1f2a1 | 111.4 | 70.9 | 159.5 | 97.0 | 67.6 | 150.4 |
| V2T1f2a2 | 46.2 | 68.5 | 86.8 | 43.4 | 66.9 | 89.2 |
| V2T1f2a3 | 15.0 | 48.5 | 43.4 | 11.4 | 40.3 | 40.5 |
| V2T1f1a1 | 80.5 | 51.0 | 100.5 | 69.4 | 47.5 | 94.5 |
| V2T1f1a2 | 36.4 | 49.9 | 59.7 | 33.0 | 45.2 | 57.2 |
| V2T1f1a3 | 9.1 | 31.4 | 25.5 | 27.9 | 14.9 | 21.4 |
| V1T2f3a1 | 128.5 | 119.2 | 263.4 | 121.8 | 139.2 | 245.8 |
| V1T2f3a2 | 69.5 | 136.1 | 159.9 | 70.0 | 136.0 | 166.5 |
| V1T2f3a3 | 21.8 | 108.1 | 78.3 | 20.8 | 101.4 | 71.9 |
| V1T2f2a1 | 144.4 | 119.9 | 173.4 | 124.1 | 110.7 | 165.8 |
| V1T2f2a2 | 87.8 | 121.9 | 118.3 | 65.2 | 120.1 | 105.5 |
| V1T2f2a3 | 25.1 | 98.8 | 54.9 | 26.2 | 92.7 | 52.9 |
| V1T2f1a1 | 130.9 | 104.7 | 120.8 | 112.9 | 100.8 | 112.2 |
| V1T2f1a2 | 82.5 | 101.7 | 89.3 | 75.4 | 96.8 | 80.9 |
| V1T2f1a3 | 13.5 | 79.1 | 53.0 | 31.8 | 74.1 | 42.3 |
| V2T2f3a1 | 198.0 | 221.9 | 303.6 | 187.8 | 232.5 | 298.8 |
| V2T2f3a2 | 104.1 | 213.5 | 201.9 | 105.9 | 212.5 | 197.8 |
| V2T2f3a3 | 32.2 | 154.1 | 94.5 | 27.7 | 144.4 | 87.8 |
| V2T2f2a1 | 183.2 | 151.1 | 201.8 | 204.9 | 157.1 | 202.2 |
| V2T2f2a2 | 102.8 | 143.4 | 137.5 | 130.4 | 152.1 | 147.6 |
| V2T2f2a3 | 26.1 | 105.6 | 64.5 | 31.8 | 106.4 | 64.9 |
| V2T2f1a1 | 135.0 | 111.5 | 135.9 | 216.1 | 119.9 | 162.5 |
| V2T2f1a2 | 96.3 | 99.6 | 105.1 | 130.8 | 110.9 | 111.8 |
| V2T2f1a3 | 27.8 | 68.9 | 45.3 | 78.9 | 36.0 | 31.0 |

# Appendix D

# Energy-dispersive X-ray spectroscopy

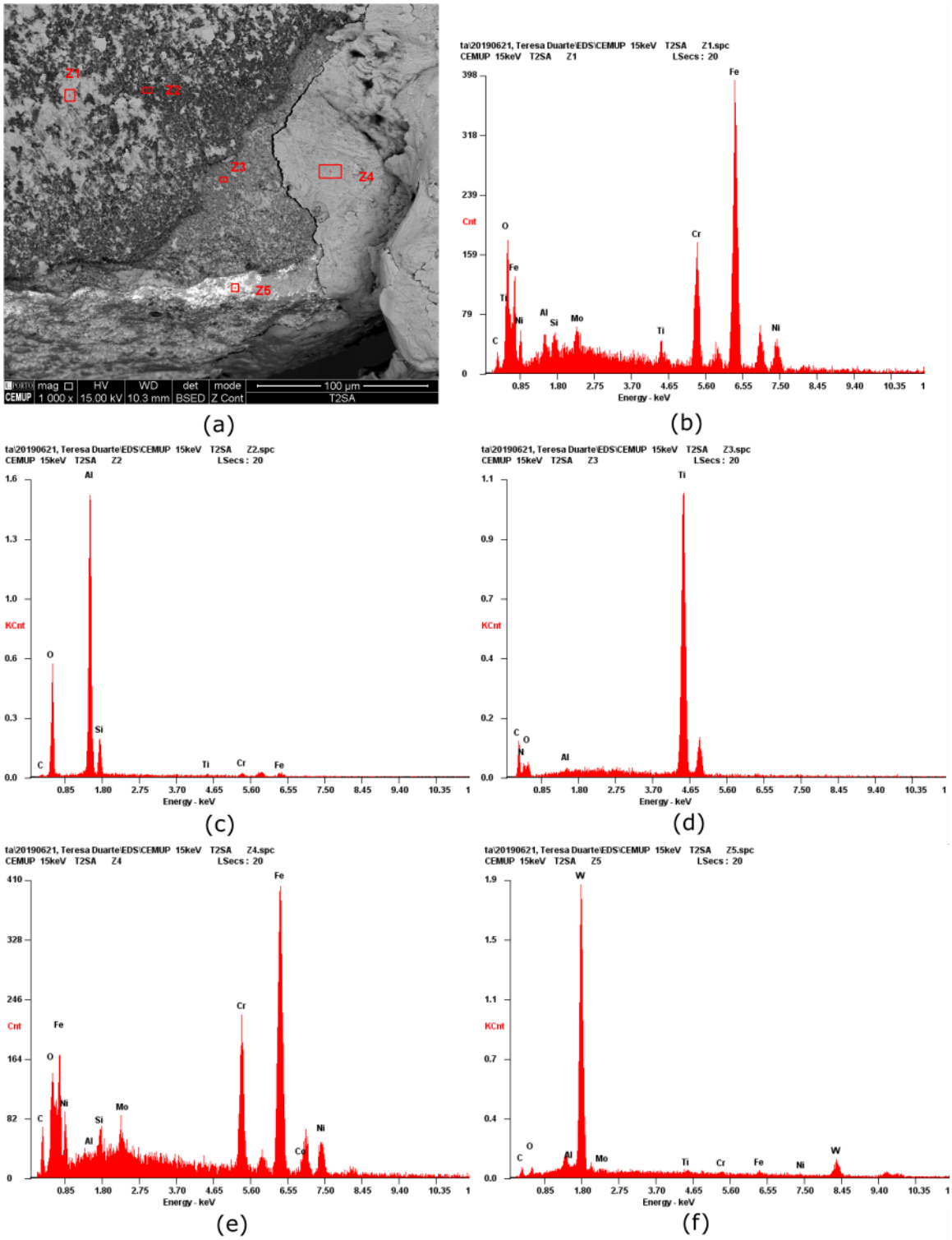


Figure D.1: EDS analysis of (a) cutting tool T2: (b) zone Z1; (c) zone Z2; (d) zone Z3; (e) zone Z4; (f) zone Z5.

# Appendix E

# Technical drawings of a gripping system for mounting the dynamometer on the shaping machine

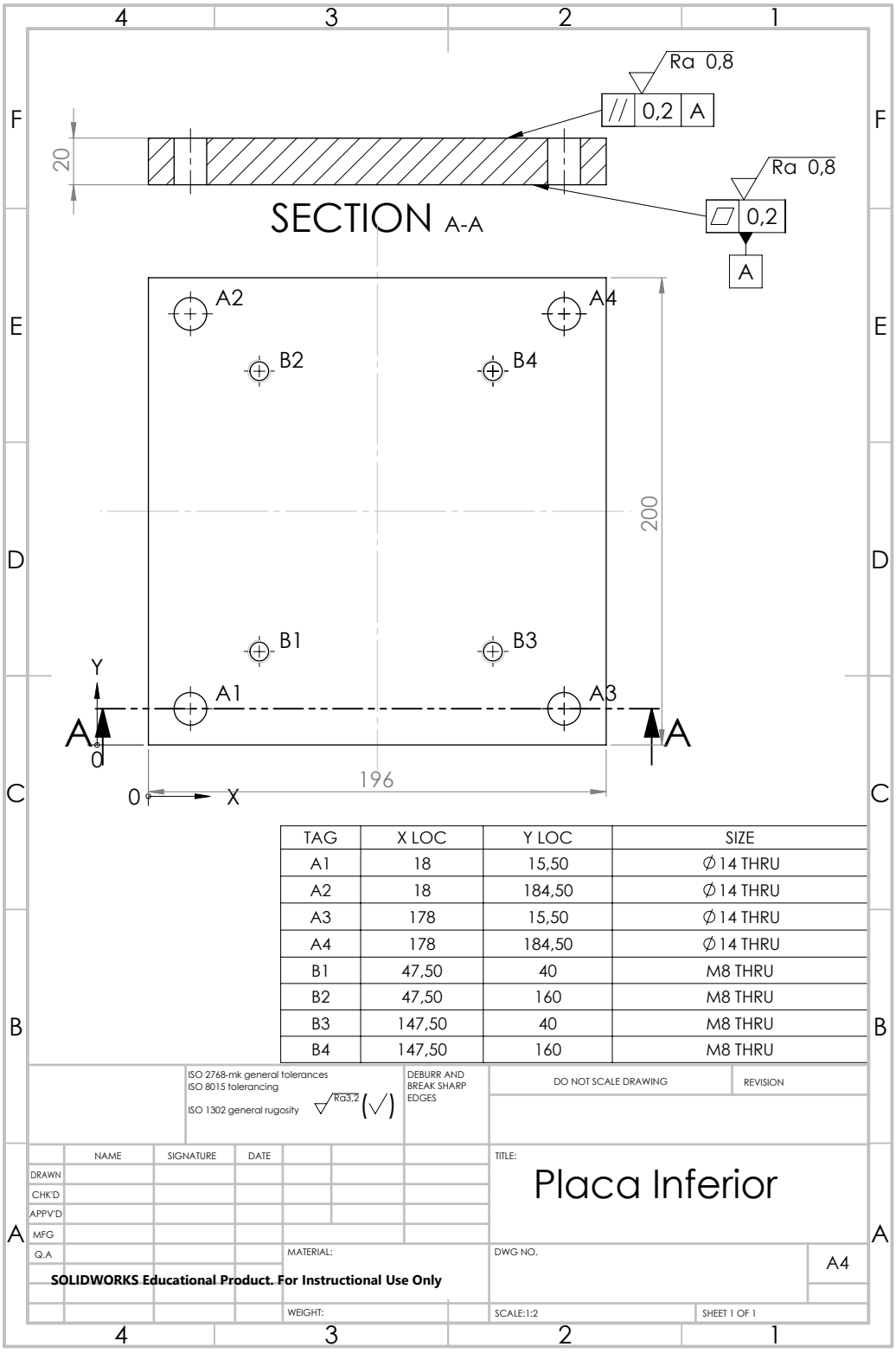


| TAG | X LOC | Y LOC | SIZE |
|---|---|---|---|
| A1 | 18 | 15,50 | ∅14 THRU |
| A2 | 18 | 184,50 | ∅14 THRU |
| A3 | 178 | 15,50 | ∅14 THRU |
| A4 | 178 | 184,50 | ∅14 THRU |
| B1 | 47,50 | 40 | M8 THRU |
| B2 | 47,50 | 160 | M8 THRU |
| B3 | 147,50 | 40 | M8 THRU |
| B4 | 147,50 | 160 | M8 THRU |

Figure E.1: Technical drawing of the lower plate to assemble the dynamometer on the shaping machine type L2-03.6.

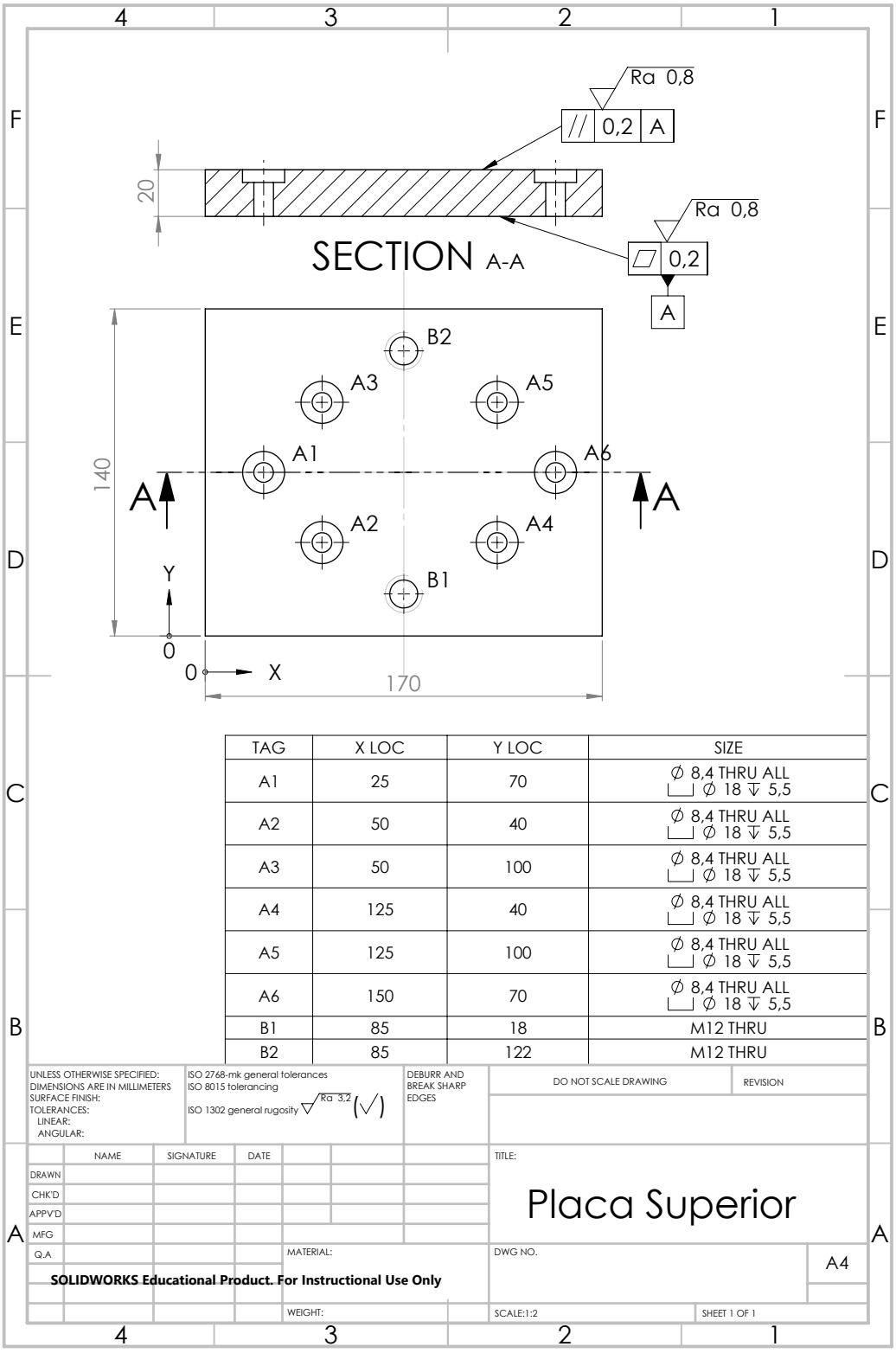


Figure E.2: Technical drawing of the upper plate to assemble the dynamometer on the shaping machine type L2-03.6.